

**DESIGN OF PIERCING BEAM PORT OF ITU TRIGA MARK
II RESEARCH REACTOR FOR BNCT APPLICATION**

**İTÜ TRIGA MARK II ARAŞTIRMA REAKTÖRÜ DELİCİ
IŞINLAMA KANALININ BNCT UYGULAMASI İÇİN
TASARIMI**

MEHMET TÜRKMEN

**Associate Prof. Dr. ŞULE ERGÜN
Supervisor**

Submitted to Institute of Sciences of Hacettepe University
as a Partial Fulfillment to the Requirements
for the Award of the Degree of Doctor of Philosophy
in Nuclear Engineering

2015

This work named “**Design of Piercing Beam Port of ITU TRIGA Mark II Research Reactor for BNCT Application**” by **MEHMET TÜRKMEN** has been approved as a thesis for the Degree of **DOCTOR OF PHILOSOPHY IN NUCLEAR ENGINEERING** by the below mentioned Examining Committee Members.

Prof. Dr. Ayhan YILMAZER

Head

.....

Associate Prof. Dr. Şule ERGÜN

Supervisor

.....

Associate Prof. Dr. Cemil KOCAR

Member

.....

Prof. Dr. Üner ÇOLAK

Member

.....

Prof. Dr. İskender A. REYHANCAN

Member

.....

This thesis has been approved as a thesis for the Degree of **DOCTOR OF PHILOSOPHY IN NUCLEAR ENGINEERING** by Board of Directors of the Institute for Graduate Studies in Science and Engineering.

Prof. Dr. Fatma SEVİN DÜZ

Director of the Institute of
Graduate Studies in Science

To my family

ETHICS

In this thesis study, prepared in accordance with the spelling rules of Institute of Graduate Studies in Science of Hacettepe University,

I declare that

- all the information and documents have been obtained in the base of the academic rules
- all audio-visual and written information and results have been presented according to the rules of scientific ethics
- in case of using others Works, related studies have been cited in accordance with the scientific standards
- all cited studies have been fully referenced
- I did not do any distortion in the data set
- and any part of this thesis has not been presented as another thesis study at this or any other university.

27/07/2015

İmza

Mehmet TÜRKMEN

ABSTRACT

DESIGN OF PIERCING BEAM PORT OF ITU TRIGA MARK II RESEARCH REACTOR FOR BNCT APPLICATION

Mehmet TÜRKMEN

Doctor of Philosophy, Department of Nuclear Engineering

Supervisor: Associate Prof. Dr. Şule ERGÜN

July 2015, 110 Pages

Main aim of this study is to design the piercing beam port (PBP) of İstanbul Technical University TRIGA Mark II Research and Training Reactor (ITU-TRR) for the purpose of nuclear applications. The nuclear application interested in this study is the Boron-Neutron Capture Therapy method (BNCT). As a neutron source, fission neutrons supplied by the ITU-TRR core are used. Availability of the incident beam of the PBP for the BNCT application is investigated. Beam shaping based on the requirements of the application is carried out by employing the Genetic Algorithm (GA) method coupled with a Monte Carlo-based reactor physics code.

For this purpose, first, a three-dimensional full-core model of the considered reactor was carried out using MCNP5/6 as a reactor physics code. The reactor model was validated with the design values given in the Safety Analysis Report (SAR). Following the validation, the reactor was re-modeled using the latest reactor operation sequence taken from the reactor log-book. Burnup effect on the incoming particle spectrum of the interested BP was investigated using the considered reactor operation sequence. Thereby, a burnup analysis was initiated for the recent core configuration. Hot-full power condition was used in the burnup calculations and PBP calculations. The temperature-dependent cross-section libraries required for the reactor physics code were produced using the NJOY code.

At the current burnup level of the reactor, particles (neutron and photon) which enter into the interested BP from the reactor core were recorded into a source file and used as a neutron/photon source in later calculations. To reduce the computational time of Monte Carlo

(MC) calculations, the BP was discarded from the full-core model and separately modeled. To achieve the desired flux values that the BNCT requires, the design calculations were focused on searching a number of proper patterns formed by a combination of filtering, spectrum shifter and collimator materials without changing core configuration or BP location inside the reactor. For this purpose, a computer code which uses Non-dominated Sorting GA (NSGA-2) method coupled with MCNP generating the optimized patterns was prepared. The optimization objectives are the maximization of epithermal neutron flux and minimization of the other fluxes in the incident beam as low as possible. To reduce high computational uncertainties due to the nature of deep penetration problem, optimization process was carried out in three steps as the spectrum shifter, filtering and collimator patterns. That is, each part was optimized separately. Once the optimization process is over, all the sub-patterns were recombined to obtain the final pattern. Optimization results were compared with the bare port results. The obtained results were discussed from the viewpoint of feasibility of BNCT in the BP.

Results of the MC model of the reactor well agree with the design parameters given in the SAR. On the other hand, it was observed that burnup level of the reactor has a significant effect on the incident beam of the BP. The PBP has a thermal neutron flux of $5.88 \pm 0.01 \times 10^8 \text{ n cm}^{-2} \text{ s}^{-1}$, an epithermal neutron flux of $2.70 \pm 0.01 \times 10^8 \text{ n cm}^{-2} \text{ s}^{-1}$, a fast neutron flux of $5.75 \pm 0.01 \times 10^8 \text{ n cm}^{-2} \text{ s}^{-1}$ and a photon fluence of $1.87 \pm 0.01 \times 10^9 \text{ } \gamma \text{ cm}^{-2} \text{ s}^{-1}$ at the port exit when the port is bare. When an optimized pattern is used inside the port, epithermal neutron flux is calculated to be $4.17 \pm 0.14 \times 10^8 \text{ n cm}^{-2} \text{ s}^{-1}$ with a current-to-flux ratio of 0.87 ± 0.03 . Furthermore, thermal and fast neutron fluxes, and photon fluence are reduced by about 20, 3 and 200 times, respectively. Therefore, it is evident that the BNCT is applicable in the PBP, by supplying the desired neutron fluxes at the port exit. The results show that the method which couples the GA with the MC method works well for this kind of optimization problem. To sum up, the beam shaping method suggested in this study is independent from user experiences and can readily be implemented into any incident beam of a considered research reactor (even for other neutron sources) for a desired nuclear application.

Keywords: ITU TRIGA Mark II, BNCT, Piercing Beam Port, Monte Carlo Method, Genetic Algorithm, Optimization, Neutron Flux

ÖZET

İTÜ TRIGA MARK II ARAŞTIRMA REAKTÖRÜ DELİCİ IŞINLAMA KANALININ BNCT UYGULAMASI İÇİN TASARIMI

Mehmet TÜRKMEN

Doktora, Nükleer Enerji Mühendisliği Bölümü

Tez Danışmanı: Doç. Dr. Şule ERGÜN

Temmuz 2015, 110 Sayfa

Bu çalışmanın temel amacı, nükleer uygulamalar için İstanbul Teknik Üniversitesi TRIGA Mark II Araştırma ve Eğitim Reaktörünün (ITU-TRR) delici ışınlama kanalının yeniden tasarlanmasıdır. Bu çalışmada, ilgilenilen nükleer uygulama Boron-Nötron Yakalama Terapisi (BNCT)' dir. Nötron kaynağı olarak, ITU-TRR korundan tedarik edilen fisyon nötronları kullanılmaktadır. Bahsedilen uygulama için porta gelen nötron demetinin kullanılabilirliği incelenmektedir. BNCT uygulamasının gereksinimleri temel alınarak yapılan demet şekillendirme işlemi, Monte-Carlo tabanlı reaktör fiziği kodu ile birleştirilmiş Genetik Algoritma (GA) kodu kullanılarak gerçekleştirilmektedir.

Bu amaçla, ilk olarak, ilgilenilen reaktörün üç-boyutlu tam-kor bir modeli, MCNP5/6 kullanılarak gerçekleştirilmiştir. Reaktör modelinin doğruluğu, Güvenlik Analizi Raporunda (GAR) verilen tasarım değerleri ile kontrol edilmiştir. Daha sonra, reaktör, reaktör kayıt defterinden alınan son işletme kaydı kullanılarak modellenmiştir. Reaktörün yakıt yanma oranının, ilgilenilen ışınlama portuna gelen parçacık spektrumuna olan etkisi incelenmiştir. Bu nedenle, mevcut reaktör kor yüklemesi düzeni için bir yakıt yanma oranı analizi gerçekleştirilmiştir. Yakıt yanma oranı ve ışınlama kanalı hesaplamalarında sıcak-tam güç durumu kullanılmıştır. Reaktör fiziği kodunun gereksinim duyduğu sıcaklık-bağımlı tesirkesiti kütüphaneleri NJOY kodu kullanılarak üretilmiştir.

Reaktörün güncel yakıt yanma oranında, reaktör korundan ilgilenilen ışınlama kanalına gelen parçacıklar (nötron ve foton), bir kaynak dosyasına kaydedilmiş ve daha sonraki hesaplamalarda nötron/foton kaynağı olarak kullanılmıştır. Monte-Carlo (MC)

hesaplamalarının hesaplama zamanını azaltmak için ilgilenilen ışınlama kanalı, reaktör tamkor modelinden ayrı olarak tekrar modellenmiştir. BNCT için önerilen akı değerlerine ulaşmak için, düşünülen tasarım, mevcut kor düzeni ve mevcut ışınlama kanalının reaktör içindeki pozisyonu değiştirilmeksizin, ışınlama kanalına yerleştirilmek üzere, spektrum kaydırıcı, süzgeç ve kolimatör malzemelerden oluşan uygun bir malzeme dizisinin araştırılmasıdır. Bu amaçla, MCNP ile birleştirilmiş Non-dominated Sorting GA (NSGA-2) metodu kullanan ve malzeme sırasını optimize eden bir bilgisayar kodu hazırlanmıştır. Optimizasyon amaçları, gelen demetin epitermal nötron akısının mümkün olduğunca en yüksek düzeye çekilmesi, diğer akıların ise mümkün olduğunca en alt düzeye çekilmesidir. Derin delme problemlerinin doğasından kaynaklanan yüksek hesaplama belirsizliklerini azaltmak amacıyla, optimizasyon işlemi, spektrum kaydırıcı, süzgeç ve kolimatör olarak üç adımda gerçekleştirilmiştir. Her parça ayrı olarak optimize edilmiştir. Optimizasyon işleminden sonra, bütün parçalar tekrar birleştirilerek nihai malzeme sırası elde edilmiştir. Optimizasyon sonuçları ışınlama kanalının çıplak durum sonuçları ile kıyaslanmıştır. Sonuçlar, ilgilenilen ışınlama kanalında BNCT'nin uygulanabilirliği açısından irdelenmiştir.

Reaktörün MC model sonuçları, GAR'da verilen tasarım değerleri ile uyum içerisindedir. Diğer taraftan, reaktörün yakıt yanma oranı, ışınlama kanalına gelen demet üzerinde oldukça etkili olduğu gözlemlenmiştir. Işınlama kanalı boş durumda iken, delici ışınlama kanalı (kanal çıkışında), $2,70 \pm 0,01 \times 10^8 \text{ n cm}^{-2} \text{ s}^{-1}$ lik epitermal nötron akısına, $5,88 \pm 0,01 \times 10^8 \text{ n cm}^{-2} \text{ s}^{-1}$ lik termal nötron akısına, $5,75 \pm 0,01 \times 10^8 \text{ n cm}^{-2} \text{ s}^{-1}$ lik hızlı nötron akısına ve $1,87 \pm 0,01 \times 10^9 \gamma \text{ cm}^{-2} \text{ s}^{-1}$ lik foton akısına sahiptir. Işınlama kanalında optimize edilmiş uygun bir malzeme dizisi kullanıldığında ise epitermal nötron akı değeri ve nötron akımının akıya oranı, sırasıyla $4,17 \pm 0,14 \times 10^8 \text{ n cm}^{-2} \text{ s}^{-1}$ ve $0,87 \pm 0,03$ olarak hesaplanmaktadır. Ayrıca, gelen demetin termal ve hızlı nötron akıları ve ayrıca foton akı kirlilikleri, çıplak ışınlama kanalı sonuçlarına göre sırasıyla 20, 3 ve 200 kat aşağı çekilebilmektedir. Dolayısıyla, BNCT yönteminin, kanal çıkışında önerilen minimum nötron akı değerlerine ulaşarak, delici ışınlama kanalında uygulanabilir olduğu ortaya konulmuştur. Sonuçlar, MC yöntemi ile birleştirilmiş GA yönteminin bu tür problemlerin çözümü için kullanımının çok uygun olduğunu göstermektedir. Özetle, bu çalışmada önerilen demet şekillendirme yöntemi, kullanıcı deneyiminden bağımsızdır ve herhangi bir araştırma reaktörünün (hatta diğer nötron kaynakları için) gelen nötron demetine ilgilenilen bir nükleer uygulama için kolaylıkla uygulanabilir.

Anahtar Kelimeler: ITU TRIGA Mark II, BNCT, Delici Işınlama Portu, Monte Carlo Yöntemi, Genetik Algoritma, Optimizasyon, Nötron Akısı

ACKNOWLEDGEMENTS

I would like to express my deepest gratitude to Professor Şule Ergün and Professor Üner Çolak, who helped guide this thesis research through numerous conversations and calculations. Their prompt comments were very useful during the preparation of this thesis.

Thanks to Dr. Zafer Akan for all his help. He supervised the construction of the experimental setup for the radial beam port. Thanks to reactor working group for all of his help in performing the experiments.

I would like to thank Dr. Ayhan Yılmaz and Dr. Cemil Kocar for giving their time to serve on my reading committee and for providing advice on this research.

Finally, this research was funded by the Scientific and Technological Research Council of Turkey (TUBITAK) 2211-C national scholarship programme.

The numerical calculations reported in this paper were partially performed at TUBITAK ULAKBIM, High Performance and Grid Computing Center (TRUBA Resources).

TABLE OF CONTENTS

	<u>Page</u>
ABSTRACT.....	i
ÖZET	iii
ACKNOWLEDGEMENTS	v
TABLE OF CONTENTS.....	vi
LIST OF TABLES	ix
LIST OF FIGURES	x
SYMBOLS AND ABBREVIATIONS	xii
1. INTRODUCTION	1
1.1 Purpose of This Study	1
1.2 Outline of the Thesis	3
1.3 Literature Review	5
2. ITU TRIGA MARK II RESEARCH REACTOR	8
2.1 General Design Parameters of the Reactor	8
2.2 Fuel, Moderator and Control Rod Design.....	10
2.3 Fuel Density and H/Zr Atom Ratio	13
2.4 Reactor Tank, Grid Plate and Reflector Assembly Design.....	13
2.5 Beam Ports and Thermal Column Design.....	14
3. MONTE-CARLO MODEL OF THE REACTOR.....	16
3.1 Reactor Core.....	16
3.1.1 Cold-Zero Power Condition.....	17
3.1.2 Hot-Full Power Condition.....	17
3.2 Temperature-dependent Cross-Section Generation	17
3.3 Burnup-Dependent Neutron Spectrum Calculation for the BP.....	18
3.4 Beam Ports	21
3.5 Input Parameters for the Reactor Physics Code	22

3.6	The Used Codes	24
3.6.1	MCNP5/6.1	24
3.6.1.1	Cards Used for the Tally Purpose	24
3.6.1.2	Variance Reduction Methods	25
3.6.2	MONTEBURNS2	26
3.6.3	NJOY	27
4.	REQUIREMENTS FOR BNCT APPLICATION IN RESEARCH REACTORS	28
4.1	Introduction to BNCT Application	28
4.2	Desired/Undesired Neutron Beam Characteristics	29
4.3	The Methods to Design the Beam (Port)	30
4.4	Choice of the Materials to be used in the Beam Design	32
4.4.1	Spectrum Shifter Materials	32
4.4.2	Filtering Materials	37
4.4.3	Collimator Materials	40
4.4.4	Gamma Shielding	41
5.	IMPLEMENTATION OF GENETIC ALGORITHM	43
5.1	Fundamentals of the GA	43
5.2	Use of the GA Method in Beam Shaping	44
5.3	MOGA: NSGA-II Method	45
5.3.1	Details of Fast Non-Dominated Sorting method	47
5.3.2	Details of Crowding Distance	47
5.3.3	Details of Crowded-Comparison Operator	48
5.4	Validation of the prepared GA code	48
5.5	Pattern Creation	50
5.5.1	Spectrum Shifter	51
5.5.2	Filtering	52
5.5.3	Collimator	53

5.6	Description of the Chromosome Structure.....	54
5.7	Selection operator.....	54
5.8	Crossover operator	55
5.9	Mutation operator.....	55
5.10	Cost Calculation: Reactor physics code	55
5.11	Convergence Criterion	55
5.12	Optimization Parameters	56
6.	RESULTS AND DISCUSSION	57
6.1	Validation of the MCNP Model.....	57
6.2	Burnup-Dependent Neutron Spectrum Calculations.....	58
6.3	Design of Piercing Beam Port for the BNCT Application.....	60
6.3.1	Particle Flux in the Bare PBP	60
6.3.2	GA Results for Spectrum Shifter Sub-pattern Optimization	63
6.3.3	GA Results for Filtering Sub-pattern Optimization.....	69
6.3.4	GA Results for Collimator Sub-pattern Optimization	74
6.3.5	Final Pattern: Uniting the Sub-patterns.....	79
6.4	Concluding Remarks	82
	REFERENCES	86
	CIRRICULUM VITAE	92

LIST OF TABLES

Table 2.1 Design parameters for ITU-TRR	10
Table 2.2 Geometric Properties of BPs.....	14
Table 4.1 Desired neutron beam characteristics for the BNCT application [61] [62].....	30
Table 4.2 Materials used to design the epithermal neutron beam in various research reactors	31
Table 4.3 Suitable spectrum shifter isotopes and decay schemes following neutron absorption [63].....	35
Table 4.4 Suitable filtering isotopes and decay schemes following thermal neutron absorption [63].....	39
Table 4.5 Suitable collimator materials and decay schemes following neutron absorption [63]	41
Table 5.1 Test problems used for validation.....	49
Table 5.2 Spectrum shifter materials to be used in the pattern creation	52
Table 5.3 Filtering materials used in the pattern creation.....	53
Table 5.4 Collimator materials used in the pattern creation	53
Table 5.5 Summary of the optimization parameters	56
Table 6.1 Effective multiplication factor	57
Table 6.2 Available patterns for the spectrum shifter sub-pattern design	68
Table 6.3 Particle fluxes with and without the sub-pattern	69
Table 6.4 Available patterns for the filtering sub-pattern design	73
Table 6.5 Particle fluxes with and without the sub-pattern	74
Table 6.6 Available sub-patterns for the collimator sub-pattern design.....	78
Table 6.7 Particle fluxes with and without the sub-pattern	79
Table 6.8 Particle fluxes with and without the final pattern	80

LIST OF FIGURES

Fig. 1.1 Computational flow diagram of the thesis.....	5
Fig. 2.1 The reactor core components of ITU-TRR (Vertical View)	8
Fig. 2.2 The reactor core components of ITU-TRR (Radial View).....	9
Fig. 2.3 Fuel-loading core map of ITU-TRR.....	11
Fig. 2.4 TRIGA stainless steel clad fuel element with end fittings	12
Fig. 3.1 Radial (left) and vertical (right) view of the reactor core in the MCNP model	16
Fig. 3.2 NJOY99 Flow Diagram.....	18
Fig. 3.3 Computational flow diagram for burnup calculations.....	21
Fig. 3.4 Radial view of the PBP in the MCNP model	21
Fig. 4.1 Scattering (green) and total (red) cross-section of the some selected isotopes. [63]..	33
Fig. 4.2 Scattering (green) and total (red) cross-section of some commonly used moderator materials. [63]	36
Fig. 4.3 Scattering (green) and total (red) cross-section of the some selected isotopes. [63]..	38
Fig. 4.4 Mass attenuation coefficient of Pb and Bi [65]	42
Fig. 5.1 GA flowchart for SOGA and MOGA (NSGA-II) methods	45
Fig. 5.2 Comparison of results of NSGA-II with results of this study for the test problems of SCH, FON, KUR and ZDT2.....	50
Fig. 5.3 A sample pattern generated using spectrum shifter materials	52
Fig. 5.4 A sample pattern generated using the filtering materials	53
Fig. 5.5 A sample pattern generated by using the collimator materials.....	54
Fig. 5.6 Genotype and phenotype of a sample chromosome generated using spectrum shifter	54
Fig. 6.1 Variation of the reactivity (ρ) with the cumulative burnup (MWh).....	58
Fig. 6.2 Change of incoming neutron spectrum of the PBP at BOL and EOL.....	60
Fig. 6.3 MCNP view of the bare PBP	61
Fig. 6.4 Change of particle flux along with distance from the core center.....	62

Fig. 6.5 Change of particle flux along with radius of PBP: at the port entry surface (left) and at the port exit surface (right)	62
Fig. 6.6 Neutron spectra at various port locations	63
Fig. 6.7 Photon spectra at various port locations	63
Fig. 6.8 Optimization results for Spectrum Shifter sub-patterns: (a) Solution space, (b) Epithermal neutron flux solutions with respect to generation number, (c) Evolution of the solutions at initial, midway and final generations and (d) Pareto-front solutions.	65
Fig. 6.9 A selected pattern for the spectrum shifter	69
Fig. 6.10 Optimization results for Filtering sub-patterns: (a) Solution space, (b) Epithermal neutron flux solutions with respect to generation number, (c) Evolution of the solutions at initial, midway and final generations and (d) Pareto-front solutions.....	71
Fig. 6.11 A selected pattern for the filtering	74
Fig. 6.12 Optimization results for Collimator sub-patterns: (a) Solution space, (b) Epithermal neutron flux solutions with respect to generation number, (c) Evolution of the solutions at initial, midway and final generations and (d) Pareto-front solutions.....	76
Fig. 6.13 A selected pattern for collimator	79
Fig. 6.14 View of the final pattern	80
Fig. 6.15 Change of particle flux along with distance from the core center with and without the final pattern	81
Fig. 6.16 Neutron spectrum at the port exit with and without the final pattern.....	82

SYMBOLS AND ABBREVIATIONS

Symbols

Φ	Neutron Flux	(n cm ⁻² s ⁻¹)
I	Photon Fluence	(γ cm ⁻² s ⁻¹)
J	Neutron Current	(n cm ⁻² s ⁻¹)
n	Neutron	
γ	Photon	
k_{eff}	Effective Core Multiplication Factor	
ρ	Density	(g/cm ³)
w	Weight Percent	(%)
x	Hydrogen-to-Zirconium Atom Ratio (N_H/N_{Zr})	
ν	Average Number of Neutrons Produced per Fission	
P	Reactor Power	(kW)
Q_{ave}	Average Fission Energy Release	(MeV)
S (α, β)	Thermal Scattering	
B	Specific Burnup	(MWh) or (MWd/kgU)
N	Population Size	
f	Fitness Function	
n	Chromosome Length	
E	Energy	(MeV)

Abbreviations

BP	Beam Port
PBP	Piercing BP
GA	Genetic Algorithm
MOGA	Multi-Objective GA
SOGA	Single-Objective GA
NSGA	Non-dominated Sorting GA
SUS	Stochastic Uniform Sampling Method
(B)NCT	(Boron) Neutron Capture Therapy
MCNP	Monte Carlo N-Particle Code
NJOY	Nuclear Data Processing System
ITU	İstanbul Technical University

ITU-TRR	İstanbul Technical University TRIGA Mark II Research Reactor
ENDF	Evaluated Nuclear Data File
JEFF	Joint Evaluated Fission and Fusion File
JENDL	Japanese Evaluated Neutron Data Library
TENDL	TALYS-based Evaluated Nuclear Data Library
CENDL	Chinese Evaluated Neutron Data Library
PE	Poly-Ethylene
EOL	End-of-Life
BOL	Beginning-of-Life
IAEA	International Atomic Energy Agency
1/2/3-D	2 or 3-Dimension
UZrH	Uranium Zirconium-Hydride
U	Uranium
H	Hydrogen
Zr	Zirconium
epi	Epithermal
th	Thermal
K	Kelvin
F1/2/4/5/6/MESH	Tally Indicator for MCNP
SSR/SSW	Source Surface File Indicator for MCNP
ACE	Proprietary Data Compression Archive File Format
CR	Control Rod
OECD-NEA	Nuclear Energy Agency
MC	Monte Carlo
MONTEBURNS	Monte Carlo Burnup Tool
FP	Fission Product
SAR	Safety Analysis Report
FPD	Full Power Day
Exp	Experiment
CZP	Cold-Zero Power
HFP	Hot-Full Power

1. INTRODUCTION

In this study, a design study to shape the incident beam of the piercing beam port (PBP) of İstanbul Technical University TRIGA Mark II Research and Training Reactor (ITU-TRR) for the Boron-Neutron Capture Therapy method (BNCT) application is performed. In this manner, optimum material sequence and geometry to be placed into the PBP are investigated using spectrum shifter, filtering and collimation methods.

1.1 Purpose of This Study

The main issue in applying the BNCT in an irradiation facility is the beam shaping. This is because an unshaped incident beam has a number of desired and undesired flux (contamination) components. Some of them are very lethal for the healthy cells. Hence, primary purpose in shaping is to reduce these unwanted components of the incident beam as low as possible.

The shaping process depends on the kind of neutron source that is utilized. Thus, for the BNCT application, as the neutron source, ITU-TRR is considered. ITU-TRR is intentionally selected due to not only providing necessary neutron flux spectrum but also due to easy modification. However, the key parameter in choosing the proper reactor is flux-to-power ratio since it has a close relationship with the irradiation time and the reactor power. A lower power with a shorter irradiation time is desired in these types of reactors. In this manner, the selected reactor, ITU-TRR, with a full power of 250 kW and a peak neutron flux of $\sim 10^{13}$ n cm⁻² s⁻¹ at the core center, is suitable.

The BNCT is examined in the piercing beam port (BP) of the considered reactor by means of the epithermal neutrons. The reason is that a separate study [1] performed in the radial BP of the interested reactor shows that the BNCT is practically possible if the port (and the others) is modified properly. However, for the sake of increasing the applicability of BNCT, a different BP, named PBP, is utilized in this study.

Each research reactor is designed to have a number of BPs (radial, tangential, etc.). In the course of construction process, each BP is particularly located inside the reactor to provide a different spectrum. For instance, the tangential BP supplies a higher thermal neutron flux than the PBP which is designed to give a higher fast neutron flux. Due to the mentioned characteristics of the BPs, in this study, the PBP is preferred for the BNCT.

Besides the construction, the incident beam of the BPs is, also, re-designed during the experiments to meet the specific requirements. The modifications are carried out by placing a number of materials with different shape, geometry and sequence into the BP. Typically, there

are three employed methods, as spectrum shifter, filtering and collimation, to shape the beam. A combination of these materials are called as the pattern. The main role of the patterns is to eliminate the undesired part of the incident beam while the desired part of the incident beam is retained.

The design process follows the estimation of application-dependent bounds (or constraints) such as minimum epithermal flux required for the irradiation of cancerous cells and then determination of possible filtering, spectrum shifter and collimator materials (e.g. PE, Fluental, Al). In the earlier studies performed, this process is based on the experiences of the researches, trial and error method, and the results of the previous studies. Yet, these types of the problems (pattern search) are optimization problems as the problem contains several objectives to be maximized/minimized. Therefore, in this study, a new method, which is free from the user experience, is suggested to shape the beam. The proposed method bases on the use of GA coupled with a Monte-Carlo based reactor physics code to investigate the proper material sequence.

In this study, to obtain the desired flux values that the BNCT requires, the pattern generation is performed using a Multi-Objective Genetic Algorithm (MOGA) computer code, namely Non-dominated Sorting Method (NSGA-2 method). However, it should be noted that the type of the optimization problem determines which solution method(s) is the most suitable for the analyses. For example, the stochastic methods are superior, not the best, in the area of in-core nuclear fuel management calculations than the mathematical optimization methods like (non)linear and quadratic methods. Therefore, as a stochastic method, the GA is chosen since it imitates the way the nature does (behaves) to get more diverse and better generations, and works well for the pattern search problems. Furthermore, the patterns are obtained using NSGA-2 method as a MOGA since the pattern search problems have more than one (multiple) objective to be optimized, and these objectives require optimization all at once. Also, the selected genetic algorithm (GA) method has been used frequently in the similar problems. It is a well-efficient, well-proven and fast GA method.

A Monte-Carlo (MC) based calculation is carried out in this study since the simulation models are mainly used to investigate the possible modifications/changes in the current designs of reactors without an experiment is performed. Further, experiments require a great deal of time, a number of staff/researchers and lots of expenditure; thus, the simulations are very proper for modeling process. Among the modelling methods, MC method offers great opportunities such as modeling the reactor in detail, use of the stochastic method for the transport of particles in

the medium and tallying the particles in any considered region. Therefore, the reactor is modelled by employing the MC method.

The last but equally important thing is that the particle spectrum in the BP strictly depends on the burnup level of the reactor. Thus, a burnup calculation is carried out to calculate up-to-date burnup level of the reactor.

In summary, the main aim of this study is to design the PBP of ITU-TRR for the purpose of nuclear applications. The nuclear application interested in this study is the Boron-Neutron Capture Therapy method (BNCT). As the neutron source, fission neutrons supplied by the ITU-TRR core are used. Availability of the incident beam of the PBP is investigated. Beam shaping based on the requirements of BNCT application is carried out by employing GA method coupled with an MC-based reactor physics code. The technique suggested in this study is unique since the GA method coupled with MCNP has not been considered in searching the pattern for the considered nuclear application and also the interested research reactor has not, yet, been used for the nuclear applications. Also, burnup effect on the incident beam has not been studied thus far.

1.2 Outline of the Thesis

To achieve the primary purpose described in Section 1.1, first of all, a 3D full-core MC model of the ITU TRIGA Mark II research reactor was carried out by utilizing a reactor physics code. For that purpose, MCNP5/6 code was selected.

After validation and testing process of the reactor model in cold-zero power condition (CZP), the reactor state was changed to hot-full power condition (HFP) in the model. This is done since the BNCT experiments require higher particle flux(es). The highest flux is produced when the reactor is at the full-power. The neutronics feedbacks mechanisms (e.g., density correction, Doppler broadening) at full-power were included into the reactor model. For all the materials, temperature-dependent cross-sections were produced using NJOY.

Later, burnup effect on the incoming neutron spectrum for the PBP was investigated. For the current core map of the reactor, a burnup analysis was performed by using the information of positions of the CRs of reactor operation sequence selected from the log-book. The up-to-date burnup level of the reactor was calculated.

Under the calculated up-to-date burnup condition, the particles entering into the PBP were written into a source file. Next, the PBP was separately modeled once again, discarding the reactor core.

First, the particle fluxes were calculated while the BP was empty. Following the estimation of nuclear application (i.e., BNCT), requirements were searched. The modifications were focused on searching a number of proper material and geometry sequence (patterns) formed by the combination of filtering, spectrum shifter and collimator materials.

For this purpose, a computer code which uses Non-dominated Sorting GA (NSGA-2) method coupled with MCNP generating the optimized patterns was prepared.

In order to reduce high computational uncertainties due to nature of the deep penetration problem, optimization process was carried out in three steps as optimizing the spectrum shifter, filtering and collimator patterns. For each sub-pattern, a number of most proper materials/isotopes were determined by taking the neutronic properties of the materials into account.

Each part was optimized separately. After the optimization process, all the sub-patterns were recombined to obtain the final pattern.

Main computational steps are outlined below. A computational flow diagram is, also, presented in Fig. 1.1.

- i. Develop a computer model for the ITU-TRR with a MC based reactor physics code in CZP.
- ii. Validate the reactor model using SAR/experimental values.
- iii. Simulate the reactor in HFP and include the feedbacks.
- iv. Generate temperature-dependent neutron cross-section libraries using NJOY.
- v. Calculate up-to-date burnup level of the reactor core.
- vi. Investigate the burnup effect on the incoming particle fluxes of the PBP.
- vii. Obtain the burnup-dependent incoming particle spectrum in the PBP.
- viii. Create a source file for the PBP.
- ix. Model the BP alone.
- x. Obtain particle fluxes when the port is bare.
- xi. Estimate the application-dependent requirements/constraints for the BNCT.
- xii. Examine the most appropriate materials suitable for BNCT.
- xiii. Use an optimization method to find the proper patterns.
- xiv. Prepare a GA code coupled with MCNP.
- xv. Obtain the available patterns for the BNCP in the PBP.

The thesis is arranged in the following way. The rest of this chapter includes the summary of the literature review. Chapter 2 describes the general design characteristics of ITU-TRR. Chapter 3 gives details of MC modeling of the core and the BP of ITU-TRR. Chapter 4 defines the fundamentals and the requirements of BNCT application. Chapter 5 provides detailed information about the optimization process. Chapter 6 provides results of optimization study for PBP and discusses the calculated results for the feasibility of BNCT.

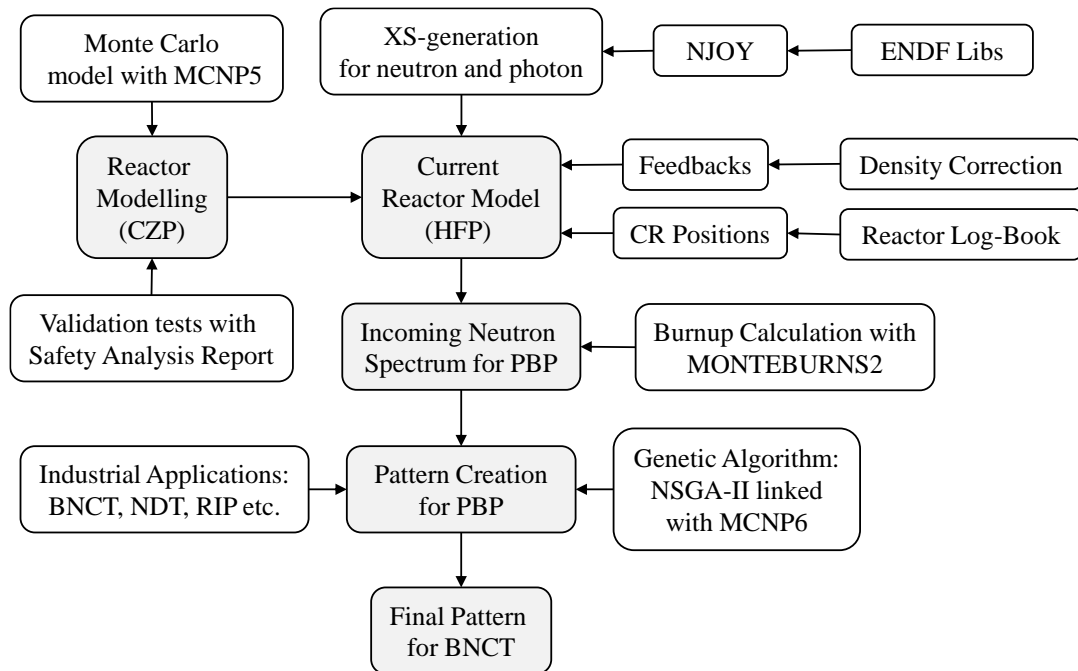


Fig. 1.1 Computational flow diagram of the thesis

1.3 Literature Review

The fundamentals of the BNCT were proposed by Locker [2] in the late of 1930s. The first BNCT experiment was performed on the tumors of the mice in 1940 by Kruger [3]. After the first experiment, many pioneering studies have been performed in USA ([4], [5]), Japan ([6], [7]) and Europe ([8], [9]).

An important issue for the BNCT application is the use of high intensity thermal or epithermal (even fast) neutron sources, depending on the tumor location. Thermal neutrons are superior to epithermal neutrons for treating the tumors near the surface [10]. Contrarily, use of the epithermal neutrons seems to be more convenient for deep tissue tumors such as head and neck cancers and glioblastoma multiform (GBM) [11].

For this purpose, modified research reactors (linear accelerators as well) are being considered as alternative thermal and epithermal neutron sources for BNCT. The use of research reactors

gives suitable excellent beam values both in intensity and quality, and this enables the reactors to be a neutron source for BNCT purpose [12].

In particular, TRIGA MARK II research reactors have been modified for BNCT application in some countries such as the TRIGA reactor of the University of Mainz, Germany [13], the Finnish BNCT facility (FiR1) at the University of Helsinki, Finland [14], and Tsing Hua open-pool reactor (THOR) in Taiwan [15]. Successful BNCT clinical trials for GBM patients have been achieved by different research groups [16]. Parallel to experimental studies, Kyiv [17] and Musashi [7] reactors were modelled for the BNCT using the MC method.

There have been some recent academic and clinical studies in BNCT that use neutron beams generated by the research reactors. For instance, dose distributions in the lungs of a rat model irradiated in the thermal column of the TRIGA reactor in Pavia were calculated to test the potential use of BNCT. Simulation of the rat model was performed by MCNP [18]. In addition, a theoretical model and a MC code simulating radiation-induced cell death based on the link between lethal chromosome aberrations (dicentric, rings and large deletions) were presented [19]. Later, upon successful use of the same reactor in the treatment of hepatic colorectal metastases, basic requirements and parameter optimization for the BNCT of extracorporeal irradiated and auto-transplanted organs were searched [20]. Several core configurations were considered, and core calculations with MCNP were performed to increase the beam intensity for BNCT in THOR [21]. Moreover, neutron spectra were measured in HFR and THOR BNCT beams [22]. One year later, a different method that uses indirect neutron radiography, instrumental neutron activation analysis, the cadmium difference method, and the unfolding technique was suggested to estimate the angular and spatial distributions of the thermal neutron source strength [23]. Moreover, performance of the source description of the THOR BNCT beam was performed using different measurement techniques in different phantoms [24]. In the LENA reactor, microdosimetric spectrum measurements in the thermal neutron irradiation facility were performed to characterize the BNCT radiation field [25]. For the purpose of BNCT in Finland, a beam model was defined for patient treatment planning and dosimetric calculations by using the mixed neutron photon beam of the FiR 1 reactor. The model was validated with activation foil measurements [26]. The TRIGA Mainz research reactor was used for the extracorporeal treatment of organs in BNCT to estimate the irradiation field in the thermal column [27]. Meanwhile, the same reactor was used for the treatment of liver metastases. The calculations were performed using the MCNP and ATTILA codes [28]. Recently, thermal column of the reactor was used for the dosimetric feasibility studies [29]. The neutron spectra

of radial and tangential BPs were measured in the TRIGA Mark III nuclear reactor in Mexico loaded with highly enriched uranium fuel [30]. An arrangement for the BNCT facility for tumor treatment was prepared by modeling the geometry and material composition of filtering/collimator similar to the beam tube configuration of the Massachusetts Institute of Technology Research Reactor (MITR) [31]. In the Oregon State TRIGA Reactor (OSTR), the neutron spectra of various experimental facilities were calculated by MCNP and measured experimentally. The results of low enriched U fuel were compared with those of highly enriched U fuel [32].

Modification of the research reactors for BNCT is mainly on the use of proper beam shaping materials inside the beam ports. Optimization processes are performed by changing the thickness of the beam shaping materials. Tiyapun [33] designed filter and moderator assemblies for the tangential beam port of the OSTR. In the study, MCNP was used to simulate a model of the reactor core and neutron irradiation facilities. Each selected filter/moderator material was placed into the BP separately and optimum thickness of the material was evaluated by increasing the thickness step by step. Similar to Tiyapun [33], Sweezy [34] proposed a filter and collimator system for boron neutron enhanced fast neutron therapy using MCNPX. In contrast to them, to optimize the beam shaping assemblies, Bleuel [35] used a different optimization method named Ubertally technique, which involves post-processing of individual particle tallies in a Monte Carlo simulation to reweight the fluxes to reflect a neutron or photon source. The literature review showed that there has not been a study which uses GA method to optimize the beam shaping materials.

In Turkey, the BNCT studies mostly cover the development and synthesis of boron carrier compounds [36]. Use of the research reactors constructed in the Turkey for the BNCT purposes has not been under consideration until 2014. Nowadays, there is an important attempt to utilize the ITU-TRR in treating the patients with BNCT method. In this manner, this study would give a significant contribution to the advancement of BNCT method in Turkey.

2. ITU TRIGA MARK II RESEARCH REACTOR

All information provided under this section is based on the Safety Analysis Report (SAR) [37] of ITU-TRR.

2.1 General Design Parameters of the Reactor

ITU-TRR, commissioned and became critical in 1979, was founded to operate under Nuclear Energy Institute of Istanbul Technical University (ITU), Istanbul, Turkey. It is a pool-type reactor, cooled by light-water, moderated by light-water and graphite, and reflected by a ring shaped graphite assembly. It operates with natural convective cooling by reactor pool water. The reactor generates a nominal power of 250 kW at full-power in a steady-state operation. The pulsed power operation is performed by step reactivity insertion when the reactor is at a power level of 1 kW at start-up. Maximum licensed peak power for the pulse experiment is limited to about 1200 MW. The reactor core components are illustrated in Fig. 2.1 for vertical view and Fig. 2.2 for radial view. The summary of geometry and material parameters of the reactor core components are listed in Table 2.1.

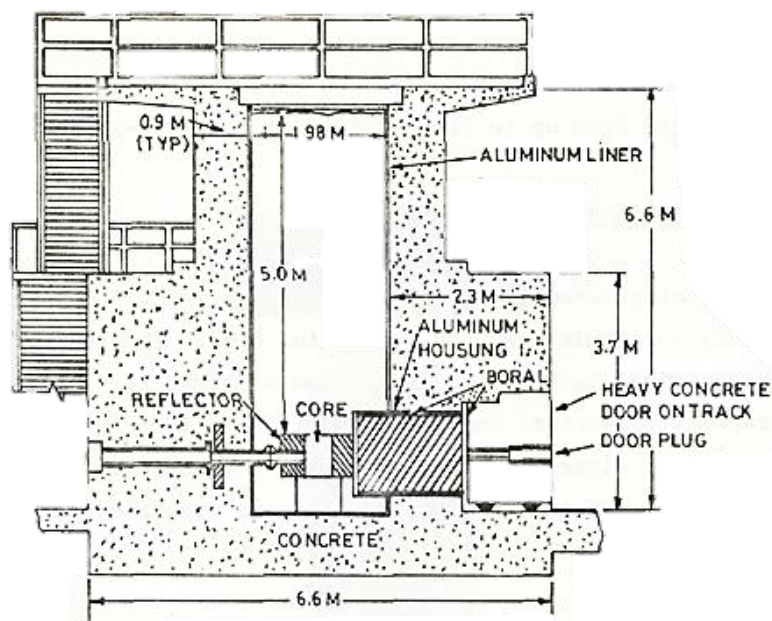


Fig. 2.1 The reactor core components of ITU-TRR (Vertical View)

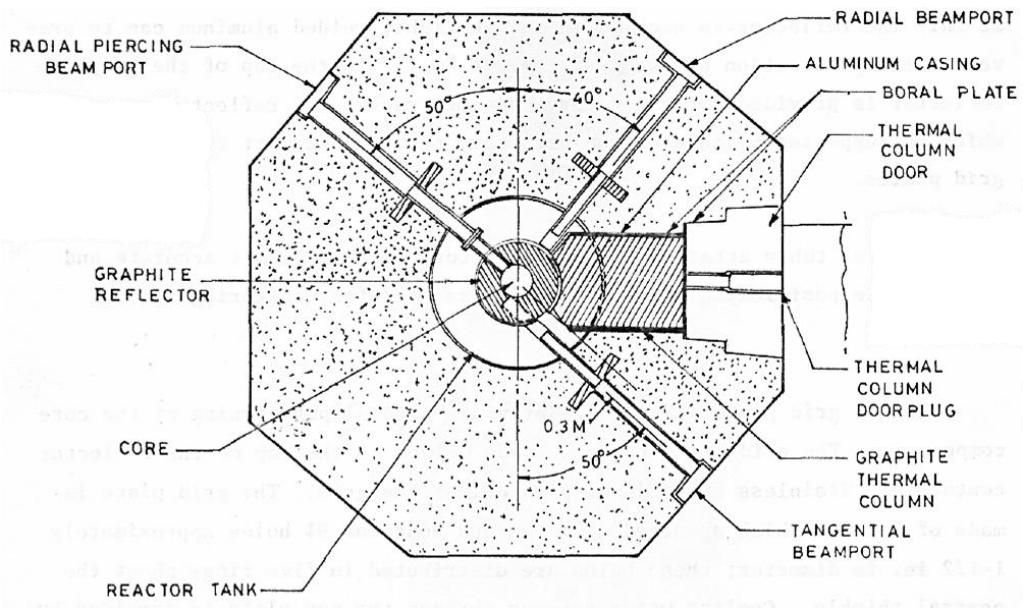


Fig. 2.2 The reactor core components of ITU-TRR (Radial View)

Table 2.1 Design parameters for ITU-TRR

Component	Dimension (cm)	Material
Core radius	21.80	
Reactor tank		
Radius	100	Anodized Aluminum
Thickness	0.635	
Height	640	
Grid plates	Top / Bottom	
Thickness	1.905	Anodized Aluminum
Hole diameter	1.905 / variable	
Fuel element		
Radius of zirconium rod	0.3175	Pure Zr
Fuel radius	1.8161	UZrH _{1.6} (20 w/o % ²³⁵ U in 8.5 w/o % U)
Fuel length	38.10	
Cladding thickness	0.0508	SS-304 Stainless steel
Axial bottom reflector length	8.8138	Graphite
Axial top reflector length	8.7376	
Total height	73.152	
End-fittings length	5.936	
Transient rod		
Guide tube outer diameter	3.8	Aluminum
Guide tube thickness	0.3	
Absorber length	38.1	B ₄ C
Absorber diameter	1.66495	
Cladding thickness	0.0508	6061-T6 Aluminum Alloy
Cladding length	41.275	
Regulating and safety rod		
Absorber length	38.1	B ₄ C
Absorber diameter	1.50876	
Cladding thickness	0.07112	6061-T6 Aluminum Alloy
Cladding length	41.275	
Reflector		
Thickness	30.48	Graphite
Height	55.88	
Cladding thickness	1.05	Anodized Aluminum
Beam tubes		
Radius	7.62	Barite Concrete
Thermal column		
Cross-sectional area	122 x 122	Graphite
Depth	168	

2.2 Fuel, Moderator and Control Rod Design

The core is composed of fuel elements, instrumented fuel elements, moderator elements, control rods, a source element, a pneumatic system and a central thimble. The core configuration is given in Fig. 2.3.

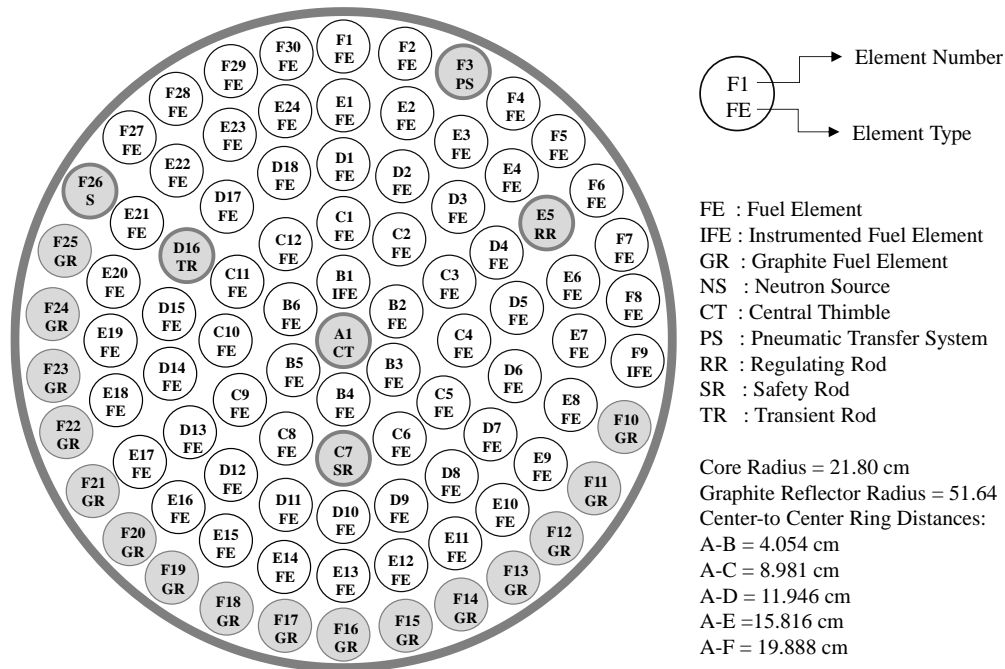


Fig. 2.3 Fuel-loading core map of ITU-TRR

Fuel-moderator elements comprise two parts: active part and moderator part. The active part has an annular fuel region containing a solid homogeneous mixture of uranium-zirconium hydride alloy ($U-ZrH_{1.6}$) and a pure zirconium rod at the center of the annular fuel region. The length of the active part (or active core length) is limited to be 38.1 cm. The nominal hydrogen-to-zirconium atom ratio is approximately 1.6. The solid fuel is made up of homogeneous mixture of uranium-zirconium hydride matrix containing about 8.5 % (by weight) U enriched to 20 % ^{235}U . Zirconium rod has a radius of 0.3175 cm with a density of 6.52 g/cm^3 . The moderator part contains two blocks of graphite, one above and one below the active part, acting as the top and bottom reflector for the core. The length of each graphite moderator region is 8.763 cm. The clad material made of stainless steel (type 304 SS) encases these two parts with a thickness of 0.508 mm. Both ends of the clad carry stainless steel end fittings with triangular spacers, which are attached to the grid plates. The overall length of the fuel element is 73.152 cm. General view of the fuel element is shown in Fig. 2.4.

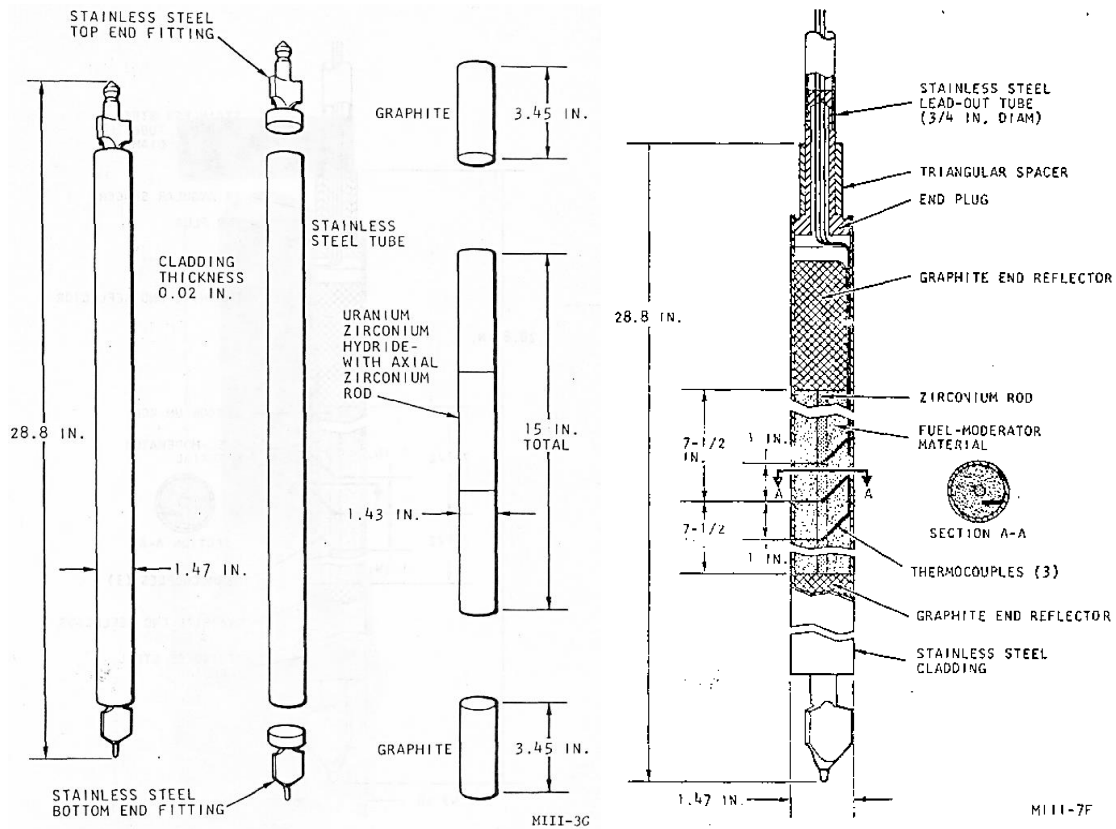


Fig. 2.4 TRIGA stainless steel clad fuel element with end fittings

An instrumented fuel-moderator element has three thermocouples embedded in the fuel. As shown in Fig. 2.4, the sensing tips of the fuel element thermocouples are located about 0.762 cm from the vertical centerline.

The empty holes on the core layout may be loaded with graphite dummy elements to provide additional moderation. These elements are all identical to fuel elements in dimensions and fabrication except that the active part of the fuel element is replaced with a block of graphite and also aluminum is used as the clad material.

Three different control rods are in use in the reactor core: safety, regulating and transient rods. Drive units provide mechanical motion for the control rods. Only transient control rod moves within hollow aluminum guide tubes. A control rod can be moved along the active core region from zero to a maximum of 38.1 cm. Absorber material of control rods is manufactured from boron carbide compacts (B_4C) and enclosed by 6061-T6 aluminum alloy. They are aligned and operate within perforated aluminum guide tubes. Each control rod is connected to a drive unit. Operation of the transient rod drive is controlled from the reactor console.

2.3 Fuel Density and H/Zr Atom Ratio

Standard TRIGA fuel contains 8.5 % U with an average ^{235}U enrichment of 20 % inside zirconium-hydride matrix. Density of the fuel directly depends on the hydrogen content, and it can be calculated as follows [38]:

$$\rho = \left(\frac{w_U}{\rho_U^0} + \frac{1-w_U}{\rho_{\text{ZrH}_x}} \right)^{-1} \quad (\text{Eq. 2.1})$$

where w_U is uranium content of the matrix fuel in units of weight percent (%); ρ_U^0 is density of the uranium in room temperature with 19.9 g/cm^3 and, ρ_{ZrH_x} is the density of zirconium-hydride matrix and can be expressed as follows [39]:

$$\rho_{\text{ZrH}_x} = 1 / (0.1541 + 0.0145x) \text{ for } x < 1.6 \quad (\text{Eq. 2.2})$$

$$\rho_{\text{ZrH}_x} = 1 / (0.1706 + 0.0042x) \text{ for } x \geq 1.6 \quad (\text{Eq. 2.3})$$

where x is hydrogen-to-zirconium atom ratio ($N_{\text{H}}/N_{\text{Zr}}$).

U-ZrH_x fuel matrix has a nominal hydrogen-to-zirconium of 1.6; however, Simnad [39] emphasizes that the value ranges from 1.5 to 1.7. On the other hand, this study uses H/Zr ratio of 1.65¹ as the SAR does not indicate any certain value. Hence, fuel density is calculated to be 5.985 g/cm^3 .

2.4 Reactor Tank, Grid Plate and Reflector Assembly Design

A central thimble to conduct experiments and/or to irradiate small specimen is positioned to the core center (the location where the maximum flux occurs). It is normally filled with water²; however, this mass of water may be discharged in order to obtain a well-collimated beam of neutrons. The thimble outer diameter is 3.81 cm that fits through the center hole between the top and bottom grid plates.

A pneumatic transfer system in aluminum tubing is typically located in the outer ring of the core, in particular in a region of high neutron flux, to produce short-lived radioisotopes. The

¹ In the report by the GA Technologies prepared for the USA-DOE [40], stainless steel standard fuel elements (% 8.5 U with 20% enrichment) has an H/Zr atom ratio of 1.7. Moreover, the nominal value provided by the GA in the IAEA report [41] is 1.60. In a different report [42], 1.60 is used in the research. Finally, in the studies performed by El Bakkari [43], Böck and Villa [44], and also in TRIGLAV [45] code, an atom ratio of 1.65 is used for the same fuel type.

² According to the SAR, reactivity effect of the central thimble that is filled with void is calculated to be $-0.6 \text{ } \Delta k/k$.

tube is filled with air and for the modelling purpose considered as air (or void)³. The outer diameter of the tube is 3.175 cm.

The core is surrounded by a ring-shaped block of graphite that serves as a reflector for the neutrons escaping from the core. The block is covered with leak-tight welded aluminum clad to avoid corrosion due to water. It is radially 30.48 cm thick with a height of 55.88 cm.

A rotary specimen-rack⁴ is embedded to the top of graphite reflector assembly in a well for large-scale radioisotope production and, the activation and irradiation of small samples.

The top and bottom grid plates are fabricated from aluminum alloy (anodized aluminum), which support the reactor core components and provide horizontal positioning to them. The top grid plate is welded on the top of the reflector and nailed with stainless steel pins. The grid plate holds 91 holes with a diameter of about 3.81 cm, distributed in five rings around the central thimble. The bottom grid plate also contains 91 holes with varying diameters. Cooling water passage through the top plate is provided by the differential area between a triangular spacer block on top of the fuel element and the round hole in the grid. Small holes at various positions in the top grid plate permit insertion of foils into the core to obtain flux data.

The reactor tank has a diameter of about 2 m with a thickness of 6.35 mm and a height of 6.40 m. Tank is fabricated with aluminum material and welded to obtain a leak-tight boundary.

2.5 Beam Ports and Thermal Column Design

Fig. 2.2 shows three BPs in the reactor: radial, tangential and piercing. The BPs are located at the core perimeter in order to provide neutron flux and gamma beam for various irradiation experiments. Each one is designed to function for a specified neutron spectrum. BPs are 7 cm below from the core center due to the position of the rotary specimen-rack inside the graphite reflector. Geometric properties of BPs are listed in Table 2.2.

Table 2.2 Geometric Properties of BPs

Name	Diameter (cm)	Total Length (cm)
Radial	15.24 to 20.32	277
Piercing	15.24 to 20.32	307
Tangential	15.24 to 20.32	330

³ The use of void/air instead of water reported in the SAR accounts for an excess reactivity of -0.15 % $\Delta k/k$.

⁴ The filling material can be void/air or water; General Atomics [37] provides that the reactivity effect due to void usage is -0.15 % $\Delta k/k$.

All of the BPs are identical in diameter, but not in length. Piercing radial and tangential BP begin from the inner surface of the graphite reflector and reach out the outer surface of the reactor concrete shield by, in turn, passing through the section of graphite reflector, water and concrete. In addition, the radial BP extends from the outer surface of the graphite reflector to the outer surface of the reactor concrete shield. All of the BPs have an inner diameter of 15.24 cm with a 0.80 cm thick aluminum cladding. However, later, the diameter increases to 20.32 cm.

BPs normally filled with air are choked up with the wood-lead plug-ends until an experiment is performed. In the experiments, plug-ends are removed, and specially designed collimators/patterns are placed into the BP hole.

3. MONTE-CARLO MODEL OF THE REACTOR

This section gives details of MC model of the core and the PBP of ITU-TRR.

3.1 Reactor Core

A 3-D full-core modelling of the reactor is performed using MCNP5 [46] (the code is detailed in Section 3.6.1). The data used in the modelling for geometry, materials and neutronic parameters is, in general, based on Safety Analysis Report for the TRIGA MARK II Reactor [37]. To minimize the systematic and modelling errors emanating from uncertainties (e.g., assumptions, approaches and applied methods), all of the core components (referring to Section 2) are, practically, transferred to the MCNP. A full core calculation is performed since the reactor is not symmetric. Radial (left) and vertical (right) view of the reactor in the MCNP model are presented in Fig. 3.1.

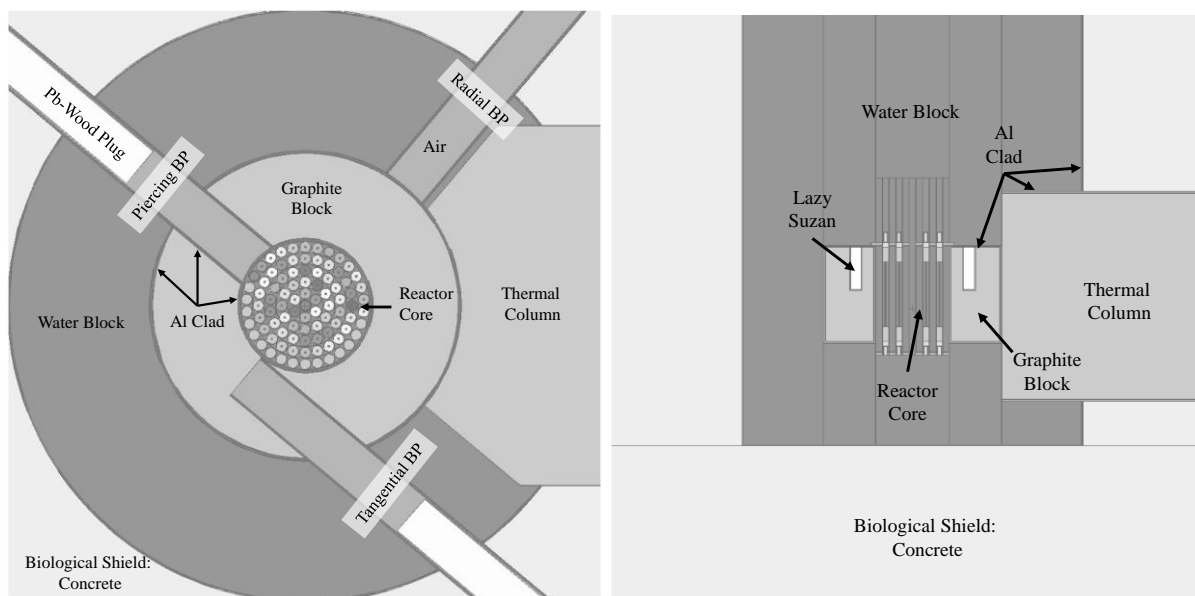


Fig. 3.1 Radial (left) and vertical (right) view of the reactor core in the MCNP model MC model incorporates neutron transport calculation with photon transport and photo-nuclear reaction calculations. More, photon interactions are taken into account by using PHYS card.

For the low energy neutrons (<4 eV), thermal scattering behavior related with crystal structures and chemical bounds is taken into consideration. Free gas approximation with regard to the thermal motion of adjacent atoms is considered for H_2O , Graphite, H in ZrH and Zr in ZrH.

The modeling is performed for CZP and HFP. The CZP is modeled to make only validation of the reactor model while the HFP is modeled for the burnup calculation and BP design.

3.1.1 Cold-Zero Power Condition

CZP (at low power) at the temperature of 23 °C (296 K) is taken into account for all the materials inside the core; thus, the feedback effects on the neutronic computations are assumed to be negligible. More, effect of burnup is not included due to the fresh core assumption.

The analyses are performed by using ENDF/B-VII.0 [47], ENDF/B-VI.8 [48], JEFF-3.1 [49] and JEFF-3.1.1 [50] libraries to observe the effect of the cross-section libraries assembled by different compilers.

3.1.2 Hot-Full Power Condition

In the case of HFP, the reactor is assumed to operate at a power level of 250 kW at a steady-state operating condition. Control rods are set to the positions where the considered operation sequence is performed.

Feedback effects caused by a change in the density and cross-section of materials due to a change in material temperatures are taken into account; however, they are assumed to be invariant. For this purpose, average material temperatures are set to 380 K for the clad, 450 K for the fuel, 540 K for pure zirconium rod, 310 K for water inside the core and 300 K for the rest of structures, respectively. As the zirconium rod is located at the center of the fuel region, average rod temperature nearly equals to maximum temperature of the fuel (to inner surface temperature) and thus, naturally would be higher than that of the fuel. For that purpose, NJOY module is used to generate the neutron cross-sections at the operating temperatures as well as photo-atomic and photo-nuclear reaction libraries.

3.2 Temperature-dependent Cross-Section Generation

NJOY99 with an update 396 [51] [52] is used to generate the neutron cross-sections at the specific material temperatures as well as photo-atomic and photo-nuclear reaction libraries. Thermal scattering libraries are also produced for the water and graphite, and the zirconium hydride fuel. A flow diagram of NJOY is presented in Fig. 3.2.

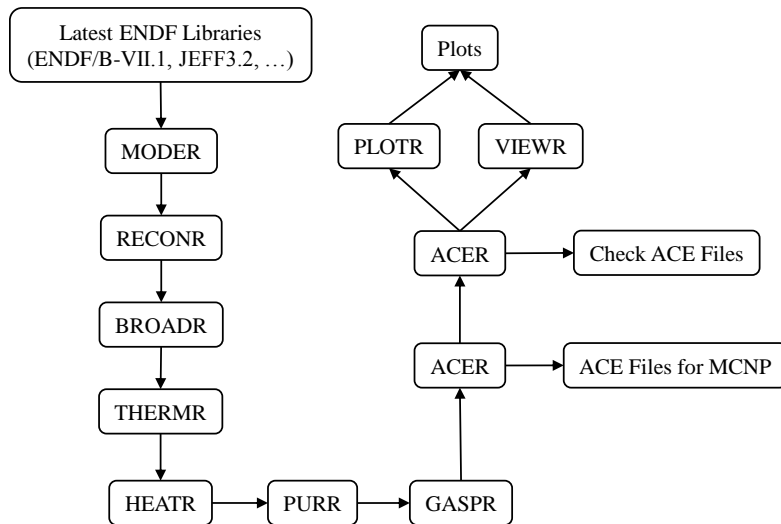


Fig. 3.2 NJOY99 Flow Diagram

As the nuclear data processing code, NJOY is made up of a set of modules such as MODER, RECONR, and BROADR. Each module (job details of the modules are given in Section 3.6.3) performs a separate task to produce final form of the cross-sections. As the required input parameters for each module are almost automatized by the code developers, default values of the parameters, which are appropriate for most of the problems, are used. Yet, the code still needs somewhat user knowledge to open the optional cards. Cross-sections can be generated for any desired temperature/reaction/particle of the selected isotope(s). In brief, after a great deal of straightforward calculation, the code produces ACE formatted files for the MCNP code and several control plots to check the ACE files⁵. Evaluated Neutron Data Files (ENDFs) primarily come from the updated ENDF/B-VII.1 library [53]; however, JEFF3.2 [54], CENDL3.1 [55], JENDL4.0 [56] and TENDL2013 [57] are used for the isotopes that are not in the used library.

3.3 Burnup-Dependent Neutron Spectrum Calculation for the BP

The main aim of this step is to obtain a burnup-dependent incoming neutron/photon spectrum for the BPs to be used in the subsequent calculations. Since the spectrum in the BPs strictly depends on the burnup and the power level of the reactor, effect of burnup on the incoming neutron spectrum of PBP is investigated. Therefore, the neutron and photon spectra are obtained at the burnup level of the specific reactor operation sequence in order to include the burnup effects into the simulation results.

⁵ The criticality test of the ACE libraries is carried out using the ‘International Handbook of Evaluated Criticality Safety Benchmark Experiments (OECD-NEA ICSBEP)’.

Burnup-dependent neutron spectrum is obtained by using the position of the CRs inside the core. Criticality during a particular reactor operation is ensured by moving the CRs upward or downward inside the core. However, the positions of the CRs inside the core are very peculiar to the reactor operation sequence. This means that burnup values of the fuel elements can be properly calculated using an MC based burnup-depletion code if the reactor is modeled at the conditions similar to the considered operation sequence. Operational data contain the information about not only the positions of the CRs, but also about the material temperatures, reactor power history and the latest core map. According to the method, any operational data (preferably the most recent) are defined in the MC model of the reactor. Subsequently, fuels are burned using a burnup code until the excess reactivity⁶ of the core becomes zero. Once the excess reactivity falls down below zero, the reactor theoretically cannot maintain its criticality and, finally shuts itself down.

The up-to-date burnup calculation is carried out using the reactor operation sequence of 1599 (# 1599) recorded into the ITU-TRR log-book in March 2013. During the operation, transient and safety rods were set to 96.89 % and 94.89 % of their full positions, respectively. Position of the regulating rod inside the core was not fixed during the operation in order to maintain criticality; however, an average value of 83.83% is used in the MC calculation. An MCNP representation of the reactor including reactor core, BPs, thermal column and, water and graphite blocks is presented in Fig. 3.1. Core loading map used in the burnup calculations is shown in Fig. 2.3.

It should be noted that photon calculation is not a necessity for a burnup calculation.

MONTEBURNS2 [58] [MCNP5 linked with ORIGEN2.1], a fully-automated burnup depletion code, is used to calculate the burnup of fuel elements. The code description is presented in Section 3.6.2. The code requires four separate input files, MCNP, MONTEBURNS, feed and cross-section input files. MCNP input file comes from the reactor model generated in Section 3.1. MONTEBURNS input file is created; input parameters are set to 9 for outer burn steps (outer iteration for convergence), 100 for internal burn steps (inner iteration for convergence), no intermediate k_{eff} calculation (initial guess for subsequent steps) due to no feed, and zero fractional importance to take all of the FPs into account. Simply, no feed indicates that no fuel is loaded into the core during the burnup calculation. The justification for that is that the reactor records show, thus far, no change in the recent reactor core

⁶ The amount of surplus reactivity that is needed to compensate for decrease of fissile content and accumulation of the FPs.

configuration. Furthermore, if the fractional importance is set to zero in the input file, it means that contribution of each FP calculated in the ORIGEN2, even negligible ones, is to be calculated by the code. For the contribution of only major FPs, the fractional importance should be one. On one hand, ORIGEN2 requires an initial cross-section library to initiate the burnup calculation. Unlikely, an initial library for a TRIGA Mark II has not been provided by Radiation Safety Information Computational Center (RSICC); thus, the required library, entitled TRIGA, is produced from a previous test run. For tally calculations, a total of 250 critical isotopes, including FPs and actinides, are chosen. A feed input file is also prepared; the time steps are selected to be 3 days (from user experience) for the FPs equilibrium and 20 days for the rest. More, no feed or discharge from the reactor core during the irradiation is considered. The cross-section input file contains a list of transmutation cross-sections for a total of 533 isotopes. Since the power history is not represented accurately in the log book, the reactor is considered to be operated at a constant power of 250 kW. However, constant power approach limits the accuracy of fuel burnup calculation as the accumulation and depletion of the FPs directly depend on power level of the reactor. The most important impact of this simplification is that the user is obligated to make an assumption of FP equilibrium in burnup calculation. A computational flow diagram of burnup calculation is shown in Fig. 3.3. The output of the code gives burnup values as a function of core multiplication factor (or in terms of reactivity). For an accurate burnup calculation, Non-Linear Reactivity Model (NLRM) [59] is employed. Therefore, a second order curve fitting for the Eq. (1) is performed assuming a single-batch core. Using the equation, burnup can be easily calculated by setting the fitted equation to zero [$\rho(B) = 0$].

$$\rho(B) = A_2 \times B^2 + A_1 \times B + A_0 \quad (\text{Eq. 3.1})$$

where A_2 [$1/(\text{MWh})^2$], A_1 [$1/\text{MWh}$], A_0 are the fitting constants, and B [MWh] is the specific burnup.

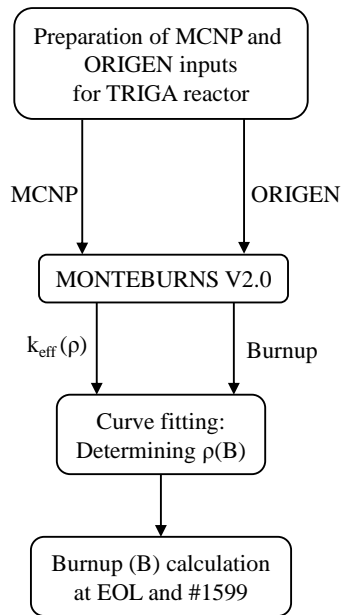


Fig. 3.3 Computational flow diagram for burnup calculations

3.4 Beam Ports

The BP calculations are carried out using MCNP6.1⁷ [60] code. Radial view of the PBP in the MCNP model is presented in Fig. 3.4.

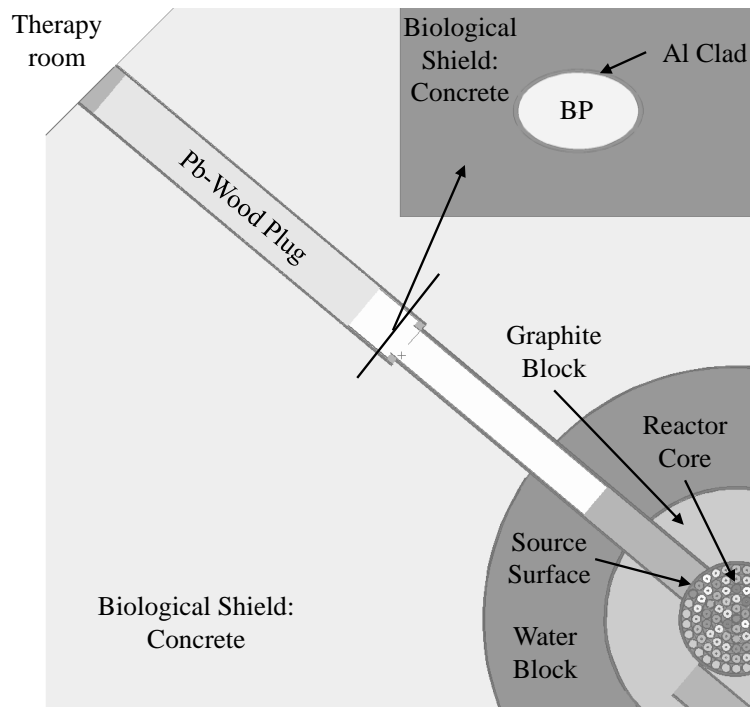


Fig. 3.4 Radial view of the PBP in the MCNP model

⁷ Note that MCNP5 is the previous code used to analyze reactor model in this study. The reason why the code is changed to a newer version is that the newest version of MCNP gets the solutions about 25 % faster than the previous one, MCNP5.

It is very important to note that the BP model is based on the values given in the SAR of the reactor. Yet, the BP has undergone several changes as the time goes by. Unfortunately, the MC model does not carry these modifications as well as the design changes, fabrication uncertainties and material property differences.

In calculations, neutron and photon physics (without the bremsstrahlung effect) are taken into account by using the PHYS card. In addition, low energy (less than 0.4 eV) interactions of neutrons with atoms are modelled with S (α , β) approach for H₂O and Graphite.

To reduce the computational time in the MC calculations, the criticality calculations are discarded from the deep penetration transport calculations for the BPs. For this purpose, the calculations are divided into two separate parts as the reactor core calculation (Eigen-value problem) and BP calculations (deep penetration problem). First part covers only the criticality calculation such as estimation of the effective multiplication factor, validation and testing of the reactor model, and burnup-dependent neutron/photon spectrum. Furthermore, the first part is used to create a source file to be used in the second part. For this purpose, a source surface for the interested BP is defined, and all the particles that pass this surface are written into a surface source file. The location of the source surface is illustrated in Fig. 3.4. The created source file contains important information about the particles such as energy, position and trajectories. In the second part, reactor core region is excluded from the BP model. That is, the BP is modeled separately. All the calculations in the PBPs are performed by using the created source file.

3.5 Input Parameters for the Reactor Physics Code

For reactor model validation and testing, MC calculations are performed by using 10000 neutrons per stage for 200 passive cycles and 1500 active cycle run about 15 million sampled neutrons per calculation. The continuous energy .03c neutron cross-section sets are used in the evaluation of reaction rates at 300 K and the standard .04p photon cross-section sets are used.

In HFP case of criticality calculations, one million neutrons per cycle with 100 passive and 1500 active cycles are used.

In the burnup calculations, KCODE criticality calculations use 10 000 neutrons per cycle with 50 passive and 500 active cycles. The provided neutron history yields a relative error of less than 0.0007 for the core multiplication factor. Typically, sensitivity of the multiplication factor for an accurate calculation should be less than 0.1 %.

During the creation of surface source file for the PBP, the number of neutrons per cycle with 100 passive and 1600 active cycles is chosen so that it would yield a maximum relative error of 0.00012 for the neutron fluxes. The neutron/photon/photo-atomic libraries used in the calculations come from the continuous-energy ENDF/B-VII.1. For the BP materials, the neutron cross-sections are used at the room temperature (300 K).

F2 surface flux tally (particles/cm².s), F4 tally (particles/cm².s) for flux averaged over a cell, F5 detector tally⁸ and FMESH (particles/cm².s) for defining a mesh tally averaged over a mesh cell are used for tally purposes.

In all calculations, the group energy boundaries are 0-0.625 eV for thermal, 0.625 eV-0.1 MeV for epithermal and 0.1 eV-20 MeV for fast neutrons. For the neutron spectrum calculations, number of energy groups are defined as 1195 for the particles. The group energy boundaries are based on 238-group ENDF/B-V.

Output of tallies is converted to the flux values by multiplying with a constant of C (using tally multiplier card):

$$C = \frac{\nu \times P \times 10^6 \text{ (W/MW)}}{1.602 \times 10^{-13} \text{ (J/MeV)} \times k_{eff} \times Q_{ave}} \quad (\text{Eq. 3.2})$$

where the average number of neutrons produced per fission, ν , is 2.438; reactor power of P is 250 kW; effective multiplication factor, k_{eff} , changes with the burnup, and average fission energy produced from all fissionable material, Q_{ave} , is about 200 MeV.

SSW card is used to create the source file; SSR card is used to read the particles from the source file. To lower the computational errors resulted from the nature of deep penetration problem, a number of variance reduction techniques are implemented into the simulation. A combination of Russian roulette for energy and weight, geometry splitting (IMP), energy splitting (ESPLT), forced collision (FCL), energy/weight cutoff (CUT), population control (NPS), DXTRAN sphere with cell contribution and point detector with detector contribution (PD) is used to reduce the relative errors of neutron group fluxes in the BP to acceptable levels⁹. The source is biased by defining an isotropic angular flux on the source. This option is useful for the point detector and DXTRAN sphere.

⁸ Same unit with F2 tally.

⁹ In a MC calculation, relative error must be less than 0.1 for a tally except detector tallies. Otherwise, it should not be greater than 0.05 for the detector tallies.

3.6 The Used Codes

3.6.1 MCNP5/6.1

MCNP5/6.1 is a general-purpose Monte Carlo N-Particle code that can be used for neutron, photon, electron, or coupled neutron/photon/electron transport. It also has a capability of calculating the multiplication factor for the critical systems. The code treats an arbitrary three-dimensional configuration of materials in geometric cells bounded by first- and second-degree surfaces and fourth-degree elliptical tori.

Point-wise cross-section data are used. For neutrons, all reactions given in a particular cross-section evaluation (i.e., ENDF/B-VII.1) are accounted for. Thermal neutrons are simulated by both the free gas and S (α , β) models. For photons, code accounts for the incoherent and the coherent scattering, the possibility of fluorescent emission after photoelectric absorption, absorption in pair production with local emission of annihilation radiation, and bremsstrahlung.

3.6.1.1 Cards Used for the Tally Purpose

In MCNP calculations, necessary computational outputs that the code users want to get are obtained by using the tally cards provided by the code. For this purpose, the Fn cards are defined together with the auxiliary cards. Not only the cards can be used separately but also using a combination of those cards is possible. The used cards in this study are introduced briefly as follows:

Tally	Definition	Unit
F1	Current integrated over a surface	particles
F2	Flux averaged over a surface	particles cm ⁻²
F4	Flux averaged over a cell	particles cm ⁻²
F5	Flux at a point detector	particles cm ⁻²
FMESH	Flux averaged over a mesh cell	particles cm ⁻²

The F1 tally calculates current for which the particles cross a defined surface. It simply gives the sum of the weights (W) of the particles; that is, there is no division by surface area. Moreover, it is the sum of the partial currents across a surface (crossing in the positive and negative directions to the surface). The tally can be expressed as in Eq. 3.3

$$F1 = J = \int_A dA \int_E dE \int_{4\pi} d\Omega n \cdot J(r_s, E, \Omega) \quad (\text{Eq. 3.3})$$

where n is the surface normal in outward direction at r_s .

The F2 tally calculates particle flux for the particles which cross a defined surface. The contribution of each particle to the tally is $W./sec\theta/A$ if the particle has a weight of W and an angle of θ with surface normal, and the surface area is A . The flux depends on energy, space and angular distribution; therefore, the tally is given as follows

$$F2 = \bar{\phi}_s = \frac{1}{A} \int_A dA \int_E dE \int_{4\pi} d\Omega \Phi(r_s, E, \Omega) \quad (\text{Eq. 3.4})$$

The F4 tally calculates average particle flux within a defined cell. Each particle makes a particular contribution of WT/V to the flux in the cell where the W is used to define the weight of the particles, T is the track-length and V is the volume of the interested cell. Total contribution to the tally can be found using following formula

$$F4 = \bar{\phi}_V = \frac{1}{V} \int_V dV \int_E dE \int_{4\pi} d\Omega \Phi(r, E, \Omega) \quad (\text{Eq. 3.5})$$

FMESH tally calculates the track length estimate of the particle flux averaged over a mesh cell. This tally is very similar to F4 tally; but, in this case, an interested cell is divided into a number of sub-cells.

The F5 tally estimates particle flux at a point in space in a deterministic way. It is a kind of limiting case of F2 surface flux. Contributions to the point/ring detector come from the source and collision events throughout the random walk. The contributions to the fluence at the detector are given by

$$\delta\Phi = \frac{W \mu(E, \theta_s)}{\mu(E)r^2} e^{-\mu(E)r} \quad (\text{Eq. 3.6})$$

where E is the energy of the particle after collision and W is its weight. $\mu(E, \theta_s)$ is the linear interaction coefficient per steradian for scattering angle θ_s .

3.6.1.2 Variance Reduction Methods

For an acceptable MC calculation, sufficient precision is a must. However, computing time directly depends on the interested sufficient/rational precision. Under this particular circumstance, most users are forced to make a selection between precision and the run-time. To solve the mentioned dilemma, a number of variance reduction methods have been developed. Frequently used variance reduction techniques are shortly described below. Before that, efficiency of the MC calculations have to be measured by using variance and computing

time. In this manner, the Figure of Merit (FOM) perfectly shows if a problem is well-sampled or not. The FOM is simply defined as

$$FOM = \frac{1}{\sigma^2 t} \quad (\text{Eq. 3.7})$$

where σ is the relative standard deviation of the mean, and t is the computational time for the calculations.

Geometry Splitting/Russian Roulette: The method, simple and widely used variance reduction technique, is based on defining an importance function on an interested surface/cell. The method divides the geometry into cells, assigns an importance (I_n) to each cell and decides which technique (splitting or roulette) is to be selected according to the ratio between cell m and cell n . If the importance ratio ($v=I_n/I_m$) between cell m (I_m) and cell n (I_n) is greater than 1, then particles split into v track. If the importance ratio is less than 1, then particles play Russian roulette. Otherwise, particles are transported to next cell without employing variance reduction.

Time/Energy Cutoff: The time/energy cutoff provides user to define a problem-wide time/energy interval. If the particles fall below a defined time/energy cutoff value, they are killed. The most beneficial effect is to decrease the required time per history.

Energy Splitting/Roulette: This method is very similar to geometry splitting; but, in this case energy of a particle is divided into the number of same particles.

3.6.2 MONTEBURNS2

MONTEBURNS2 [MCNP5 linked with ORIGEN2.1], a fully-automated burnup depletion code, is used to calculate the burnup of fuel elements. The code requires four separate input files, MCNP, MONTEBURNS, feed and cross-section input file. MONTEBURNS produces large number of criticality and burnup results based on various material feed/removal specifications, power(s), and time intervals. The program processes input defined by the user that specifies the system geometry, initial material compositions, feed/removal specifications, and other code-specific parameters. Various results from MCNP, ORIGEN2, and other calculations are then output successively as the code runs. The principle function of MONTEBURNS is to transfer one-group cross-section and flux values from MCNP to ORIGEN2, and then transfer the resulting material compositions (after irradiation and/or decay) from ORIGEN2 back to MCNP in a repeated, cyclic fashion. The basic requirement of the code is that the users have a working MCNP input file and other input parameters; all interaction with ORIGEN2 and other calculations are performed by MONTEBURNS.

3.6.3 NJOY

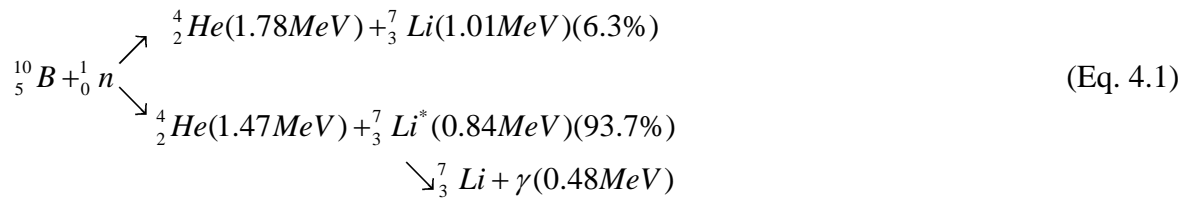
Nuclear Data Processing System, shortly called NJOY, produces point-wise and multi-group cross-sections from Evaluated Nuclear Data for a variety of particle transport/diffusion codes including MCNP. NJOY consists of a number of modules, each of which is coded to perform a separate task; however, only the used modules are introduced related with the scope of this study. As shown in Fig. 3.2, the modules used to produce ACE cross-section files consistent with MCNP are MODER, RECORN, BROADR, THERMR, HEATR, PURR, GASPR and ACER, respectively. In NJOY, MODER is used to convert binary-to-ASCII or ASCII-to-binary mode; RECORN is used to reconstruct resonance cross-sections from resonance parameters; BROADR is used to generate Doppler-broadened cross-sections; THERMR is used to generate point-wise neutron scattering cross-sections in the thermal energy range; HEATR is used to generate point-wise heat production cross-sections and radiation damage energy production for the specified reactions; PURR is used to produce probability tables for MCNP; GASPR is used to add gas production reactions; ACER is used to prepare libraries in ACE format for MCNP. Apart from the mentioned modules, there are a number of distinct modules used to verify the produced neutron cross-sections. ACER is capable of making a series of consistency checks and produces several plot files for which VIEWR module prepares the plot files as Postscript file. Furthermore, PLOTR is very useful when the generated cross-sections are compared with the raw data of ENDF file.

4. REQUIREMENTS FOR BNCT APPLICATION IN RESEARCH REACTORS

4.1 Introduction to BNCT Application

Neutron Capture Therapy (NCT) is an experimental radiation technique based on the theory of destroying the selectively targeted deep tumors with heavy charged particles created after thermal neutron capture process of a particular isotope inside the tumor cells. The isotopes suitable for the NCT are the specific atoms which have a huge thermal neutron capture cross-section. The candidate materials such as ^3He , ^{10}B , ^{157}Gd and ^{113}Cd are used as chemical agents which are selectively taken up by the tumor cells. When ^{10}B , which has been widely used in the world due to its chemical properties, is used for the purpose of NCT, the method is referred to BNCT. Similarly, GdNCT method uses ^{157}Gd isotope instead of ^{10}B .

The benefit of the BNCT method is to destroy the tumor cells selectively which are fed with a boron containing chemical compound, so-called boron delivery agents. The method works well even the tumor cells spread out in the healthy tissue. The reaction $^{10}\text{B} (n, \alpha) ^7\text{Li}$ is



The created heavy particles lose their energies within a cell, typically in less than 10 μm . Stopping powers of alpha and lithium are 150 MeV/mm and 175 MeV/mm.

Depth and position of the tumor cells determine the energy of the source neutrons to be used in BNCT. Superficial tumors are irradiated with thermal neutrons (< 0.4 eV) while the tumors seated deeper than 8 cm are irradiated with the epithermal (0.4 eV $< E < 10$ keV) and fast neutrons (> 10 keV). As the epithermal/fast neutrons penetrate deep into the tissue, they lose their energies due to scattering and slow down to thermal energies at the tumor site. The thermalized neutrons make absorption interaction with the tumors containing boron compound. Such reaction, given in Eq. 4.1, produces a very high radiation dose in the cancerous cells.

It is important for BNCT to be successful that not only high energy neutron beams have to be employed but also high tumor concentrations of ^{10}B and a high tumor to normal tissue ratio must also be achieved. A well-efficient boron-included chemical agent development is one of the key parameter for a successful BNCT.

4.2 Desired/Undesired Neutron Beam Characteristics

One of the key aspects of beam (port) design is to maximize the desired epithermal neutrons. Thus, the major objective in applying the BNCT is to increase the epithermal flux as high as possible while all other radiation types in the incident beam are minimized.

IAEA technical document [61] reports that the range of dose from the epithermal flux component is from 2.5 to 13×10^{-13} Gy cm² per epithermal neutron in existing facilities. A target number is estimated to be 2×10^{-13} Gy cm² per epithermal neutron. Epithermal energy range is in the range of 0.4-0.6 eV and 10 keV.

The studies performed earlier indicate that a minimum epithermal neutron flux of 10^9 n cm⁻² s⁻¹ is desired in the incident beam. However, a lower epithermal neutron flux ($> 5 \times 10^8$ n cm⁻² s⁻¹) can be used in irradiation; but, this situation would lead to an increase in irradiation period (within a reasonable treatment time) of the patient. In addition to longer irradiation period, sustaining the necessary boron concentration in the tumor cells till the end of the total required irradiation time may not be achievable if the beam intensity is lower than the desired value. This is because the tumor boron concentration completely depends on the used beam intensity. Higher epithermal neutron flux ($> 10^9$ n cm⁻² s⁻¹) means much lower irradiation period. However, it should be noted that besides high epithermal neutron flux, an improved beam quality is crucial in performing the BNCT. The reason is that the beam has a number of undesirable characteristics such as containing photon fluence and thermal neutron flux. In such application, one should make a decision between a better quality and more intensity.

Energy range of the fast neutrons is assumed to be higher than 10 keV (up-to-20 MeV). A beam of neutrons generated in a research reactor core inevitably contains fast neutron flux which has a number of undesirable characteristics such as production of high LET (Linear Energy Transfer) protons. These protons are very harmful for the healthy cells. Therefore, it is important to reduce the fast neutron flux of the incident beam as low as possible for the BNCT application.

Photons interact not only with tumor tissue but also with a large volume of healthy tissue as they have a wide energy range of several keV to MeV. Therefore, it is important to eliminate photon fluence from the beam as much as possible. Furthermore, there is somewhat gamma dose contribution due to the neutron capture reaction of boron inside the patient. Although a desired target value is 2×10^{-13} Gy cm² per epithermal neutron, in existing facilities the value changes from 1 to 13×10^{-13} Gy cm² per epithermal neutron.

To reduce radiation damage to the skin tissue as low as possible, thermal neutron contribution of the incident beam needs to be minimized. A well-adjusted beam of neutrons has a ratio of epithermal flux to thermal flux of 20.

Another important parameter for an incident neutron beam is the ratio of neutron current to neutron flux at the port exit. A desired ratio is intended to be greater than 0.75. As the value increases, fraction of the particles traveling in the forward direction (and thus depth dose) increases and is kept almost constant with the distance from the port. A higher value limits spread of the particles from the beam center and prevents the undesired irradiation damages to the healthy tissues enclosing the tumor cells. Furthermore, a higher value allows somewhat flexibility to the patient positioning along the beam central far from the port exit without losing the availability/efficiency of the beam intensity.

The last issue with the BNCT application is the determination of the size of beam apertures. In present research facilities, adjustable circular (and square) shape and size ranging from 0-16 cm in diameter for brain are opted. They are shaped according to the tumor size and position.

A summary of the desired neutron beam characteristics for the BNCT application is tabulated in Table 4.1.

Table 4.1 Desired neutron beam characteristics for the BNCT application [61] [62]

Neutron Energy	0.4-0.6 eV < E < 10-20 keV
$J_{\text{epith}} / \Phi_{\text{epith}}$	> 0.75
Beam Aperture	Adjustable size and shape, 0–16 cm diam. for brain
Epithermal Neutron Flux	> $1 \times 10^9 \text{ n cm}^{-2} \text{ s}^{-1}$
Patient Irradiation Period	~ 10 min
Penetration Depth	> 8 cm
Thermal/Fast/Gamma Dose Contributions	< $2 \times 10^{-13} \text{ Gy cm}^2$
Epithermal Neutron Dose Contribution	> $2 \times 10^{-13} \text{ Gy cm}^2$
$\Phi_{\text{epith}} / \Phi_{\text{th}}$	> 20

To obtain the desired beam, so far, several methods have been developed and used widely. The methods are introduced in detail in the subsequent section.

4.3 The Methods to Design the Beam (Port)

There are three primary methods to design the beam (port) and to obtain an appropriate neutron beam at the considered location, which is outside of the research reactor core. These are spectrum shifting, filtering and collimation methods.

For a beam (port) design, the spectrum shifting method or filtering method or collimation method or a combination of them is usually applied by taking the application requirements into

account. IAEA [61] suggests for the research reactors that spectrum shifting and filtering methods should be employed together to get a better beam of neutrons.

The role of spectrum shifting method in the beam (port) design is to slow down the fast particles (neutrons) into an appropriate energy interval (namely, epithermal) which is suitable for the BNCT. However, the final energy of the particles can be thermal or epithermal.

Filtering method aims to eliminate the undesired particles or parts or energies of the incident beam while allowing the desired component of the beam to transmit in the BP. In the filtering method, the most important issue is to keep the desired part of original source flux value as high as possible.

Collimation method is used to form a well-adjusted forward-directed beam of neutrons along the beam central axes and to improve the neutron current to flux ratio at the port exit. As discussed above, it gives flexibility to the patient in positioning and provides an increased deep dose.

Various facilities in the world have used those mentioned three methods to enhance the capability of their BPs or thermal columns. In this manner, they have suggested a number of materials suitable for BNCT. Some common materials studied in the literature are presented in Table 4.2.

Table 4.2 Materials used to design the epithermal neutron beam in various research reactors

Spectrum Shifters or Fast Neutron Filter	Filtering	Photon Attenuator
Aluminum and its compounds (Al ₂ O ₃ , Flualtal, AlF ₃)	Al	Bi
H ₂ O, D ₂ O	Li and its compounds	Pb
Teflon	Cd (Cadmium)	Ar in liquid form
MgF ₂ (Magnesium Fluoride)	Ti (Titanium)	Poly-B
Lithium and its compounds (LiF, Li ₂ CO ₃)	B (Boron)	LiF ₃
Beryllium and its compounds (BeO)	Bi (Bismuth)	
Lead and its compounds (PbF ₂)	Pt (Platinum), Hf (Hafnium), W (Tungsten), Fe	
Carbon and its compounds (Teflon, Graphite)	²³⁵ U (Uranium)	
S (Sulfur), Si (Silicon), Fe (Iron), Ar (Argon)		

4.4 Choice of the Materials to be used in the Beam Design

The choice of the appropriate material is directly related with the incoming neutron energy, and the nuclear characteristics (cross-sections), secondary particles produced after interaction, the gamma attenuation and photonuclear reaction of each individual element/isotope. Therefore, neutronic properties of the selected materials are discussed below.

4.4.1 Spectrum Shifter Materials

In the spectrum shifter method, moderation of the neutrons without significant absorption is the main requirement. A good spectrum shifter material should have large scattering cross-section and low absorption cross-section at the energies higher than about 0.4 eV. Specifically, the desired materials, if any, should have higher scattering cross-section in fast energy range and have lower scattering cross-section in epithermal and thermal energy ranges. Higher absorption cross-section in thermal energies is desirable to eliminate the thermal neutron contribution of the beam without applying filtering method.

Good moderators such as light water, heavy water, and carbon have low atomic number. However, it is important to note that such materials with very low atomic number may result in moderating the fast neutrons to the energies lower than 0.4 eV after a few collisions and decreasing the desired intensity of the beam. Furthermore, a spectrum shifter material must show sufficient resistance to the radiation damage. It should not either break down easily under radiation or produce contamination problem. A short lived by-product isotope after the neutron activation or photo-neutron reaction is desired.

Scattering (green) and total (red) cross-sections of some of the selected proper isotopes are plotted in Fig. 4.1. Once the all the isotopes are carefully examined, the candidate isotopes tabulated in Table 4.3 are found suitable for spectrum shifting purpose.

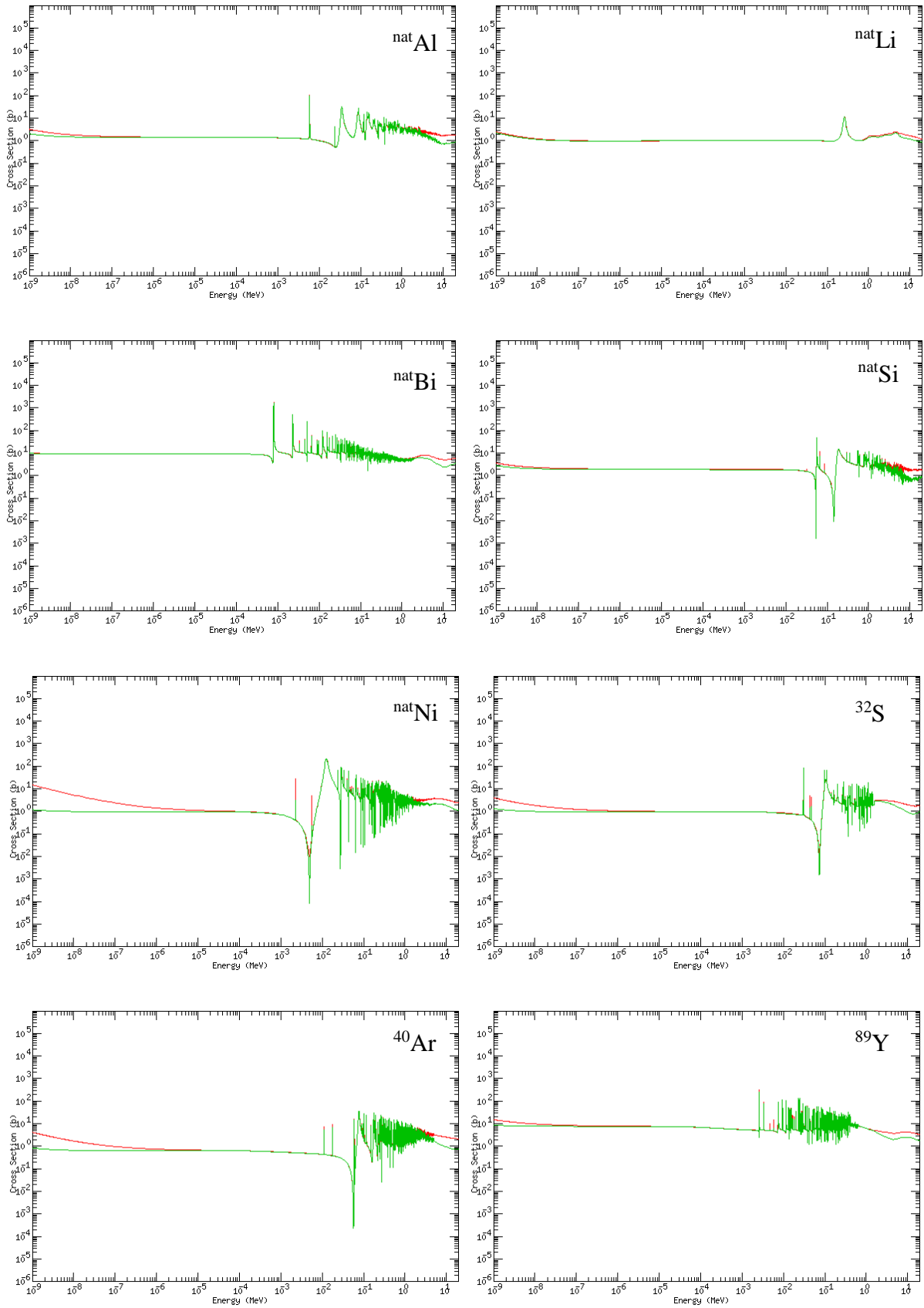


Fig. 4.1 Scattering (green) and total (red) cross-section of the some selected isotopes. [63]

As seen in the figure, the common property of these isotopes is to have very low absorption cross-section in epithermal and higher absorption cross-section in thermal and fast energies. Also, these isotopes have relatively lower cross-sections at the epithermal energy than the other materials that are not found proper. In addition, major resonance peaks of the selected isotopes are in the fast energy region.

In the beam shaping, material selection has great importance due to the secondary particle(s) released after the neutron capture reaction and/or photonuclear reaction. Table 4.3 shows possible decay type(s) of the daughter isotope for each isotope in the natural element and if any, the released particles after the decay. The same table contains the minimum activation photon energy for the photo-neutron reaction. Decay of the daughter isotope from the isomeric state is represented with asterisk. Probability of the different decay types are demonstrated in units of the percent value within the brackets. The rightmost column exhibits the maximum energy of the particles emitted with the significant intensity.

Table 4.3 Suitable spectrum shifter isotopes and decay schemes following neutron absorption [63]

Material	Neutron Capture	Daughter Half-life	Released Particle(s) Max. Energy (MeV)	Photoneutron Threshold Energy (MeV)
⁸⁹ Y (Yttrium)	⁸⁹ Y (n, β) ⁹⁰ Zr	64 h	2.28 β, 1.29 γ, 2.32 γ	
	⁸⁹ Y* (n, γ) ⁹⁰ Y	3.19 h	0.68 γ	
³² S	³² S (n, γ) ³³ S	Stable	-	15.04
⁴⁰ Ar	⁴⁰ Ar (n, β) ⁴¹ K	109 m	2.49 β, 1.29 γ	9.87
^{nat} Kr (Krypton)	⁸⁰ Kr (n, EC) ⁸¹ Br	2.29e5 y		
	⁸⁰ Kr* (n, γ) ⁸¹ Kr	13.10 s	0.190 γ	
	⁸² Kr (n, γ) ⁸³ K	Stable		
	⁸³ Kr (n, β) ⁸⁴ K	Stable		
	⁸⁴ Kr (n, β) ⁸⁵ Rb	3934.4 d	0.68 β, 0.514 γ	
	⁸⁴ Kr* (n, β) ⁸⁵ Rb (78 %)	4.480 h	0.84 β, 0.151 γ	
	⁸⁴ Kr* (n, γ) ⁸⁵ K (78 %)	4.480 h	0.31 γ	
³⁹ K (Potassium)	³⁹ K (n, β) ⁴⁰ Ca (89 %)	1.277e9 y	1.31 β, 1.46 γ	13.09
	³⁹ K* (n, EC) ⁴⁰ Ar (11 %)			
^{nat} Li	⁶ Li (n, α) ³ H	Stable	2.05 α	
	⁷ Li (n, β) ⁸ Be	838 ms	12.96 β	
^{nat} Si	²⁸ Si (n, γ) ²⁹ Si	Stable		17.18
	²⁹ Si (n, γ) ³⁰ Si	Stable		8.47
	³⁰ Si (n, β) ³¹ P	157.3 m	1.49 β, 1.27 γ	10.61
^{nat} Bi	²⁰⁹ Bi (n, β) ²¹⁰ Po	5.013 d	1.16 β	7.46
	²⁰⁹ Bi* (n, α) ²⁰⁶ Tl	3.04e6 y	4.69 α, 0.30 γ, 0.27 γ	
^{nat} Al	²⁷ Al (n, β) ²⁸ Si	2.24 m	2.86 β, 1.78 γ	13.06
^{nat} Ni	⁵⁸ Ni (n, EC) ⁵⁹ Co			12.22
	⁶⁰ Ni (n, γ) ⁶¹ Ni	Stable		11.39
	⁶¹ Ni (n, γ) ⁶² Ni	Stable		7.82
	⁶² Ni (n, β) ⁶³ Cu	100.1 y	0.07 β	10.60
	⁶⁴ Ni (n, β) ⁶⁵ Cu	2.5172 h	2.14 β, 1.62 γ	9.66
^{nat} Cu (Copper)	⁶³ Cu (n, EC) ⁶⁴ Ni (61 %)	12.700 h	1.67 β, 1.35 γ	10.85
	⁶³ Cu (n, β) ⁶⁴ Zn (39 %)	12.700 h	0.58 β	
	⁶⁵ Cu (n, β) ⁶⁶ Zn	5.120 m	2.63 β, 1.04 γ	9.91
^{nat} Pb	²⁰⁴ Pb (n, EC) ²⁰⁵ Tl	1.53e7 y		
	²⁰⁴ Pb* (n, EC) ²⁰⁵ Pb	5.54 ms	1.01 γ	
	²⁰⁶ Pb (n, γ) ²⁰⁷ Pb	Stable		8.09
	²⁰⁶ Pb* (n, γ) ²⁰⁷ Pb	0.806 s	1.06 γ	
	²⁰⁷ Pb (n, γ) ²⁰⁸ Pb	Stable		6.74
²⁰⁸ Pb (n, β) ²⁰⁹ Bi	3.253 h	0.64 γ	7.37	

The table indicates that the secondary photon particles emitted in the decay do not cause problems in shielding prompt gammas and reducing their intensity at port exit since the maximum energy of these can reach as high as 10 MeV. However, it is evident that photon (gamma and x-ray) contamination of the beam significantly increases. Maximum energy of the emitted photons is 2.32 MeV after the decay of ^{90}Y . Yet, the long and medium-lived isotopes (e.g., ^{90}Y , ^{210}Bi , ^{84}Kr) may result in contamination problem in handling/transporting the materials after the treatment. Photo-neutron interaction would result in somewhat neutron production inside the materials, Pb, ^{61}Ni , Bi and ^{29}Si .

It is understood during the examination that there are not many isotopes which meet the requirements. In the computational analyses, most of the elements are preferred in natural form (due to fabrication consideration). However, some of the assessed elements (e.g., Al and Pb) are used in the compound form with O or F isotopes to fill the valley between the resonance peaks. Typical moderators such as light water, heavy water, and carbon are not, on purpose, used since those materials have low scattering cross-section in fast energy range and have high scattering cross-section in epithermal energy, as shown in Fig. 4.2.

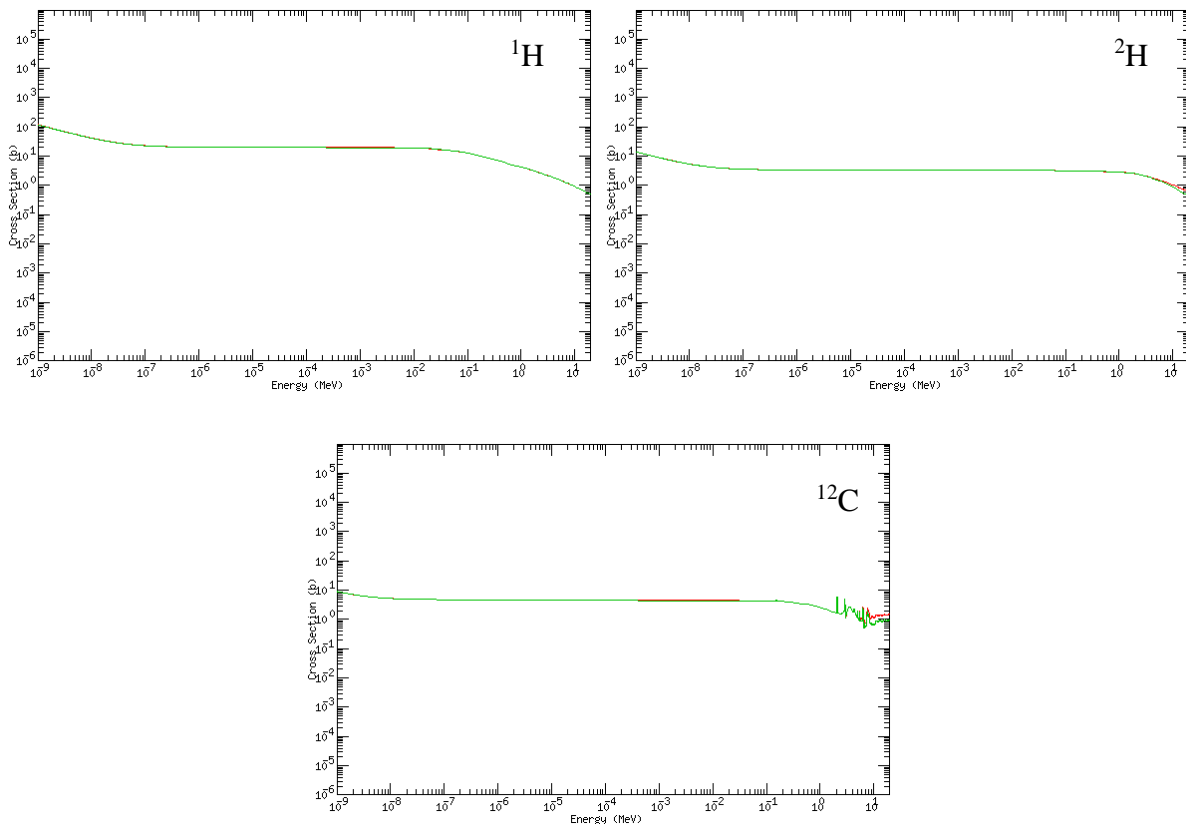


Fig. 4.2 Scattering (green) and total (red) cross-section of some commonly used moderator materials. [63]

4.4.2 Filtering Materials

In the filtering method, absorption of thermal neutrons¹⁰ of the incident beam is the main challenge. A good filtering material/isotope should have large absorption cross-section and low scattering cross-section at the thermal and fast energy ranges. Hence, all but the neutrons with energies of 0.4 eV to 10 keV should be filtered. Specifically, the desired materials, if any, should be relatively transparent to the epithermal neutrons. A high atomic mass is desirable to result in little energy loss when the neutrons are scattered. To prevent the self-shielding problem, material thickness should be as thin as possible. The $1/v$ cross section materials such as ^6Li or ^{10}B can be good candidates to wipe out the lower energy part of the thermal neutron spectrum of the beam.

As in the spectrum shifter materials, the filtering isotopes must show sufficient resistance to the radiation damage. It should not either break down easily under the radiation or produce contamination problem. A short lived by-product isotope after the neutron activation or photo-neutron reaction is desired.

Scattering (green) and total (red) cross-sections of some of the selected proper isotopes are plotted in Fig. 4.3. Once the all the isotopes are carefully examined, the candidate isotopes tabulated in Table 4.3 Table 4.4 are found suitable for filtering purpose.

¹⁰ Thermal neutrons in the beam are the neutrons that leak to beam port from reactor core and also neutrons that are slowed down when epithermal neutron flux in the incident beam is maximized using spectrum shifter materials.

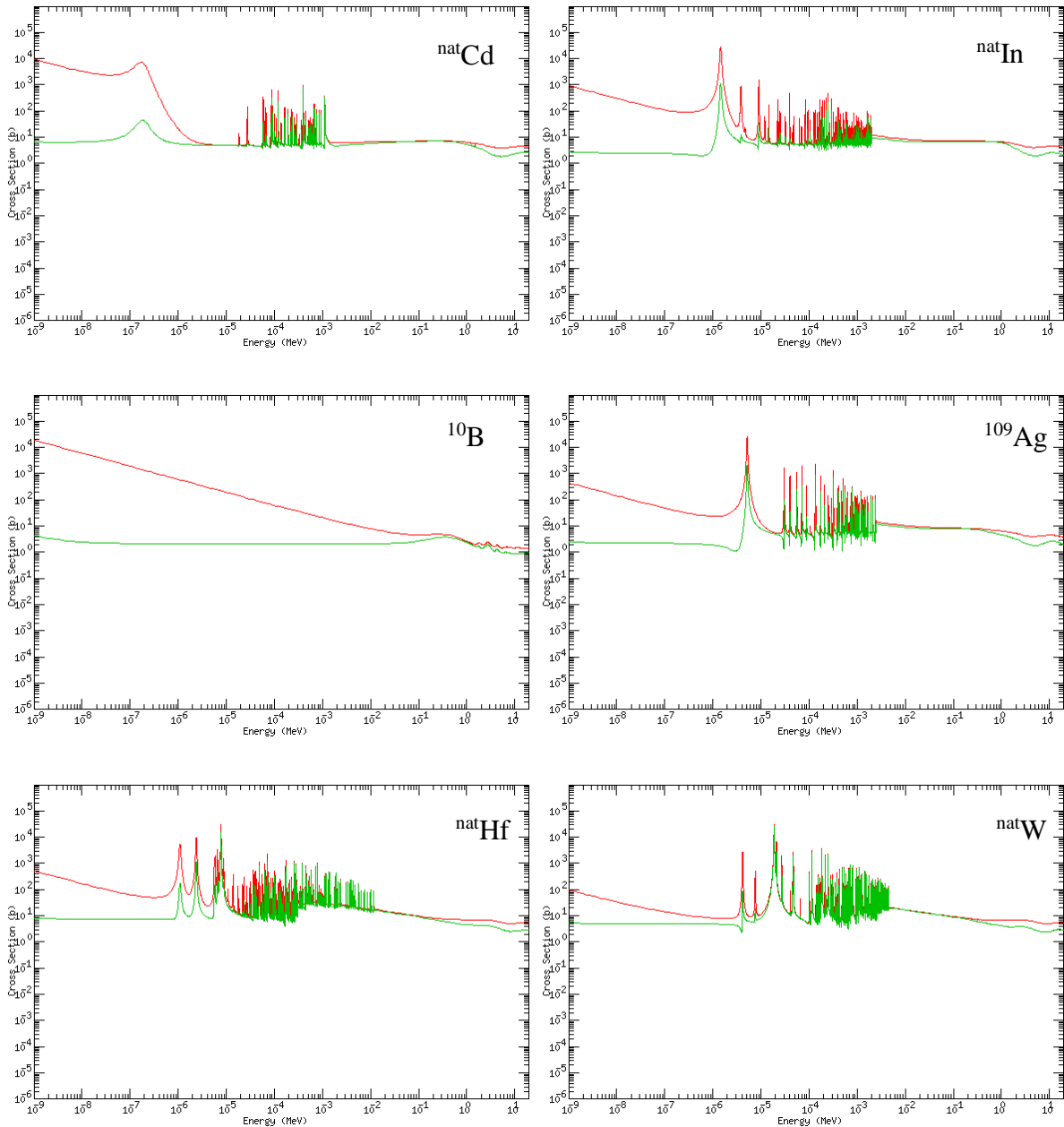


Fig. 4.3 Scattering (green) and total (red) cross-section of the some selected isotopes. [63]

As seen in the figure, the selected isotopes have very high absorption cross-section at thermal energy. Unfortunately, resonance peaks of those isotopes lie through the epithermal energy. However, they have very small mean free paths at the thermal region. Hence, the issue of absorption of neutrons in epithermal energy region may be solved if the filtering materials are prepared quite thick.

Table 4.4 shows possible decay type(s) of the daughter isotope for each isotope in the natural element and if any, the released particles after the decay. Description of the table is the same as Table 4.3.

Table 4.4 Suitable filtering isotopes and decay schemes following thermal neutron absorption [63]

Material	Neutron Capture	Daughter Half-life	Released Particle(s) Max. Energy (MeV)	Photon neutron Threshold energy (MeV)
^{nat} Cd	¹⁰⁶ Cd (n, EC) ¹⁰⁷ Ag	6.50 h	0.829 γ	10.87
	¹⁰⁸ Cd (n, EC) ¹⁰⁹ Ag	462.6 d	0.088 γ	10.33
	¹¹⁰ Cd (n, γ) ¹¹¹ Cd	Stable	0.25 γ	9.92
	¹¹¹ Cd (n, γ) ¹¹² Cd	Stable		6.97
	¹¹² Cd (n, β) ¹¹³ In	7.7e15 y	0.58 β	9.40
	¹¹³ Cd (n, γ) ¹¹⁴ Cd	Stable	9.0 γ	6.54
	¹¹⁴ Cd (n, β) ¹¹⁵ In	53.46 h	1.11 β , 0.53 γ	9.04
	¹¹⁴ Cd* (n, β) ¹¹⁵ In	44.6 d	1.62 β , 1.29 γ	
	¹¹⁶ Cd (n, β) ¹¹⁷ In	2.49 h	2.22 β , 1.58 γ	8.70
^{nat} In (Indium)	¹¹³ In (n, β) ¹¹⁴ Sn (99.50%)	71.9 s	1.98 β , 1.30 γ	
	¹¹⁵ In (n, β) ¹¹⁶ Sn (99.97%)	14.1 s	3.29 β , 1.29 γ	
	¹¹⁵ In* (n, β) ¹¹⁶ Sn	54.29 m	1.01 β , 2.11 γ	
^{nat} Ag (Silver)	¹⁰⁷ Ag (n, β) ¹⁰⁸ Cd (97.2%)	2.37 m	1.65 β , 0.633 γ	9.54
	¹⁰⁷ Ag (n, EC) ¹⁰⁸ Pd (2.8%)	2.37 m	0.896 p, 0.618 γ	
	¹⁰⁹ Ag (n, β) ¹¹⁰ Cd (99.7%)	24.6 s	2.89 β , 0.657 γ	7.27
	¹⁰⁹ Ag* (n, β) ¹¹⁰ Cd	249.79 d	1.51 β , 1.505 γ	9.19
^{nat} Hf	¹⁷⁴ Hf (n, EC) ¹⁷⁵ Lu	70 d	0.433 γ	
	¹⁷⁶ Hf (n, γ) ¹⁷⁷ Hf	Stable		
	¹⁷⁷ Hf (n, γ) ¹⁷⁸ Hf	Stable		
	¹⁷⁸ Hf (n, γ) ¹⁷⁹ Hf	Stable		
	¹⁷⁹ Hf (n, γ) ¹⁸⁰ Hf	Stable		
	¹⁸⁰ Hf (n, β) ¹⁸¹ Ta	42.39 d	0.405 β , 0.482 γ	
^{nat} B (Boron)	¹⁰ B (n, α) ⁷ Li	Stable	1.48 α	8.4
	¹¹ B (n, β) ¹² C (98.4%)	20.20 ms	13.37 β , 4.438 γ	7.2
	¹¹ B (n, $\beta+3\alpha$) ¹² C (1.6%)	20.20 ms		
²³² Th (Thorium)	²³² Th (n, β) ²³³ Pa	22.3 min	1.24 β , 0.670 γ	6.44
^{nat} W	¹⁸⁰ W (n, EC) ¹⁸¹ Ta	121.2 d	0.006 γ	8.41
	¹⁸² W (n, γ) ¹⁸³ W	>1.1e17 y		8.07
	¹⁸³ W (n, α) ¹⁸⁰ Hf	>3e17 y	1.48 α	6.19
	¹⁸⁴ W (n, β) ¹⁸⁵ Re	75.1 d	0.433 β , 0.125 γ	7.41
	¹⁸⁶ W (n, β) ¹⁸⁷ Re	23.72 h	1.31 β , 0.773 γ	7.19
^{nat} Ti	⁴⁶ Ti (n, γ) ⁴⁷ Ti	Stable		13.19
	⁴⁷ Ti (n, γ) ⁴⁸ Ti	Stable		8.88
	⁴⁸ Ti (n, γ) ⁴⁹ Ti	Stable		11.63
	⁴⁹ Ti (n, γ) ⁵⁰ Ti	Stable		8.14
	⁵⁰ Ti (n, β) ⁵¹ V	5.76 m	2.15 β , 0.929 γ	10.94
^{nat} Au (Gold)	¹⁹⁷ Au (n, β) ¹⁹⁸ Hg	2.7 d	0.96 β , 0.411 γ	8.07
	¹⁹⁷ Au* (n, γ) ¹⁹⁸ Au	2.27 d	0.333 γ	
^{nat} Gd (Gadolinium)	¹⁵² Gd (n, EC) ¹⁵³ Eu	240.4 d	0.103 γ	
	¹⁵⁴ Gd (n, γ) ¹⁵⁵ Gd	Stable		
	¹⁵⁵ Gd (n, γ) ¹⁵⁶ Gd	Stable		
	¹⁵⁶ Gd (n, γ) ¹⁵⁷ Gd	Stable		
	¹⁵⁷ Gd (n, γ) ¹⁵⁸ Gd	Stable		
	¹⁵⁸ Gd (n, β) ¹⁵⁹ Tb	18.479 h	0.96 β , 0.363 γ	
	¹⁶⁰ Gd (n, β) ¹⁶¹ Tb	3.66 m	1.64 β , 0.361 γ	

A contamination problem, as in the case of spectrum shifter, may emerge due to the long and medium-lived isotopes (e.g., ^{109}Cd , $^{110\text{m}}\text{Ag}$ and ^{133}Gd). A considerable contribution to photon contamination appears to be originated from the neutron capture of ^{113}Cd producing a 9 MeV photon and from the decay of ^{12}B isotope emitting a 13.37 MeV beta-minus particle with a 4.4 MeV photon. Shielding of these gammas requires special attention. Furthermore, photons less than 10 MeV would lead to neutron production inside all the filtering materials, in particular, ^{133}W , ^{113}Cd and ^{232}Th .

It is understood during the examination that not many isotopes meet the requirement of high thermal/fast neutron absorption cross-section. However, all the isotopes have high scattering cross-section in the resonance part. In the computational analyses, all the isotopes are preferred in natural form except that boron element is used in the form of B_4C . It is observed that high filtering ratio can be easily achievable if the materials are formed with a single (as pure) isotope.

4.4.3 Collimator Materials

In the collimator design, the materials which show a high reflecting property with high scattering cross section and high atomic mass (resulting in little energy loss) such as Pb and Bi are used to turn the neutrons back into the beam and to increase the beam intensity. Geometric shape, dimensions and the material(s) used in fabrication are the design challenges to overcome. To date, there are two types of collimators used in the research studies. These are the divergent and convergent beam collimators. The type and design parameters depend on which application is taken into account at the collimator exit.

Convergent collimators are widely used in neutron radiography with the lining materials in the inner wall of collimator such as boron, cadmium, dysprosium, europium, gadolinium and indium [64]. In addition, a complicated design of collimators which have varying inner radius and materials is used in the examined studies [61]. For instance, polyethylene collimator mixed with B_4C or Li_2CO_3 is used.

A candidate material should not thermalize the epithermal neutrons significantly and produce high energetic gamma rays after a radiative capture process. But, in the meantime, thermal neutrons striking to the wall of the collimators need to be absorbed to reduce the thermal neutron dose contribution.

The selected appropriate collimator materials without a lining material in accordance with the requirements are listed in Table 4.5.

Table 4.5 Suitable collimator materials and decay schemes following neutron absorption [63]

Material	Neutron Capture	Daughter Half-life	Released Particle(s) Max. Energy (MeV)	Photoneutron Threshold Energy (MeV)
Cerrobend (30 % Bi + 31.8 % Pb + 18.2 % Sn)	$^{112}\text{Sn} (n, \text{EC}) ^{113}\text{In}$	115.09 d	0.392 γ	10.79
	$^{114}\text{Sn} (n, \gamma) ^{115}\text{Sn}$	Stable		10.30
	$^{115}\text{Sn} (n, \gamma) ^{116}\text{Sn}$	Stable		7.55
	$^{116}\text{Sn} (n, \gamma) ^{117}\text{Sn}$	Stable		9.56
	$^{117}\text{Sn} (n, \gamma) ^{118}\text{Sn}$	Stable		6.94
	$^{118}\text{Sn} (n, \gamma) ^{119}\text{Sn}$	Stable		9.33
	$^{119}\text{Sn} (n, \gamma) ^{120}\text{Sn}$	Stable		6.49
	$^{120}\text{Sn} (n, \beta) ^{121}\text{Sb}$	27.06 h	0.389 β	9.11
	$^{122}\text{Sn} (n, \beta) ^{123}\text{Sb}$	129.2 d	1.40 β , 1.09 γ	8.81
	$^{124}\text{Sn} (n, \beta) ^{125}\text{Sb}$	9.64 h	2.06 β , 0.311 γ	8.49
PE (Polyethylene)	$^{12}\text{C} (n, \gamma) ^{13}\text{C}$	Stable		18.72
	$^{13}\text{C} (n, \beta) ^{14}\text{N}$	5730 y	0.16 β	4.95
	$^1\text{H} (n, \gamma) ^2\text{H}$			
	$^2\text{H} (n, \beta) ^3\text{He}$	12.33 y	0.019 β	2.22
$^{\text{nat}}\text{Be}$	$^9\text{Be} (n, \beta) ^{10}\text{Be}$	1.51e6 y	0.556 β	1.67
CaF ₂ (Calcium Fluoride)	$^{40}\text{Ca} (n, \text{EC}) ^{41}\text{K}$	1.03e5 y		15.64
	$^{42}\text{Ca} (n, \gamma) ^{43}\text{Ca}$	Stable		11.48
	$^{43}\text{Ca} (n, \gamma) ^{44}\text{Ca}$	Stable		7.93
	$^{44}\text{Ca} (n, \beta) ^{45}\text{Sc}$	162.61 d	0.258 β , 0.012 γ	11.13
	$^{19}\text{F} (n, \beta) ^{20}\text{Ne}$	11.163 s	5.39 β , 1.633 γ	
Fluental (30 % Al + 69 % AlF ₃ + 1 % LiF)	See Table 4.2 and Table 4.3 for the reactions of listed isotopes.			

It is important to mention that Cerrobend material is composed of 30 % Bi, 31.8 % Pb and 18.2 % Sn (Tin). The chemical formula of polyethylene (PE) is $(\text{C}_2\text{H}_4)_n \text{H}_2$. Fluental contains 30 % Al, 69 % AlF₃ and 1 % LiF.

In the collimator design, radiation resistant materials are preferred since the collimator is the last step in designing the beam and the last layer in protecting the patient from the contaminations. As seen in the table, photo-neutron production of beryllium and deuterium seems serious. Luckily, they almost do not absorb the neutrons. Among the isotopes, the most important contamination is due to the hard gamma-ray emission of Al with 1.78 MeV following the thermal neutron absorption.

4.4.4 Gamma Shielding

For the BNCT, a good gamma shielding material should reduce the photon fluence as low as possible but, at the same time it should be transparent to the epithermal neutrons. Therefore,

materials such as Pb and Bi, which are relatively transparent to neutrons, can be used in the BP to reduce photons. Change of mass attenuation coefficients of Pb and Bi with the incident photon energy is illustrated in Fig. 4.4.

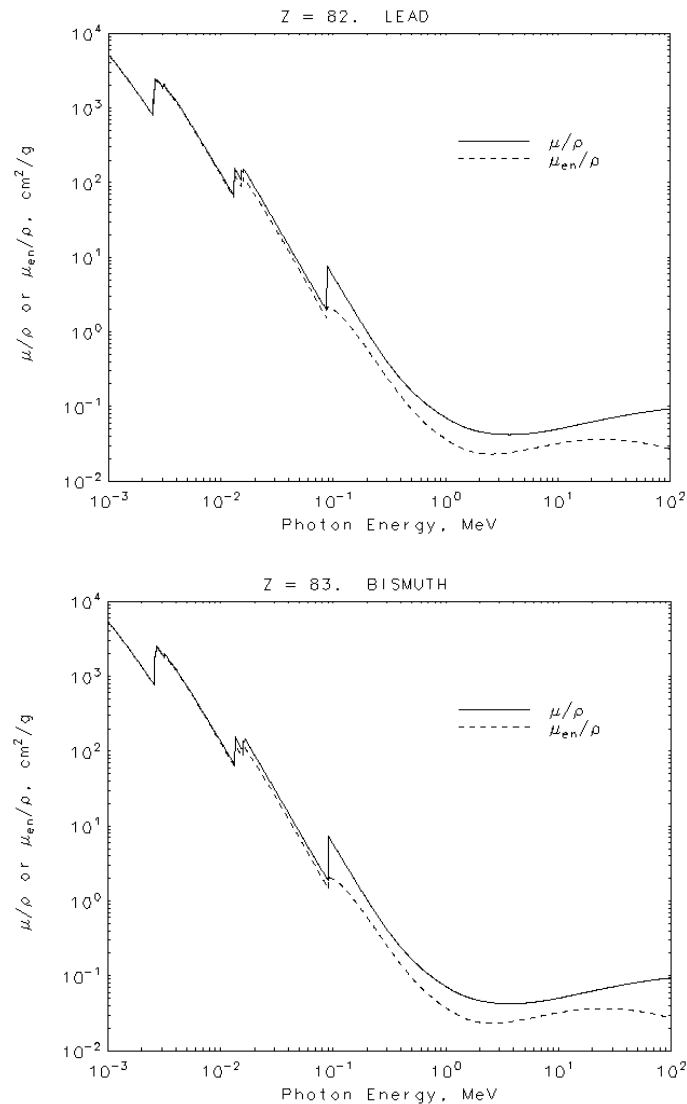


Fig. 4.4 Mass attenuation coefficient of Pb and Bi [65]

Shielding of the photons must be performed by taking the most energetic photon, up-to 10 MeV prompt gammas, into account. As seen in the figures, mass attenuation coefficients of both materials in the energy range of 1 and 10 MeV are almost constant with a value of about 0.05 cm²/g.

These materials, nonetheless, would result in somewhat reduction in the neutron beam intensity due to interaction with neutrons; but, photo-neutron interaction would result in somewhat neutron production inside the materials. Here, the main problem with Bi is to transmute to highly toxic ²¹⁰Po following the neutron absorption. Thus, Pb is used in shielding the photons.

5. IMPLEMENTATION OF GENETIC ALGORITHM

5.1 Fundamentals of the GA

In an optimization problem, the best solution, defined as the global optimum, is searched among the number of possible solutions, called search space, and among the local optimums. The issue with the optimization in classical methods like mathematical iterations is the initiation of the searching process from a single point within enormous size of the search space. In contrast to mathematical methods, GA uses a distinct method that produces the random spread solutions throughout the search space.

Each different solution in the GA is defined by a distinct chromosome. A chromosome contains a number of genes each of which corresponds to a variable used to obtain the solution. The genes (or variables) can be continuous or discrete. A chromosome can be encoded in the algorithm by means of binary format as well as real values (real-coded). In the GA, while the iteration steps are named as the generations, all the solutions in a generation are termed as the population. Furthermore, the code demonstration of the solution is characterized by the genotype like A, T, G in DNA structure whereas appearance of the solution in real life (i.e., hair color) as a result of genotype is characterized by the phenotype.

As a numerical optimization method, the GA uses natural evolution processes (operators) to solve a wide range of complex engineering problems. To lead the solutions toward the global optimum, typical GA uses selection, crossover and mutation operators. Selection operator, very similar to natural selection rule, applies a selection criterion for the individuals to pick better solutions or eliminate worse solutions. Crossover operator is used to swap the genetic information (gene(s)) between the elite solutions to get a better evolved offspring. The main role of the mutation operator is to change randomly the value of a gene inside the chromosome and to obtain more diverse solutions.

After the operators are applied, a number of offspring (a new population) are produced from the current population. This process repeats until a pre-defined number of generations are elapsed or one of the defined convergence criterion is met.

There are two types of GA applications. First is the Single-Objective GA (shortly SOGA) developed to solve the problems comprising single objective. Second is the Multi-Objective GA (MOGA) utilized for the problems having two or more than two objectives.

Although the GA is an effective method, there is no guarantee for it to solve every optimization problem.

5.2 Use of the GA Method in Beam Shaping

In this study, the GA method is used to search the patterns appropriate for the considered nuclear application. The design process follows the estimation of application-dependent bounds (or constraints) such as minimum epithermal flux required for the irradiation of the cancerous cells. Such pattern search problems contain at least two objectives to be achieved. For this purpose, NSGA-II [66] with the Binary Tournament is selected for the optimization. In order to search the best patterns suitable for BNCT, a GA code is prepared. The code is linked with MCNP to calculate the neutron/photon fluxes at the port exit (at the patient side). It incorporates strategies of multi-objective Pareto-optimal GA and MC method.

A real-coded GA with discrete/continuous variables is used in this study since this technique is easy to use and does not require coding/decoding of the chromosomes. A continuous GA flowchart given in Fig. 5.1 shows the computational main steps performed. The terms used in the GA are as follows: cost function means the generated pattern which the MCNP uses to calculate the objectives; discrete variables refer to types of materials given in the pattern while continuous variables refer to length and inner/outer radius of the collimator material; objectives to be achieved are the Φ_{th} , Φ_{epi} , Φ_f , I_γ and J_{epi}/Φ_{epi} values of the generated pattern. The used GA method and the genetic operators are described below in detail.

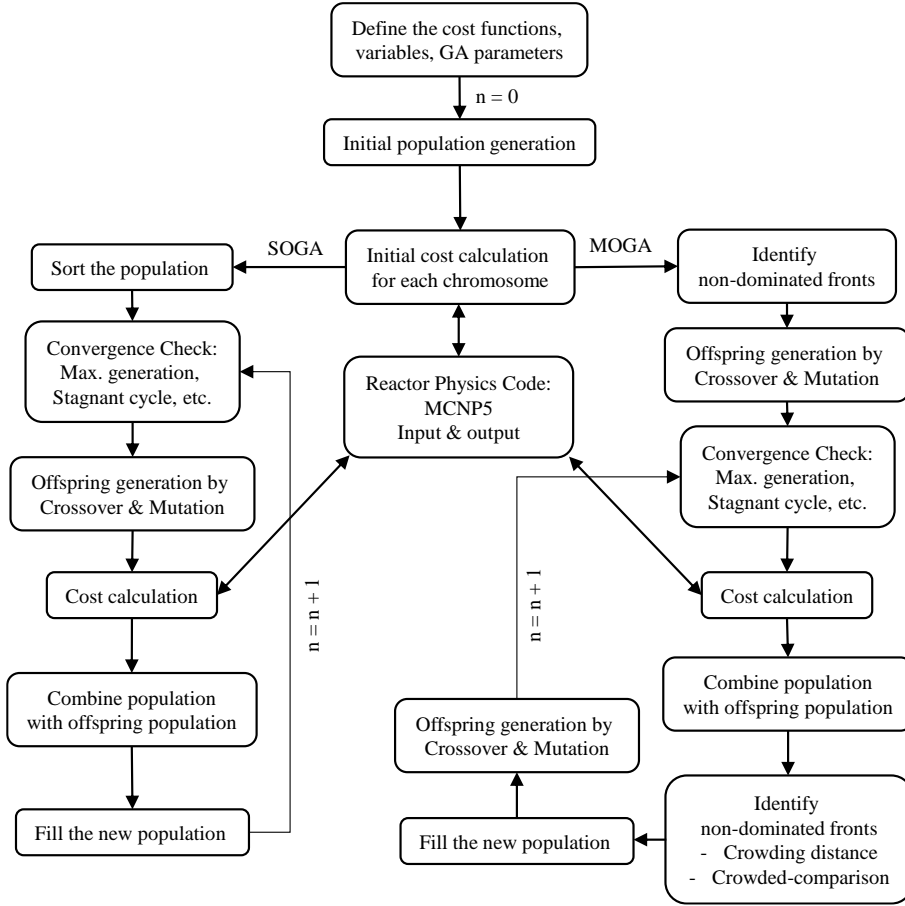


Fig. 5.1 GA flowchart for SOGA and MOGA (NSGA-II) methods

5.3 MOGA: NSGA-II Method

In this study, the following optimization problem is considered:

$$y = [f_1(x_1, \dots, x_n), \dots, f_m(x_1, \dots, x_n)] \text{ subject to } x_n \in S \quad (\text{Eq. 5.1})$$

where y is the objective vector, f is the cost function to be minimized (or maximized or any), m is the number of objective functions to be evaluated, x_n is the number of variables (may be dependent or independent) to be optimized, and S is the multi-dimensional search space with the defined upper/lower boundary limits.

Optimization problems given in Eq. 5.1 always have more than one objective to be optimized. Therefore, they require an advanced sorting method which is quite different from the method that SOGA uses. In a multi-objective optimization problem, a feasible solution for which all of the objectives are optimized simultaneously may not exist. In such cases, there is more than one feasible solution, these solutions are called Pareto-optimal solutions.

In this study, the selected multi-objective GA method used to find possible patterns is the Non-Dominated Sorting GA (NSGA-II) method purposed by Deb et al. [66]. It is a single parameter

(only population size), well-tested and efficient multi-objective GA. In the algorithm, fitness assignment is based on the Fast Non-Dominated Sorting Method without an external population. Diversity is preserved by using the Crowding Distance Mechanism. The Crowding Distance provides worthwhile benefits to users by computing the population density close to the best solutions. Also, it provides a uniform spread of solutions along the best-known Pareto front without using a fitness sharing value. The selection is carried out by using the Crowded-Comparison operator. NSGA-II algorithm is briefly defined in the following main steps:

- For the generation $i = 0$, create a random initial population (P_0) with a population size of N .
- Calculate cost functions for each member of the population.
- Identify the non-dominated fronts ($F_1, F_2\dots$) using the Fast Non-Dominated Sorting method.
- Create an offspring population (O_0) with a population size of N by the Crossover and Mutation operators. Use the Binary Tournament Selection method to select the parents from the population.
- Check the results for the predefined stopping criteria. If the results are converged, then stop and provide the Pareto-front solutions. If not, then go on searching.
- Calculate cost functions for each member of the offspring population.
- For $i \geq 1$, combine the population ($C_i = P_i \cup O_i$) with the generated offspring population. Now, the combined population size is $2N$.
- Identify the non-dominated fronts ($F_1, F_2\dots$) of C_i using the Fast Non-Dominated Sorting method.
 - Calculate crowding distance value of each solution in each front using the Crowding Distance method.
 - Fill the new population (P_{i+1}) from the subsequent non-dominated fronts with respect to their rank (from the best solutions of F_1 in the C_i) until the new population is filled.
 - If the size of the last non-dominated front F_n causes exceeding the size of the new population, select the best solutions by sorting the solution of the last front according to the Crowded-Comparison operator in descending order and then fill the population with the least-crowded solutions until no more position remains.

- Create an offspring population with a population size of N by the Crossover and Mutation operators. Use the Binary Tournament Selection method by selecting the parents from the population based on the Crowded-Comparison operator.
- Increase the generation by one ($i = i + 1$) and go to convergence check step.

5.3.1 Details of Fast Non-Dominated Sorting method

According to the method, the population is sorted according to non-domination sets. For any solution of p and q in the main population (P), the algorithm follows below steps:

- Set $S_p = \emptyset$. If p dominates q , then insert solution q into $S_p = S_p \cup \{q\}$ where S_p is the solution set which contains all the individuals dominated by p .
- Set $n_p = 0$. If q dominates p , then increase the n_p by one ($n_p = n_p + 1$) where n_p is the number of solutions which dominate p .
- When no solution (if n_p equals to zero) dominates p , the solution p belongs to first front F_1 , $F_1 = F_1 \cup \{p\}$.
- Set the front counter to one ($i = 1$). While the front F_i is not empty $F_i \neq \emptyset$, set $Q = \emptyset$ where Q is used to store the solutions for the next front F_{i+1} .
- For each solution p in the front F_i , and each solution q in the set S_p , follow the below rule;
 - Visit each member q in the set S_p and decrease n_q by one, $n_q = n_q - 1$.
 - When n_q becomes zero ($n_q = 0$), put the solution q in a separate list Q , $Q = Q \cup \{q\}$.
 - Increase the front counter by one ($i = i + 1$) to find the members of the next fronts.
 - Now, identify the members of the current front F_i by setting $F_i = Q$.

5.3.2 Details of Crowding Distance

After the non-dominated sorting step is completed, the density calculation of the solutions around a particular solution needs to be carried out. This is because the selection process is performed over the rank and crowding distance values of the individuals. The Crowding Distance stands on the idea calculating the Euclidian distance between each solution in a front

according to m objectives. For each front F_i containing the number of solutions $l = |F_i|$, the algorithm can be expressed as below:

- Define the crowding-distance set I as $I(i) = 0$ for each solution, i .
- For each objective m , sort the solutions of F_i in the ascending order. Assign each solution as $x_{(i,m)}$ in the sorted listed.
- Set the upper and lower boundary values as infinite distance, $I_m(x_{(1,m)}) = \infty$ and $I_m(x_{(l,m)}) = \infty$
- For $i = 2, \dots, l-1$, calculate $I_m(x_{(i,m)}) = I_m(x_{(i,m)}) + \frac{I_m(x_{(i+1,m)}) - I_m(x_{(i-1,m)})}{I_m^{\max} - I_m^{\min}}$.

5.3.3 Details of Crowded-Comparison Operator

After the fast non-dominated sorting method is applied and the crowding distance calculation is performed, Crowded-Comparison operator is used to select the elite individuals for the offspring creation by using the binary tournament selection technique. Crowded-Comparison operator (\prec) is defined as follows:

- Assume that each solution p in front F_i has its non-domination rank (p_{rank}) and crowding distance value ($x_{distance}$)
- Prefer the solution with the lower (better) rank if two solutions have different non-domination ranks. If the selected solutions are located at the same front then, the solution that is located in a lesser crowded region is
 - If ($p_{rank} < q_{rank}$) then ($p \prec_n q$)
 - Or if ($p_{rank} = q_{rank}$) and ($x_{distance} > y_{distance}$) then ($p \prec_n q$).

5.4 Validation of the prepared GA code

The test problems are selected from a number of sample test problems used in the literature for validation of the code. The chosen problems, SCH [67], FON [68], KUR [69] and ZDT2 [70], have a wide variety of characteristics of the Pareto-Optimal front such as (non-)convexity and (dis)connectivity, and those are listed in Table 5.1. Throughout testing process, a real-coded (not binary) GA is used. In the implementation of NSGA-II, one-point cross-over and a mutation probability of $1/n$ (where n is the number of decision variables) are used.

Table 5.1 Test problems used for validation

Prob.	n	Variable Bounds	Objective Function	Optimal Solutions	Problem Types
SCH	1	$[-10^3, 10^3]$	$f_1(x) = x^2$ $f_2(x) = (x-2)^2$	$x \in [0, 2]$	Convex Connected
FON	3	$[-4, 4]$	$f_1(x) = 1 - \exp\left(-\sum_{i=1}^n \left(x_i - \frac{1}{\sqrt{3}}\right)^2\right)$ $f_2(x) = 1 - \exp\left(-\sum_{i=1}^n \left(x_i + \frac{1}{\sqrt{3}}\right)^2\right)$	$x_1 = x_2 = x_3$ $\in [-1/\sqrt{3}, 1/\sqrt{3}]$	Non-convex Connected
KUR	3	$[-5, 5]$	$f_1(x) = \sum_{i=1}^{n-1} \left(-10 \exp\left(-0.2\sqrt{x_i^2 + x_{i+1}^2}\right)\right)$ $f_2(x) = \sum_{i=1}^n \left(x_i ^{0.8} + 5 \sin(x_i^3)\right)$		Non-convex Disconnected
ZDT2	30	$[0, 1]$	$f_1(x) = x_1$ $f_2(x) = g(x) \left[1 - (f_1(x)/g(x))^2\right]$ $g(x) = 1 + 9 \left(\sum_{i=2}^n x_i\right) / (n-1)$	$x_1 \in [0, 1]$ $x_i = 0, i = 2, \dots, n$	Non-convex Connected

The results of NSGA-II method reported by Deb et al. [66] and the results of the prepared GA code in this study are compared and result of comparison is shown in Fig. 5.2. The convergence and distribution of solutions obtained in this study fully overlap with those of NSGA-II for test problems of SCH, FON, KUR and ZDT2. The results show that the prepared code yields adequately reliable results if a sufficient number of generations are used.

After the code validation is completed, it was decided that the code can be used for the optimization analyses in order to find the proper patterns for the PBP.

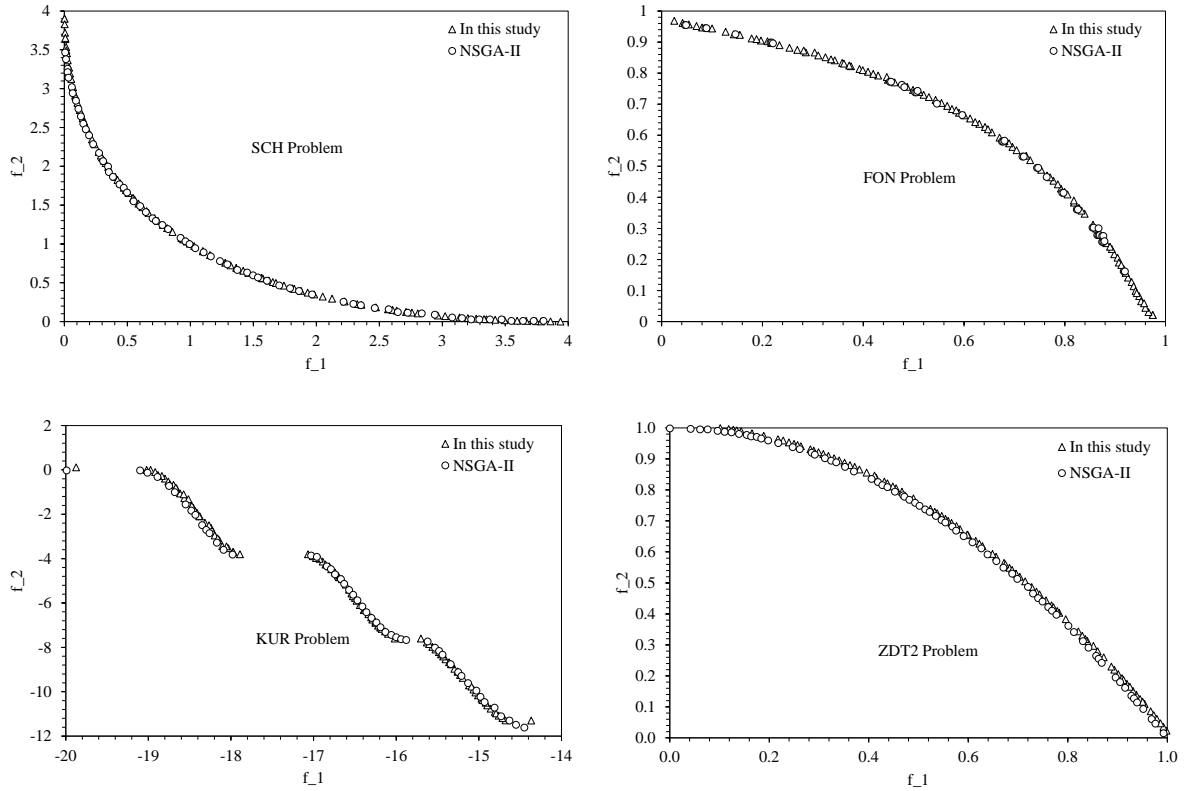


Fig. 5.2 Comparison of results of NSGA-II with results of this study for the test problems of SCH, FON, KUR and ZDT2.

5.5 Pattern Creation

A pattern is generated by using the methods mentioned in Section 4.3. The order of these methods inside the BP depends on the neutron spectrum of the incident beam. However, as a general rule, collimator is placed to the port exit as the last part. Furthermore, since the spectrum shifter sub-pattern causes a certain increase in the number of thermal neutrons due to slowing down of fast neutrons into thermal energy, placing the spectrum shifter before the filtering to eliminate the thermal neutron contribution of the beam seems reasonable. In this manner, sequence of the final pattern is in order as follows: the spectrum shifter, filtering and collimator sub-patterns.

In a sub-pattern, the thickness, type and location of a specific material to be used inside the sub-pattern are unknown variables, and also the total length of the sub-pattern is the other unknown parameter. In optimization, computational time increases considerably as the number of variables in the cost function increases. Therefore, the sub-patterns are discretized (changed to the discrete optimization problem from continuous) in the spectrum shifter and filtering optimization problems. Hereby, number of used variables in the cost function and hence,

computational time are decreased significantly. The unknown variables are limited to the search of material sequence.

Furthermore, total lengths of the sub-patterns are also fixed. Maximum total length is adjusted in such a way that epithermal neutron flux would not fall below 1×10^7 n cm⁻² s⁻¹ at the sub-pattern exit. After a few trials, for each sub-pattern, maximum sub-pattern length is obtained except for collimator. The collimator is a special case because the length of the collimator has no significant effect on the absorption of the neutrons. Instead, it changes orientation of the particles. Thus, maximum collimator length used in this study is open to change.

Only neutron transport calculation is considered throughout the optimization; photon transport is included once the optimization is completed.

The optimization steps of each sub-pattern are given below.

5.5.1 Spectrum Shifter

A spectrum shifter sub-pattern has a total length of 40 cm with 1 cm thick, including 40 regions, and it is generated using 17 different spectrum shifter materials (without air). Air is used to create an empty location inside the sub-pattern.

Based on the selection process described in Section 4.4.1, the materials used in the pattern creation are tabulated in Table 5.2. It should be noted that Ar and Kr materials are used in the liquid form with a density of 1.39 and 2.41 g cm⁻³, respectively. In the same table, mean free path (λ_{ave}) averaged over the all energies is presented for each material to determine the average thickness of each spectrum shifter material inside the pattern. The criterion is that the fast neutrons would interact with the material a few times but the other neutrons would not. Thus, by looking into the λ_{ave} , the values imply that average material thickness should be in the order of several centimeters. Sensitivity of the thickness is selected to be 1 cm regarding one-third of the smallest one (according to ^{nat}Cu).

Table 5.2 Spectrum shifter materials to be used in the pattern creation

	λ_{ave} (cm)		λ_{ave} (cm)		λ_{ave} (cm)		λ_{ave} (cm)
^{nat} Y (Yttrium)	4.38	^{nat} Ar (liq.) (Argon)	351	^{nat} K (Potassium)	50.26	^{nat} Si (Silicon)	10.99
^{nat} Al (Aluminum)	8.87	Al ₂ O ₃	2.93	^{nat} Ni (Nickel)	2.34	^{nat} Bi (Bismuth)	4.61
^{nat} S (Sulfur)	22.94	^{nat} Kr (liq.) (Krypton)	10.12	^{nat} Li (Lithium)	13.85	PbF ₂	3.00
SiC	3.44	^{nat} Cu (Copper)	2.59	^{nat} Pb (Lead)	4.10	Air	5110
AlF ₃	3.50	Al ₂ (SO ₄) ₃	4.33				

A sample pattern is given in Fig. 5.3. Objectives to be achieved are determined as the maximization of epithermal neutron flux and minimization of the fast neutron flux at the exit of the sub-pattern. Population used per generation is 140.



Fig. 5.3 A sample pattern generated using spectrum shifter materials

5.5.2 Filtering

A filtering sub-pattern has a total length of 9 cm with 0.3 cm thick, including 30 regions, and generated using 10 different filtering materials (without air). Air is used to create an empty location inside the sub-pattern.

Based on the selection process described in Section 4.4.2, the materials used in the pattern creation are tabulated in Table 5.3. In the same table, mean free path (λ_{ave}) averaged over the all energies and mean free path (λ_{th}) averaged over the thermal energy are presented for each material to determine the average thickness of each filtering material inside the pattern. The criterion is that the thermal neutrons would interact with the material at least once but the rest would not. Thus, by looking into the λ_{ave} and λ_{th} , the values imply that average material thickness should be on the order of several millimeters. Sensitivity of the thickness is selected to be 3 mm as an average value.

Table 5.3 Filtering materials used in the pattern creation

	$\lambda_{ave} / \lambda_{th}$ (cm)		$\lambda_{ave} / \lambda_{th}$ (cm)		$\lambda_{ave} / \lambda_{th}$ (cm)
^{nat} Cd (Cadmium)	1.78/8.54e-3	^{nat} In (Indium)	3.66/0.133	^{nat} Ag (Silver)	2.12/0.25
^{nat} W (Tungsten)	2.12/0.65	^{nat} Ti (Titanium)	4.87/1.80	^{nat} Au (Gold)	2.14/0.16
^{nat} Hf (Hafnium)	2.78/0.20	B ₄ C	2.21/9.52e-3	²³² Th (Thorium)	3.72/1.75
^{nat} Gd (Gadolinium)	4.21/6.74e-4	Air	5110/-		

A sample pattern is given in Fig. 5.4. Objectives in the design of the sub-pattern are the maximization of epithermal neutron flux and minimization of thermal neutron flux at the exit of the sub-pattern. Population used per generation is 100.

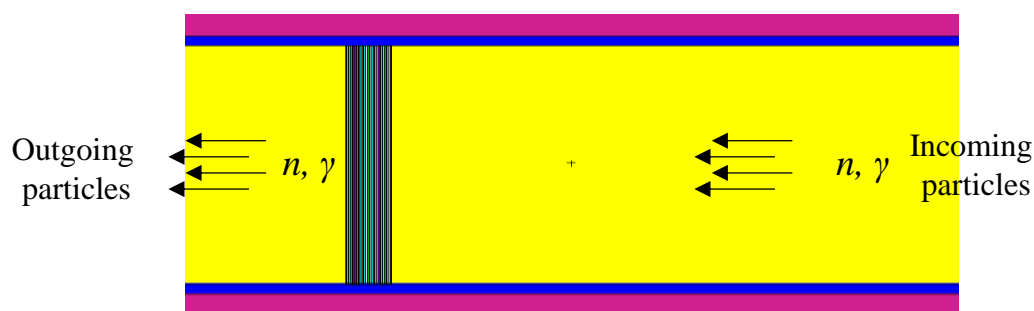


Fig. 5.4 A sample pattern generated using the filtering materials

5.5.3 Collimator

A collimator sub-pattern has a length of up-to-40 cm (L), an inner (r_i) and outer radius (r_o) of up-to-10 cm, including 1 region, and generated using 9 different collimator materials.

Based on the selection process described in Section 4.4.3, the materials used in the pattern creation are tabulated in Table 5.4.

Table 5.4 Collimator materials used in the pattern creation

Cerrobend	PE (Polyethylene)	^{nat} Bi	^{nat} Al	Al ₂ O ₃	^{nat} Be (Beryllium)	^{nat} Pb	CaF ₂ Fluental
-----------	----------------------	-------------------	-------------------	--------------------------------	----------------------------------	-------------------	---------------------------

A sample pattern is given in Fig. 5.5. Objectives to be achieved are determined to be the maximization of epithermal neutron flux and maximization of epithermal neutron current to epithermal flux ratio at the end of the sub-pattern (collimator). Population used per generation is 80.

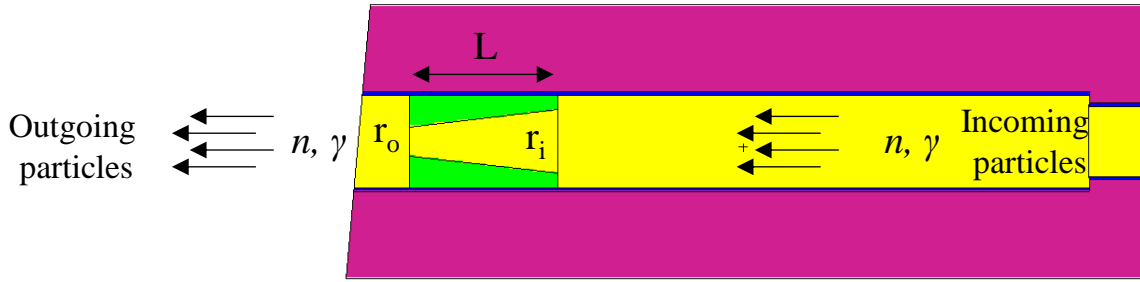


Fig. 5.5 A sample pattern generated by using the collimator materials

5.6 Description of the Chromosome Structure

Each different (sub)pattern is represented by a unique chromosome in the GA. A generated chromosome with a chromosome length of n is defined by a number of genes. Each gene of a chromosome refers to type of a material shown in Fig. 5.3 and Fig. 5.4 or length/radius given in Fig. 5.5. A chromosome contains a number of genes; same genes express the same material but different location in the pattern. Furthermore, each gene carries specific information about the materials (material density, isotopic content, atomic weights and cross-section identifiers for neutron/photon/photo-atomic reactions) required for the MC calculations. Genotype and phenotype of a produced sample chromosome are given in Fig. 5.6. As an illustration, the first gene with the number 2 represents the sulfur (S) while the last gene with the number 13 is Al_2O_3 . Chromosomes are randomly created from a total of 17 different spectrum shifter materials to optimize the epithermal/fast neutron flux, a total of 10 filtering materials to optimize epithermal/thermal neutron flux and a total of 9 collimator materials to optimize the epithermal neutron flux and neutron current to flux ratio. Air is also added into the used materials to define the “no material” in the pattern.

Genotype= [2	2	7	8	13	13	13]
Phenotype= [S	S	Si	Ar	Al_2O_3	Al_2O_3	Al_2O_3]

Fig. 5.6 Genotype and phenotype of a sample chromosome generated using spectrum shifter

5.7 Selection operator

Crowded-comparison operator of the NSGA-II is the primary selection operator. For this purpose, first, the current population, including produced offspring population (by mutation and crossover), is sorted in descending order according to the crowding distance values. Subsequently, the population is sorted in ascending order according to the rank values and non-domination sets. Finally, for a considered population size, a new population is obtained from the current population by choosing the best solutions.

5.8 Crossover operator

Heuristic crossover method is used in searching the collimator pattern which has the continuous genes. Otherwise, scattered crossover method [71] for the discrete genes is implemented. The elite parents are selected with Binary Tournament Selection.

5.9 Mutation operator

For an elite parent selected with Binary Tournament Selection, a one-point mutation [71] is used to create offspring. For this purpose, a randomly selected gene of the considered parent chromosome is randomly changed between the upper and lower bounds of any variable. One-point mutation has a mutation probability of $1/n$ where n is number of genes in a chromosome. It should be noted that although the desired/suggested mutation probability which would provide more diverse population is in the order of 0.01, in this study, the probability ranges from 0.025 (1/40) to 0.25 (1/4) depending on which sub-pattern type is selected. If the same materials are chosen for replacing, the mutation process is repeated until a different material is selected. Further, in order to avoid producing the same offspring, all the generated chromosomes are stored in the archive, and only different chromosomes are allowed to pass to the next generation.

5.10 Cost Calculation: Reactor physics code

For each generated pattern, at the tally regions, the cost functions are Φ_{th} , Φ_{epith} , Φ_{fast} and J_{epith} / Φ_{epith} for neutrons and I_γ for the photons.

Each chromosome created by the GA code is sent (as input) to a prepared script to get the cost values. The script converts chromosomes to the input decks of the selected physics code. Moreover, another generated script extracts the cost values from the code output.

The code seeks the proper patterns by simulating a number of patterns created by stochastic processes and uses MCNP in the background to calculate the neutron/photon fluxes at the (sub)pattern exit.

5.11 Convergence Criterion

The convergence criteria are selected such that either all the solutions should be in the first front or a limiting number of stagnant cycles should be observed during the iteration. Otherwise, the iterations stop after the maximum pre-defined number of generations are reached.

5.12 Optimization Parameters

A uniform fixed crossover of 0.7 and mutation fraction of 0.3 are used to produce next population. Maximum generation is selected to be 200 to terminate the algorithm. A summary of the optimization parameters is listed in Table 5.5.

Table 5.5 Summary of the optimization parameters

Parameter	Value
Population	140/100/80
Number of genes (n) in a chromosome	40/30/4
Max. generation number	200
Parent selection criterion	Binary tournament
Crossover fraction	0.7
Crossover method	Heuristic (continuous)/Scattered (discrete)
Mutation fraction	0.3
Mutation probability	$1/n$

6. RESULTS AND DISCUSSION

To this point, design characteristics of the ITU-TRR and the PBP, Monte-Carlo modeling of the reactor, basic requirements of the BNCT application, the employed GA method with the selected parameters and the developed beam shaping method were introduced. Using the information and data described above chapters, validation of the MCNP model, burnup-dependent spectrum calculations and beam shaping calculations steps are performed respectively and the results are presented below.

6.1 Validation of the MCNP Model

Criticality analyses are performed for the initial core loaded with fresh fuel when the control rods are in their bank positions and withdrawn entirely. The bank position of the rods, leading to a critical core, is adjusted to be 37.13 % of total active fuel length¹¹. A comparison between the results of MC method calculations and the data from the experiments are presented in Table 6.1. The results obtained by using different neutron libraries are listed in the same table.

Table 6.1 Effective multiplication factor

	Core Multiplication Factor, k_{eff}	
	Critical	Withdrawn
Experimental or SAR	1.00	1.0460
<i>MCNP5</i>		
ENDF/B-VII.0	1.00134 ± 0.00020	1.04603 ± 0.00021
ENDF/B-VI.8	1.00071 ± 0.00020	1.04585 ± 0.00021
JEFF-3.1.1	1.00213 ± 0.00020	1.04684 ± 0.00021
JEFF-3.1	1.00138 ± 0.00020	1.04669 ± 0.00021

The results indicate that the TRIGA core with out-core equipment is correctly modelled with MCNP. Maximum deviation of calculational results from the experimental data is obtained to be less than 0.08 % for the withdrawn condition and 0.2 % for the critical condition.

The experimental data has somewhat measurement errors, not greater than 10% [72]; thus, it can be concluded that outcomes of the MCNP model are, sufficiently, in good agreement with the experimental data.

In addition to experimental measurement errors, the SAR notifies that the fuel mass ranges from 36 to 40 g ²³⁵U per rod. Uncertainty in the fuel data, in particular in weight of ²³⁵U, apparently, leads to overestimated/underestimated consequences¹². Referring to the results, it

¹¹ Equals to a length of 14.147 cm where the length of fuel is 38.1 cm.

¹² The expected uncertainty due to composition is measured to be about ± 100 pcm [73] if the uncertainty in the weight of ²³⁵U is not greater than 10⁻³ relative to the total mass. (1 pcm = 10⁻⁵ Δk/k)

is clear that the uncertainty in the mass of fuel does not have a significant impact on the multiplication factor. However, mass distribution of the fissile material and the rod positions would be an important issue on the neutron flux distribution, and probably on the spent fuel content and burnup analysis.

There is a disparity among the used cross-section libraries as can be seen in table. However, still, uncertainties in material composition and geometry data provided by General Atomics are likely to surpass the uncertainties due to the libraries.

Since the critical CZP in equilibrium is used in all calculations, the temperature is assumed to be the same everywhere and thus the feedbacks (e.g., Doppler broadening, density change) are neglected. In reality, temperature and density vary with the position even though the reactor is at low power. Axial change of water density would lead to a variation in multiplication factor due to temperature and void feedbacks.

To sum up, it appears from the results that there is not much to be gained by modelling the reactor with further detail. That is, the current model produces acceptable results.

6.2 Burnup-Dependent Neutron Spectrum Calculations

Following the validation of the reactor model, up-to-date burnup level of the reactor core was obtained. For the operation sequence # 1599, the change of the core excess reactivity ($\$$) as a function of cumulative burnup (MWh) is illustrated in Fig. 6.1 with computational errors (as bar).

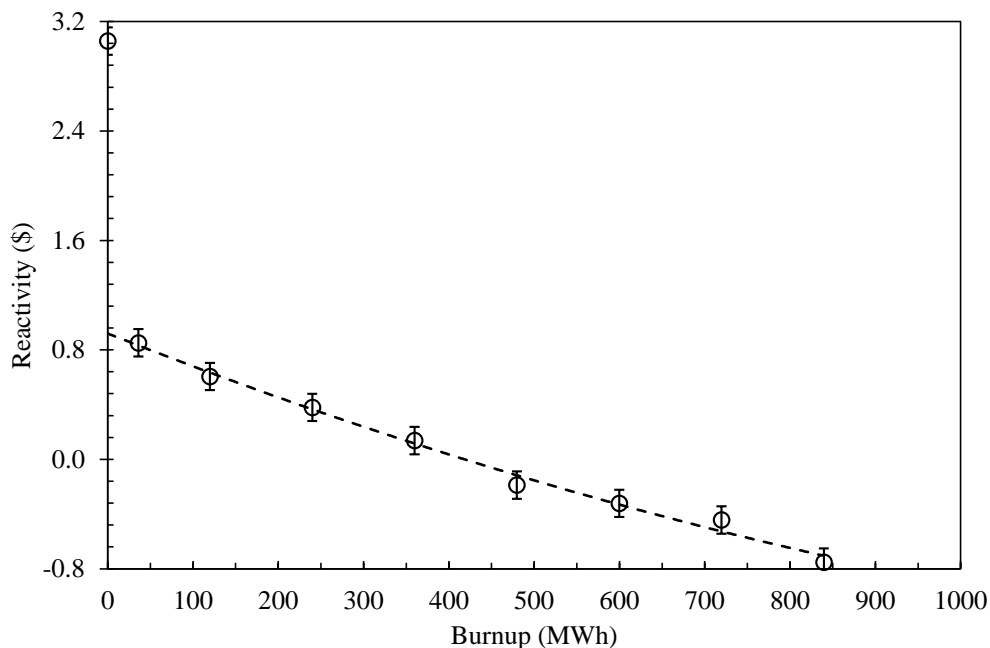


Fig. 6.1 Variation of the reactivity ($\$$) with the cumulative burnup (MWh)

Using the theory described in Section 3.3, the results are fitted to a second order polynomial equation (excluding the initial reactivity) with sufficient accuracy ($R^2=0.55$) to obtain the burnup level of the reactor core. Excess reactivity decreases smoothly (as quasi-linear) as the burnup goes up after a sharp decrease due to the FP poisoning. Burnup at sequence # 1599 is obtained to be 420 (17.5 MWd) \pm 12 MWh with a total irradiation time of 70 \pm 2 days.

As mentioned earlier, it has been decided to use the PBP in future studies for BNCT applications. For this purpose, effect of the burnup on the spectrum of the neutrons arriving to the BP is investigated. The energy distribution of incoming neutrons into the PBP at the Beginning of Life (BOL) and End of Life (EOL) is plotted in Fig. 6.2. The results are also provided in terms of fraction of BOL (EOL/BOL-1) in units of percentage.

From the results, it is observed that the spectrum¹³ is significantly affected from the change in burnup. Change of neutron distribution in epithermal energies with almost 5 % is higher than thermal energies. Impact of resonance overlap becomes important since the number of nuclides having higher resonance capture cross-section increase in the burned fuel with burnup. For instance, ¹⁵¹Sm isotope has large cross-section at the 6.16-7.52 eV. ²³⁸U has also large resonance peak in this energy range. Therefore, neutron spectrum plotted in Fig. 6.2 shows a significant fluctuation. It is also observed that there is no neutrons with energies less than 10⁻⁴ eV. Therefore, a burnup-dependent spectrum must be taken into account for the PBP calculations.

¹³ Maximum relative error does not exceed a value of about 4 % in the energy interval of 10⁻⁹-13 MeV.

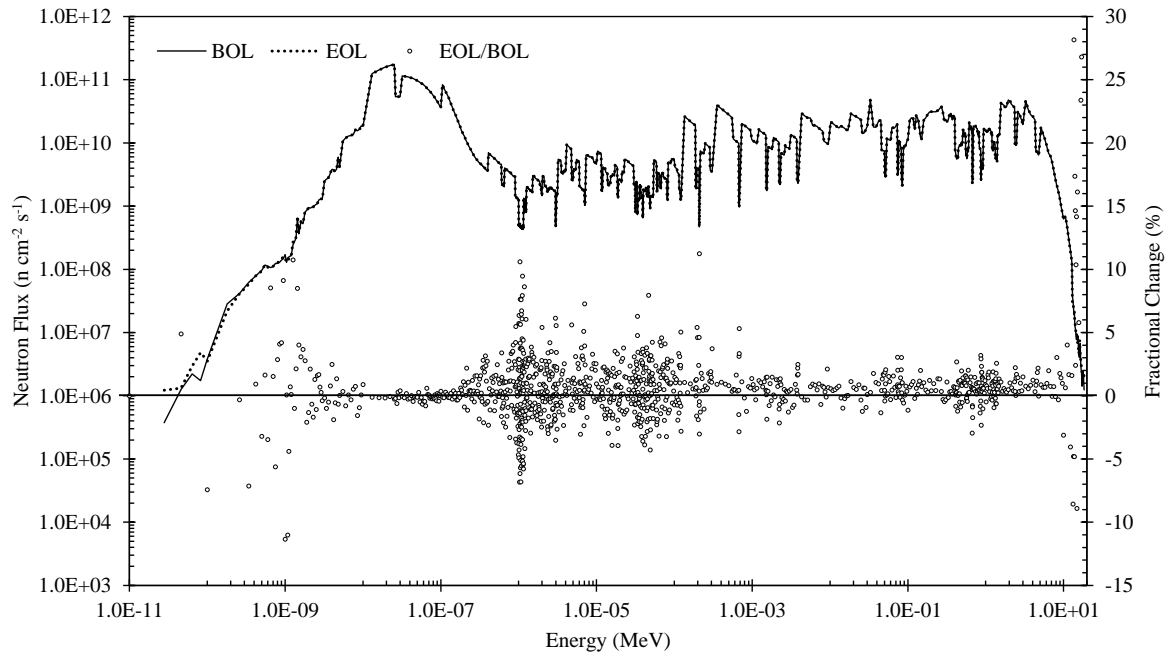


Fig. 6.2 Change of incoming neutron spectrum of the PBP at BOL and EOL

In the course of burnup analyses, CRs are fixed to a constant position and it is assumed that they do not move. However, in normal reactor operation, the positions of CRs, in particular the position of the regulating rod, are continuously changed to maintain criticality. This difference between the modeling and real operation results in acceptable modeling error.

Moreover, the reactor operates at varying power levels; but, in this model, it is assumed that it operates at the constant power for the burnup calculation. This affects accumulation of the poisonous FPs, the decay of some short-lived isotopes, and hence, the calculated burnup.

The results of the burnup calculations show that a burnup-corrected neutron spectrum must be used in the succeeding studies when BPs are modelled.

6.3 Design of Piercing Beam Port for the BNCT Application

At this point, the PBP was modeled alone and a surface source file, produced at the up-to-date burnup, was used in calculations. Results were provided when the BP was empty and also when the optimized patterns were used in the BP.

6.3.1 Particle Flux in the Bare PBP

MCNP view of the PBP is shown in Fig. 6.3 when the BP is bare. In the figure, port entry, extension and exit surfaces are the surfaces at which the particle spectrum is obtained. In the same figure, tally surfaces for the flux calculations are illustrated as the vertical lines to the BP.

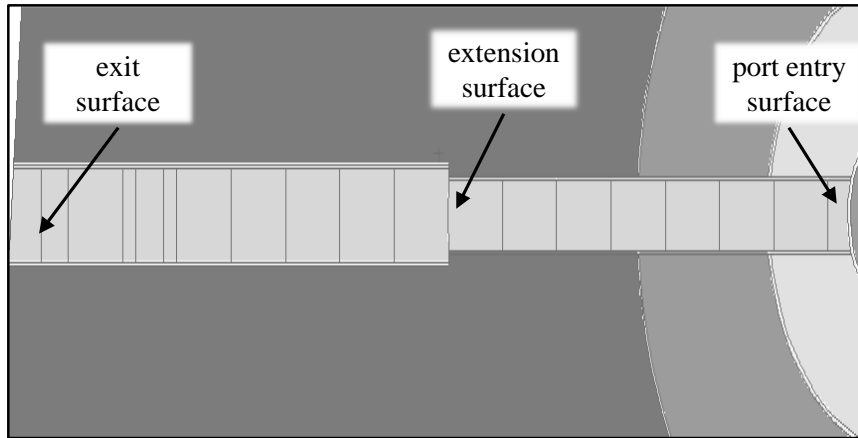


Fig. 6.3 MCNP view of the bare PBP

Change of particle flux with the distance from the core center in the bare BP is illustrated in Fig. 6.4. All the fluxes decrease, by showing similar trend, as the distance from the core center increases. Decrease in the fluxes is due to leakage from the BP and interaction of particles with the materials which surround the BP. Thermal neutrons do not decrease as fast as the others. This is because some of the epithermal and fast neutrons which leak out or scatter from the enclosed materials eventually turn back into the BP as thermal ones. Losses in other fluxes become gain for the thermal neutrons. While the incoming fluxes at the BP inlet are in the order of $10^{12} \text{ n cm}^{-2} \text{ s}^{-1}$, the outgoing fluxes at the BP exit reduce to the order of $10^9 \text{ n cm}^{-2} \text{ s}^{-1}$. Fluxes decrease rapidly until the extension surface and then decrease in the fluxes lessens. Change of the neutron fluxes with the port radius at the port entry and exit surfaces is plotted in Fig. 6.5. Intensity of the beam increases through the center of radius. For all group fluxes, trend is the same. Neutron flux distribution changes significantly as the distance increases from the core center.

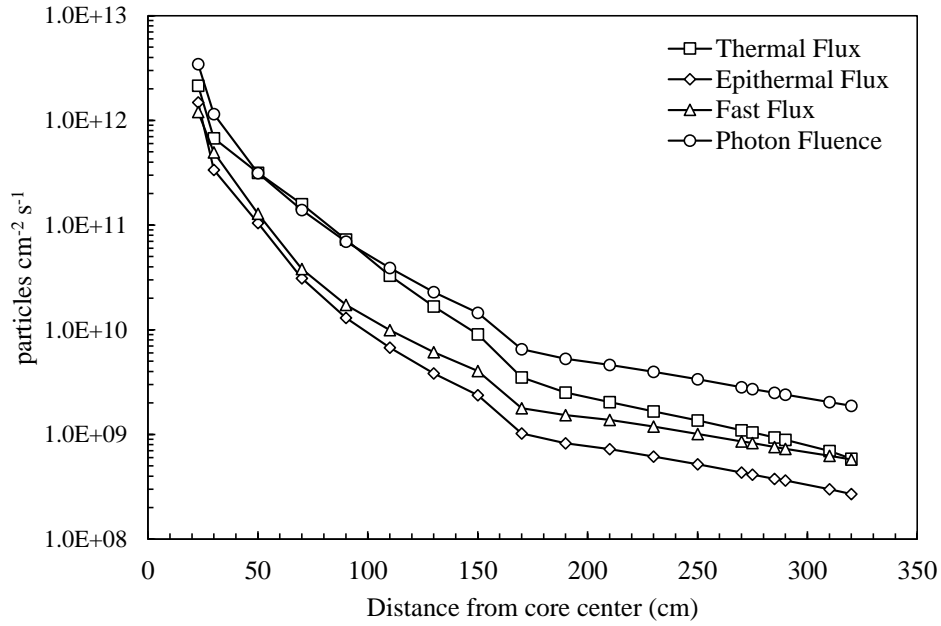


Fig. 6.4 Change of particle flux along with distance from the core center

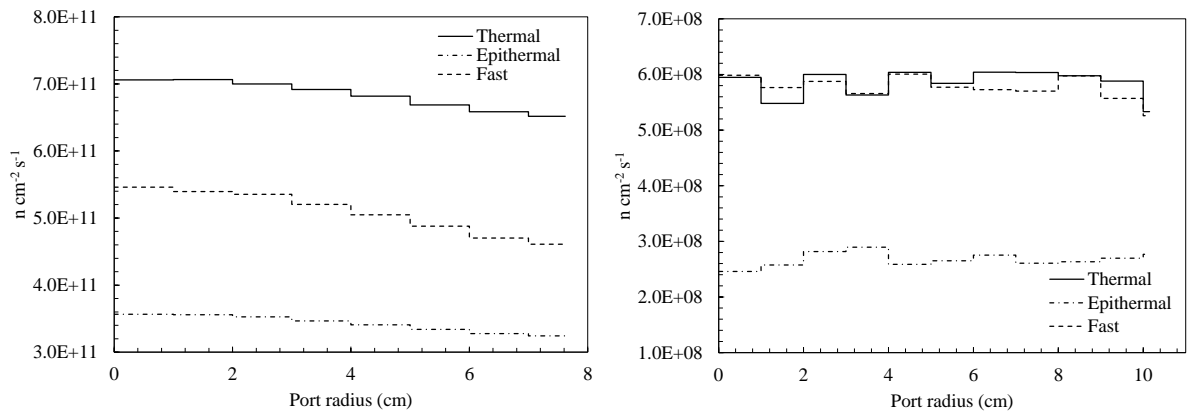


Fig. 6.5 Change of particle flux along with radius of PBP: at the port entry surface (left) and at the port exit surface (right)

Particle spectrum at various port locations (entry, extension and exit) is presented in Fig. 6.6 for neutrons and in Fig. 6.7 for photons. Penetration of the thermal neutrons through the BP reduces considerably and low energy part of thermal group disappear at the port exit. However, shape of the spectrum seems preserved. Thermal and fast fluxes should be decreased to get a desired beam of neutrons for the BNCT. In the case of photon spectrum, the shape changes significantly.

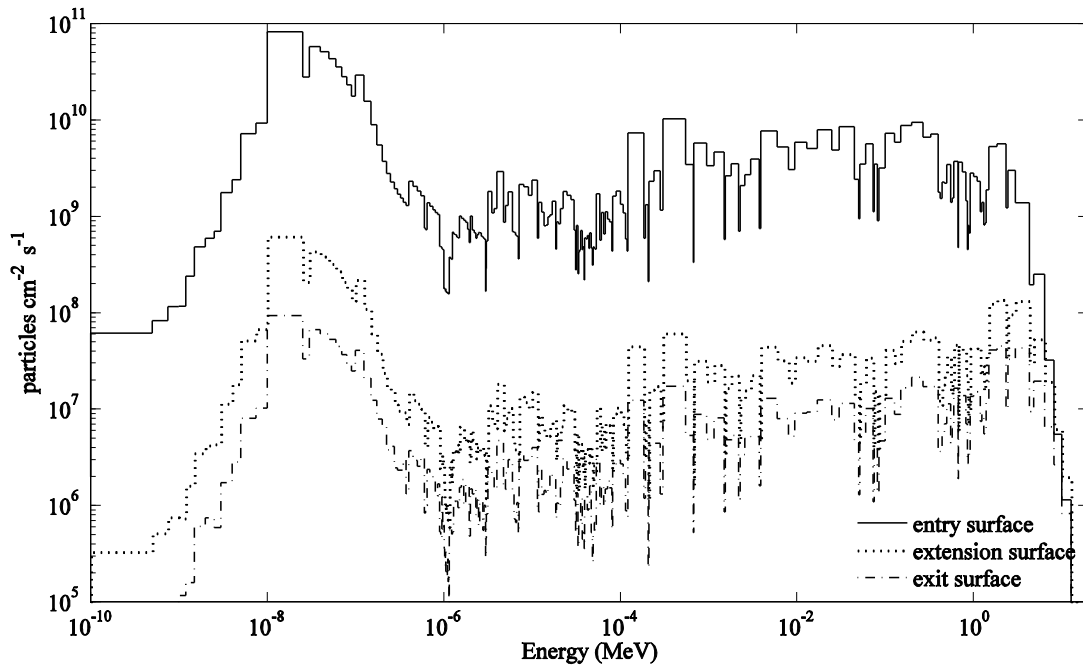


Fig. 6.6 Neutron spectra at various port locations

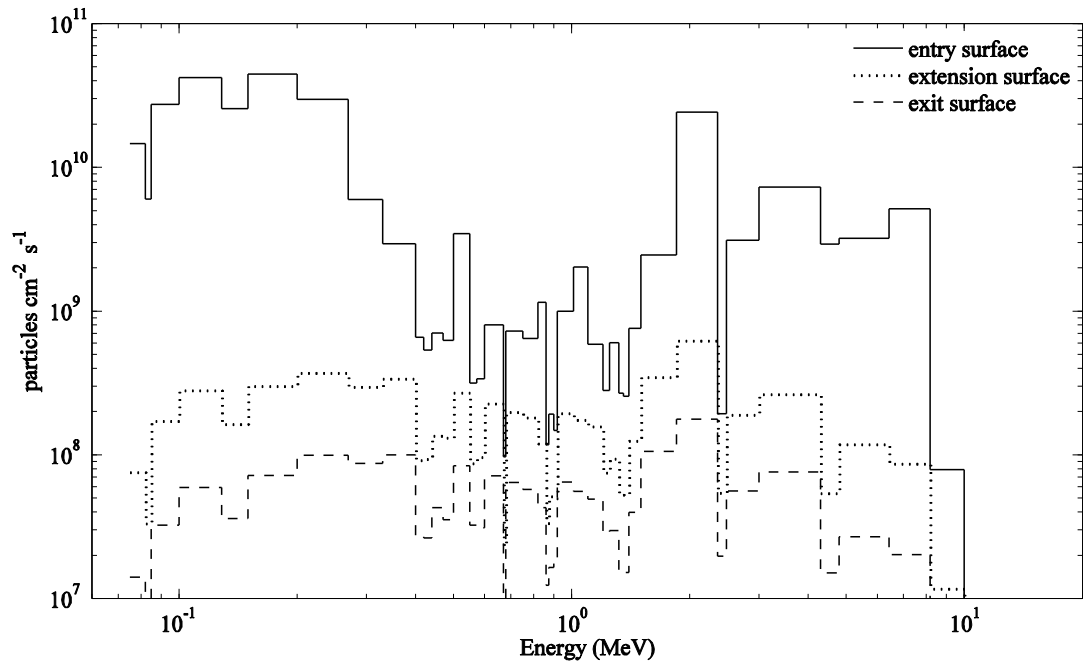


Fig. 6.7 Photon spectra at various port locations

6.3.2 GA Results for Spectrum Shifter Sub-pattern Optimization

While no pattern is loaded into the BP (so-called bare BP), fluxes for thermal, epithermal and fast neutrons are tabulated in Table 6.3. An epithermal neutron flux of about $4.1 \times 10^8 \text{ n cm}^{-2} \text{ s}^{-1}$ is obtained at the end of location where the spectrum shifter patterns are to be placed. In addition, a thermal neutron flux of about $1.0 \times 10^9 \text{ n cm}^{-2} \text{ s}^{-1}$ and a fast neutron flux of about $8.3 \times 10^8 \text{ n cm}^{-2} \text{ s}^{-1}$ are calculated. As seen from the results, without using the spectrum shifter

patterns, fast neutron flux is too high to use in BNCT. Therefore, a proper spectrum shifter pattern which would slow the fast neutrons down into epithermal energy range is investigated by employing the GA method detailed in Section 5.5.1.

Using the materials listed in Table 5.2, the GA results are presented in Fig. 6.8. The results are provided in terms of Pareto-front solutions, epithermal neutron flux solutions with respect to generation number, solution space and evolution of the solutions at initial, midway and final generations.

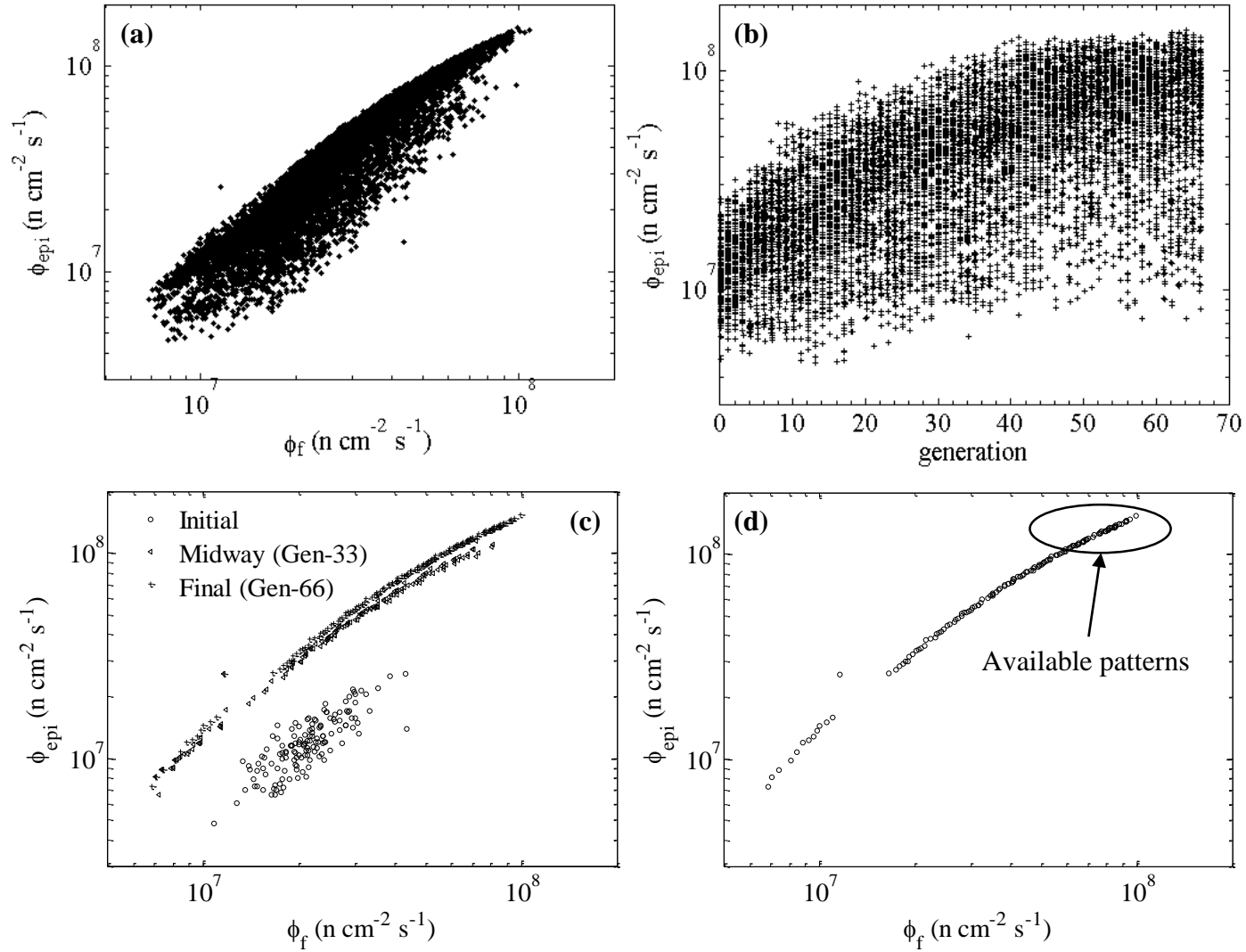


Fig. 6.8 Optimization results for Spectrum Shifter sub-patterns: (a) Solution space, (b) Epithermal neutron flux solutions with respect to generation number, (c) Evolution of the solutions at initial, midway and final generations and (d) Pareto-front solutions.

The solution space, shown in Fig. 6.8 (a), indicates that all the solutions are in the range of 2.0 and $0.4 \times 10^8 \text{ n cm}^{-2} \text{ s}^{-1}$ for epithermal neutron flux and in the range of 0.6 and $1.0 \times 10^8 \text{ n cm}^{-2} \text{ s}^{-1}$ for fast neutron flux. Since all the solutions are (assigned as) in the first front, the iterations appear to be converged. In addition, a well spread of the epithermal neutron flux solution, shown in (b), is obtained at the final generation. As the generation number increases, the solutions, shown in (c), approach to pareto-optimal solution line. The line, shown in (d), has a continuous linear slope, neither concave or convex nor discrete.

The best pattern (SP₁), which gives the lowest fast neutron flux within the pareto-front solutions, has a fast flux of $6.9 \times 10^6 \text{ n cm}^{-2} \text{ s}^{-1}$ and an epithermal neutron flux of $7.3 \times 10^6 \text{ n cm}^{-2} \text{ s}^{-1}$. However, the obtained epithermal flux is not useful any more for the BNCT since it has a lower value than the desired value although the contribution of fast neutrons is reduced by 120 times. The other best pattern (SP₂), which gives the highest epithermal neutron flux within the pareto-front solutions, has a fast flux of $9.9 \times 10^7 \text{ n cm}^{-2} \text{ s}^{-1}$ and an epithermal neutron flux of $1.5 \times 10^8 \text{ n cm}^{-2} \text{ s}^{-1}$. The obtained epithermal flux seems useful even without collimating the beam. A reduction in the fast flux by 8 times is achieved with a reduction of about 3 times in the epithermal flux.

To further reduce the dose contribution due to fast neutrons of the beam, either a pattern may be used several times in succession or a combination of the suggested patterns may be used. As an example, if the SP₂ is used twice in the BP, a reduction of nearly 70 times in the fast flux is possible; but, the epithermal flux reduces about one-eighth of its bare value. If the length of this pattern, preserving the material content, is reduced by half, in this case epithermal flux decreases to about 60 % of its bare value.

It can be deduced that the candidate patterns must be among the patterns which would make sure an epithermal flux of $> 1.0 \times 10^8 \text{ n cm}^{-2} \text{ s}^{-1}$. The available patterns are pointed out on Fig. 6.8 (d) and tabulated in Table 6.2. In the table, the regions filled with the air are excluded from the patterns due to having negligible interaction¹⁴ probability with the neutrons. Only the existing materials inside the patterns are presented in the table with their total thicknesses.

In addition, a filtering ratio for the epithermal (r_{epith}) and fast (r_{fast}) neutrons is defined to find out the pattern efficiency. The filtering ratio is defined as the ratio of bare neutron flux to shifted neutron flux. A high r_{fast} and a low r_{epith} are desired; but, both may not be optimized all at once. Therefore, an overall coefficient, $r_{\text{fast}} / r_{\text{epith}}$, is also defined. The highest value means

¹⁴ Air behaves like an empty space for the neutrons with an exceeding average track mean free path of 600 cm.

the most efficient pattern. However, in this case, as the efficiency increases, r_{epith} also increases. Besides fast neutrons, some of the epithermal neutrons inevitably interact with the pattern materials and as a consequence, are filtered by the pattern.

According to the results, the patterns presented at the end of the table are the most effective patterns in slowing down the fast neutrons with a fast-to-epithermal ratio of 3.5; however, those patterns reduce epithermal neutron flux to one-fourth of its bare value. The available patterns are mostly composed of a combination of sulfur, argon and aluminum-based materials. It is clear that Al and Ar are the most suitable materials to form a good spectrum shifter pattern. Results also indicate that some of the suggested materials such as Li, Kr and Bi are eliminated. Results show that the best pattern has an overall $r_{\text{fast}} / r_{\text{epith}}$ ratio of 3.1 and made up of 13 cm thick Al, 11 cm thick Ar, 9 cm thick S, 3 cm thick K and, 1 cm thick Si and Al_2O_3 foils.

Table 6.2 Available patterns for the spectrum shifter sub-pattern design

Neutron Flux $10^8 \text{ n cm}^{-2} \text{ s}^{-1}$					Pattern Material Content (cm)						
Φ_{epith}	Φ_{fast}	r_{epith}	r_{fast}	$r_{\text{fast}}/r_{\text{epith}}$	Al	$^{\text{nat}}\text{Ar}$	$^{\text{nat}}\text{S}$	$^{\text{nat}}\text{K}$	Si	Al_2O_3	AlF_3
1.533	0.996	2.7	8.3	3.1	13	11	9	3	1	1	0
1.470	0.949	2.8	8.7	3.1	14	10	9	3	1	1	0
1.457	0.927	2.8	8.9	3.1	12	10	10	2	1	1	1
1.444	0.925	2.9	8.9	3.1	14	10	9	2	0	1	1
1.438	0.918	2.9	9.0	3.1	14	9	8	2	1	1	1
1.410	0.893	2.9	9.3	3.2	13	10	9	2	0	1	2
1.402	0.884	3.0	9.3	3.2	15	9	9	2	0	1	1
1.402	0.879	3.0	9.4	3.2	14	10	8	2	1	1	1
1.386	0.861	3.0	9.6	3.2	14	10	10	2	0	1	1
1.372	0.856	3.0	9.7	3.2	15	10	9	2	0	1	1
1.361	0.851	3.0	9.7	3.2	15	9	9	3	0	1	1
1.352	0.850	3.1	9.7	3.2	14	10	6	3	1	1	2
1.344	0.847	3.1	9.8	3.2	15	8	10	3	0	1	1
1.344	0.836	3.1	9.9	3.2	15	9	10	2	0	1	1
1.339	0.822	3.1	10.0	3.3	16	10	8	1	0	1	1
1.322	0.815	3.1	10.1	3.2	15	10	9	1	1	1	1
1.308	0.814	3.2	10.2	3.2	16	9	9	1	0	1	1
1.303	0.809	3.2	10.2	3.2	13	9	10	2	1	1	2
1.300	0.802	3.2	10.3	3.2	17	10	7	1	0	1	1
1.293	0.793	3.2	10.4	3.3	16	9	9	3	0	1	1
1.286	0.792	3.2	10.4	3.2	16	8	10	2	0	1	1
1.285	0.772	3.2	10.7	3.3	15	11	8	1	0	1	2
1.280	0.769	3.2	10.7	3.3	17	10	8	1	0	1	1
1.255	0.768	3.3	10.8	3.3	14	8	9	3	1	1	2
1.252	0.759	3.3	10.9	3.3	15	11	7	1	1	1	2
1.248	0.733	3.3	11.3	3.4	16	11	7	1	0	1	2
1.217	0.725	3.4	11.4	3.3	14	10	9	2	0	1	3
1.194	0.703	3.5	11.8	3.4	15	10	9	2	1	1	2
1.182	0.699	3.5	11.8	3.4	16	9	9	3	0	1	2
1.176	0.692	3.5	11.9	3.4	17	9	8	1	0	1	2
1.171	0.689	3.5	12.0	3.4	16	7	10	1	1	1	2
1.167	0.681	3.5	12.1	3.4	17	11	7	1	0	1	2
1.153	0.680	3.6	12.2	3.4	17	8	10	1	0	1	2
1.143	0.679	3.6	12.2	3.4	16	10	8	2	0	0	3
1.140	0.671	3.6	12.3	3.4	15	10	7	1	1	1	3
1.133	0.657	3.7	12.6	3.4	18	9	8	1	0	1	2
1.120	0.654	3.7	12.6	3.4	16	9	8	2	0	1	3
1.109	0.651	3.7	12.7	3.4	17	7	8	3	1	1	2
1.104	0.645	3.8	12.8	3.4	16	7	12	2	0	1	2
1.102	0.634	3.8	13.0	3.5	18	11	6	1	1	1	2

A selected suitable pattern for the BNCT is depicted in Fig. 6.9. Sequence of the materials is presented below the figure. The divisions filled with the same materials inside the pattern are visualized with the same color. The pattern is made up of 1.8 cm thick Ti, 1.5 cm thick Cd and 0.3 cm thick ^{232}Th . Effect of this pattern on the neutron fluxes is shown in Table 6.3. Incoming particle fluxes are calculated at the entry surface of the pattern enclosed with the port radius while outgoing particle fluxes are calculated at the exit surface of the pattern enclosed with the port radius. The fluxes reported are the values averaged over the considered surfaces.

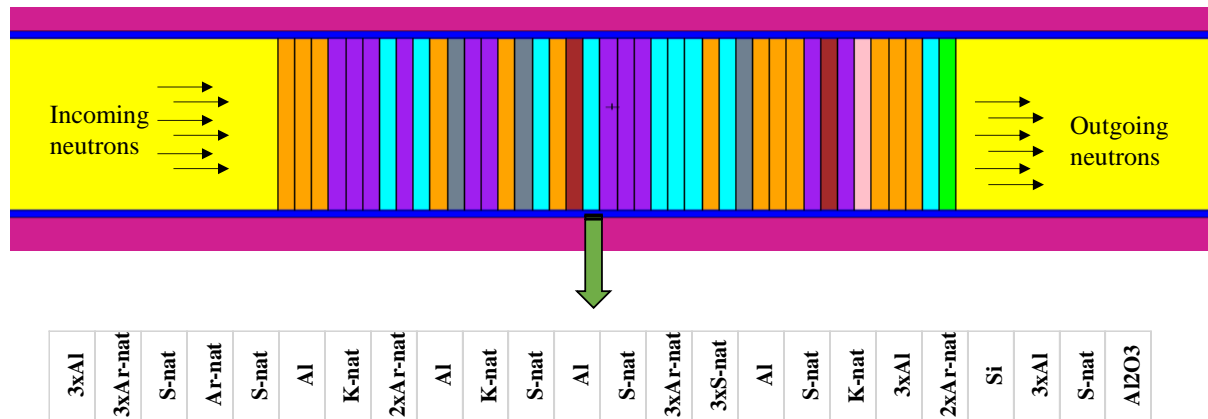


Fig. 6.9 A selected pattern for the spectrum shifter
 Table 6.3 Particle fluxes with and without the sub-pattern

	Incoming Particle Flux	Outgoing Particle Flux	
		Bare	Sub-pattern
Φ_{th} (n/cm ² .s)	$2.034 \pm 0.0041 \times 10^9$	$1.044 \pm 0.0060 \times 10^9$	$2.498 \pm 0.0142 \times 10^8$
Φ_{epi} (n/cm ² .s)	$7.232 \pm 0.0087 \times 10^8$	$4.140 \pm 0.0116 \times 10^8$	$1.533 \pm 0.0095 \times 10^8$
Φ_{fast} (n/cm ² .s)	$1.376 \pm 0.0069 \times 10^9$	$8.264 \pm 0.0090 \times 10^8$	$0.996 \pm 0.0117 \times 10^8$
I_γ (γ/cm ² .s)	$4.622 \pm 0.0059 \times 10^9$	$2.715 \pm 0.0079 \times 10^9$	-

6.3.3 GA Results for Filtering Sub-pattern Optimization

Fluxes for thermal, epithermal and fast energy groups are tabulated in Table 6.5 for the bare BP. An epithermal neutron flux of about $3.8 \times 10^8 \text{ n cm}^{-2} \text{ s}^{-1}$ is obtained at the end of location where the filtering patterns are to be placed. In addition, a thermal neutron flux of about $9.4 \times 10^8 \text{ n cm}^{-2} \text{ s}^{-1}$ and a fast neutron flux of about $7.6 \times 10^8 \text{ n cm}^{-2} \text{ s}^{-1}$ are calculated. As seen from the results, without using the filtering patterns, thermal neutron flux is too high to use for

BNCT. Therefore, a useful filtering pattern which would eliminate thermal neutron contribution of the beam is investigated by employing the GA method detailed in Section 5.5.2. Using the materials given in Table 5.3, the GA results are presented in Fig. 6.10. The results are provided in terms of Pareto-front solutions, epithermal neutron flux solutions with respect to generation number, solution space and evolution of the solutions at initial, midway and final generations.

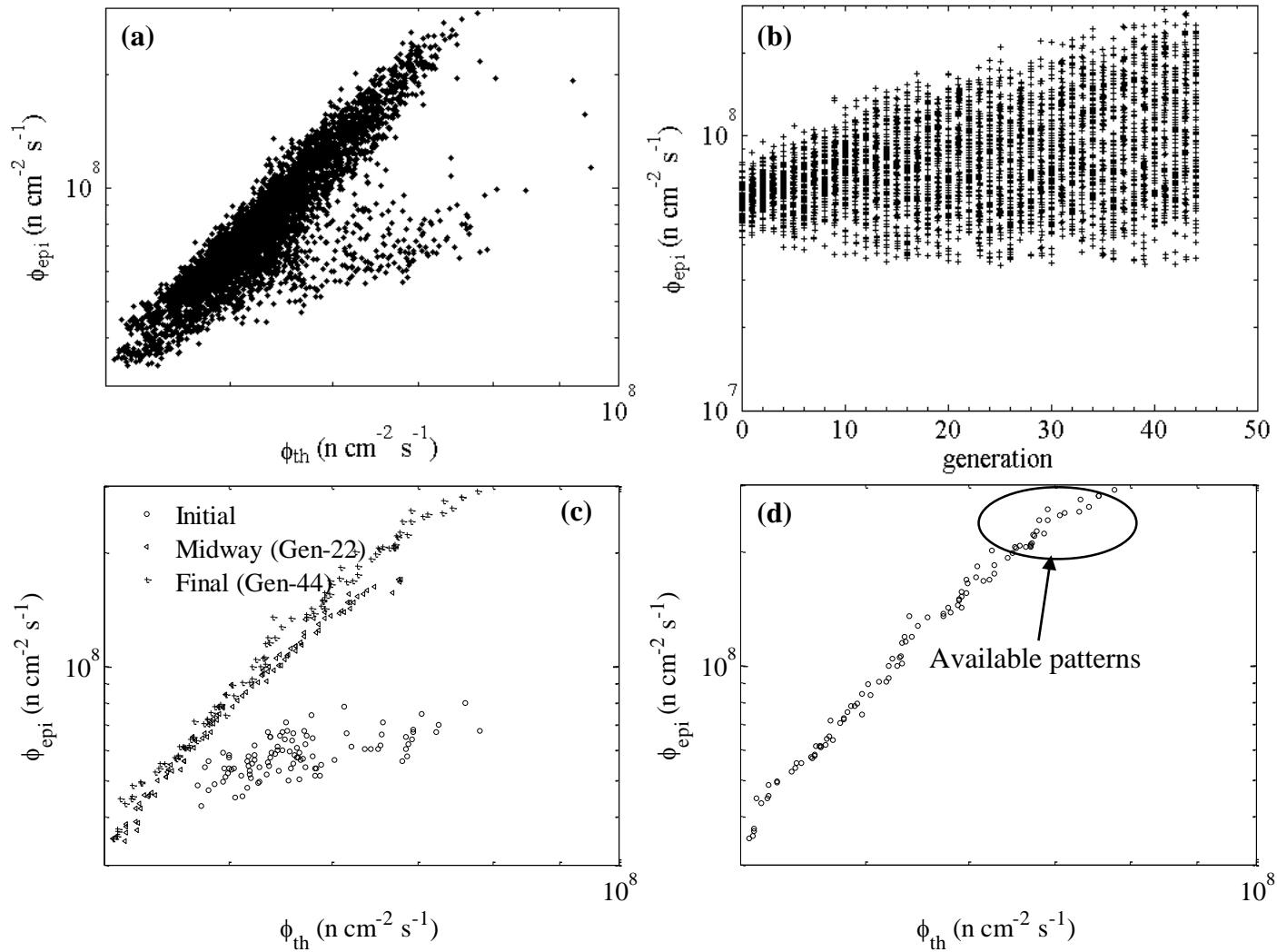


Fig. 6.10 Optimization results for Filtering sub-patterns: (a) Solution space, (b) Epithermal neutron flux solutions with respect to generation number, (c) Evolution of the solutions at initial, midway and final generations and (d) Pareto-front solutions.

The solution space, shown in Fig. 6.10 (a), indicates that all the solutions are obtained in the epithermal neutron flux range of 3.0 and $0.3 \times 10^8 \text{ n cm}^{-2} \text{ s}^{-1}$ and in the thermal neutron flux range of 0.4 and $1.0 \times 10^8 \text{ n cm}^{-2} \text{ s}^{-1}$. Since all the solutions are (assigned as) in the first front, the iterations appear to be converged. In addition, a well spread of the epithermal neutron flux solution, shown in (b), is obtained at the final generation. As the generation increases, the solutions, shown in (c), approach to pareto-optimal solution line. The line, shown in (d), has a continuous linear slope, not concave or convex or discrete.

The best pattern (FP₁), which gives the lowest thermal neutron flux within the pareto-front solutions, has a thermal flux of $4.1 \times 10^7 \text{ n cm}^{-2} \text{ s}^{-1}$ and an epithermal neutron flux of $3.5 \times 10^7 \text{ n cm}^{-2} \text{ s}^{-1}$. However, the obtained epithermal flux is not useful any more for the BNCT due to providing too much lower value than the desired value although the contribution of thermal neutrons is reduced by 22 times. The other best pattern (FP₂), which gives the highest epithermal neutron flux within the pareto-front solutions, has a thermal flux of $7.8 \times 10^7 \text{ n cm}^{-2} \text{ s}^{-1}$ and an epithermal neutron flux of $2.9 \times 10^8 \text{ n cm}^{-2} \text{ s}^{-1}$. The obtained epithermal flux seems useful even without collimating the beam. A reduction of 12 times in the thermal flux is achieved with almost no cost paid for the epithermal flux.

To further reduce the dose contribution due to thermal neutrons of the beam, either a pattern may be used several times in succession or a combination of the suggested patterns may be used. As an example, if the FP₂ is used twice in the BP, a reduction of nearly 144 times in the thermal flux is possible while the epithermal flux is likely to obtain only a half of its bare value.

In a nutshell, it can be concluded that the candidate patterns must be among the patterns which would make sure an epithermal flux of $> 1.0 \times 10^8 \text{ n cm}^{-2} \text{ s}^{-1}$. The available patterns are pointed out on Fig. 6.10 (d) and tabulated in Table 6.4. In the table, the regions filled with the air material are excluded from the patterns due to having negligible interaction probability with the neutrons.

In addition, a filtering ratio for the thermal (r_{th}) and epithermal (r_{epith}) neutrons is defined to find out the pattern efficiency. The filtering ratio is defined as the ratio of bare neutron flux to filtered neutron flux. A high r_{th} and a low r_{epith} are desired; but, both may not be optimized all at once. Therefore, an overall coefficient, $r_{\text{th}} / r_{\text{epith}}$, is also defined. The highest value means the most efficient pattern.

According to the results, first fifteen patterns listed in Table 6.4 are the most effective patterns in eliminating the thermal neutrons, without significantly absorbing the epithermal neutrons.

The patterns are mostly composed of a combination of Cd and Ti materials. It is clear that Cd and Ti are the most proper materials to form a good filtering pattern. It is interesting to note that some of the filtering materials suggested in the literature such as Hf, W and Au do not exist in the patterns. Table also shows that In, Th, Ag, B₄C and in some cases Gd are very effective in reducing the thermal neutron contribution.

The best pattern has an overall r_{th} / r_{epith} ratio of 9.3 and made up of 1.8 cm thick Cd foil and 1.8 cm thick Ti foil.

Table 6.4 Available patterns for the filtering sub-pattern design

Neutron Flux $10^8 \text{ n cm}^{-2} \text{ s}^{-1}$					Pattern Material Content (cm)								
Φ_{epith}	Φ_{th}	r_{epith}	r_{th}	r_{th}/r_{epith}	^{nat} Cd	^{nat} Ti	Th	^{nat} In	^{nat} Ag	B ₄ C	^{nat} W	^{nat} Au	^{nat} Gd
2.906	0.777	1.30	12.0	9.29	1.8	2.1							
2.797	0.756	1.35	12.4	9.19	1.5	1.8							
2.790	0.757	1.35	12.4	9.15	1.2	2.1							
2.745	0.732	1.37	12.8	9.32	1.8	1.8							
2.628	0.744	1.43	12.6	8.77	1.5	1.8	0.3						
2.572	0.691	1.46	13.5	9.24	0.6	2.1		0.3					
2.546	0.731	1.48	12.8	8.65	2.1	1.5	0.3						
2.531	0.712	1.49	13.1	8.83	1.2	1.8		0.3					
2.483	0.706	1.52	13.2	8.73	1.5	1.5			0.3				
2.412	0.680	1.56	13.7	8.81	1.5	1.8		0.3					
2.406	0.691	1.56	13.5	8.64	1.2	1.5	0.3	0.3					
2.258	0.677	1.67	13.8	8.28	0.9	1.5	0.3			0.6			
2.220	0.686	1.70	13.6	8.03	0.9	2.1		0.9					
2.211	0.673	1.70	13.9	8.16	0.9	2.1	0.3	0.6					
2.193	0.675	1.72	13.8	8.06	1.2	2.4	0.3	0.3					
2.094	0.672	1.80	13.9	7.74	1.2	1.5		0.6	0.3				
2.088	0.671	1.80	13.9	7.73	0.9	1.8	0.3	0.3	0.3				
2.066	0.671	1.82	13.9	7.65	1.2	1.8	0.3	0.9					
2.064	0.657	1.82	14.2	7.81	0.9	2.1	0.3	1.2					
2.060	0.671	1.83	13.9	7.62	0.9	1.8	0.3		0.3			0.3	
2.053	0.652	1.83	14.3	7.82	0.9	1.5	0.3	0.6	0.3				
2.048	0.664	1.84	14.1	7.66	0.9	1.8	0.3	0.6			0.3		
2.045	0.653	1.84	14.3	7.78	1.5	1.8		0.3			0.3		
2.009	0.626	1.87	14.9	7.97	0.6	1.8		0.3			0.6		
1.976	0.649	1.91	14.4	7.56	1.8	1.8			0.3		0.3		
1.929	0.644	1.95	14.5	7.44	0.6	2.1	0.3	0.6	0.3				
1.843	0.629	2.04	14.9	7.28	1.5	1.2			0.3		0.3		0.3
1.820	0.610	2.07	15.3	7.41	0.9	1.8	0.3			0.3			
1.746	0.629	2.16	14.9	6.90	1.2	2.1	0.3				0.3		
1.708	0.609	2.20	15.4	6.97	1.2	1.5	0.6				0.3		
1.686	0.622	2.23	15.0	6.73	0.9	1.8	0.3	0.3			0.3		
1.678	0.598	2.24	15.6	6.97	1.5	1.5			0.3	0.3			
1.673	0.616	2.25	15.2	6.74	1.2	1.8			0.3	0.3			
1.647	0.599	2.29	15.6	6.83	1.2	1.8			0.3	0.3			
1.561	0.593	2.41	15.8	6.54	1.2	1.2	0.6	0.3	0.3	0.3			
1.552	0.597	2.43	15.6	6.45	1.5	1.2	0.6	0.3	0.3	0.3			

A selected suitable pattern selected for the BNCT is depicted in Fig. 6.11. Sequence of the materials is presented below the figure. The divisions filled with the same materials inside the pattern are visualized with the same color. The pattern is made up of 1.8 cm thick Ti, 1.5 cm thick Cd, and 0.3 cm thick ^{232}Th . Effect of this pattern on the neutron fluxes is shown in Table 6.5. Incoming particle fluxes are calculated at the entry surface of the pattern enclosed with the port radius while outgoing particle fluxes are calculated at the exit surface of the pattern enclosed with the port radius. The fluxes reported are the values averaged over the considered surfaces.

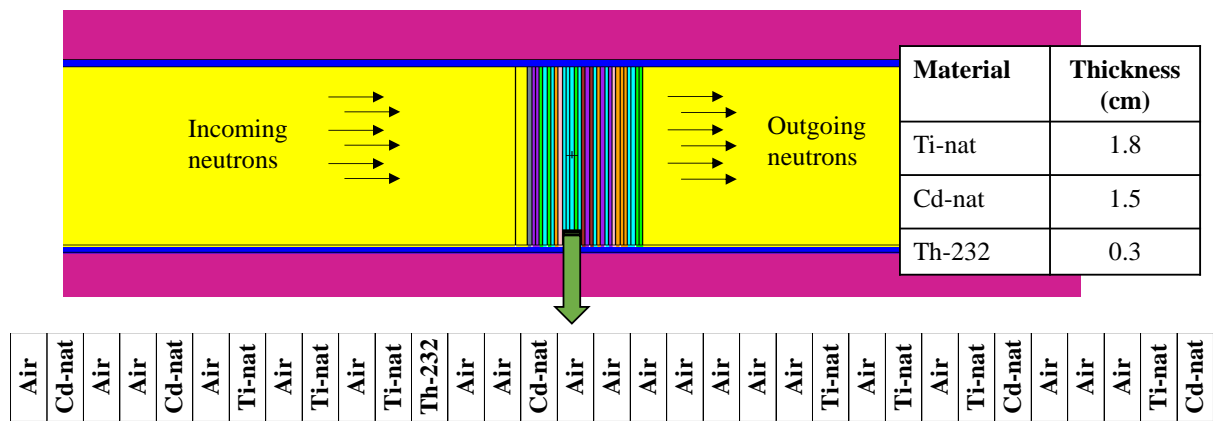


Fig. 6.11 A selected pattern for the filtering

Table 6.5 Particle fluxes with and without the sub-pattern

	Incoming Particle Flux		Outgoing Particle Flux	
		Bare	Sub-pattern	
Φ_{th} (n/cm ² .s)	$1.044 \pm 0.0060 \times 10^9$	$9.353 \pm 0.0063 \times 10^8$	$7.440 \pm 0.026 \times 10^7$	
Φ_{epi} (n/cm ² .s)	$4.140 \pm 0.0116 \times 10^8$	$3.765 \pm 0.0122 \times 10^8$	$2.628 \pm 0.030 \times 10^8$	
Φ_{fast} (n/cm ² .s)	$8.264 \pm 0.0090 \times 10^8$	$7.596 \pm 0.0094 \times 10^8$	$6.304 \pm 0.027 \times 10^8$	
I_{γ} (γ/cm ² .s)	$2.715 \pm 0.0079 \times 10^9$	$1.873 \pm 0.0096 \times 10^9$	-	

6.3.4 GA Results for Collimator Sub-pattern Optimization

Neutron fluxes for thermal, epithermal and fast neutron energy groups are tabulated in Table 6.7 for the bare BP. An epithermal neutron flux of about $2.7 \times 10^8 \text{ n cm}^{-2} \text{ s}^{-1}$ is obtained at the end of location where the collimator is to be placed. In addition, a thermal neutron flux of about $5.9 \times 10^8 \text{ n cm}^{-2} \text{ s}^{-1}$ and a fast neutron flux of about $5.8 \times 10^8 \text{ n cm}^{-2} \text{ s}^{-1}$ are calculated. Neutron current to flux ratio is calculated to be 0.89. As seen from the results, without using the

collimator, epithermal neutron flux is not adequately sufficient to use in the BNCT. Therefore, a useful collimator design which would yield a highly collimated beam of epithermal neutrons is examined by employing the GA method detailed in Section 5.5.3.

Using the materials presented in Table 5.4, the GA results obtained are presented in Fig. 6.12. The results are provided in terms of Pareto-front solutions, epithermal neutron flux solutions with respect to generation number, solution space and evolution of the solutions at initial, midway and final generations.

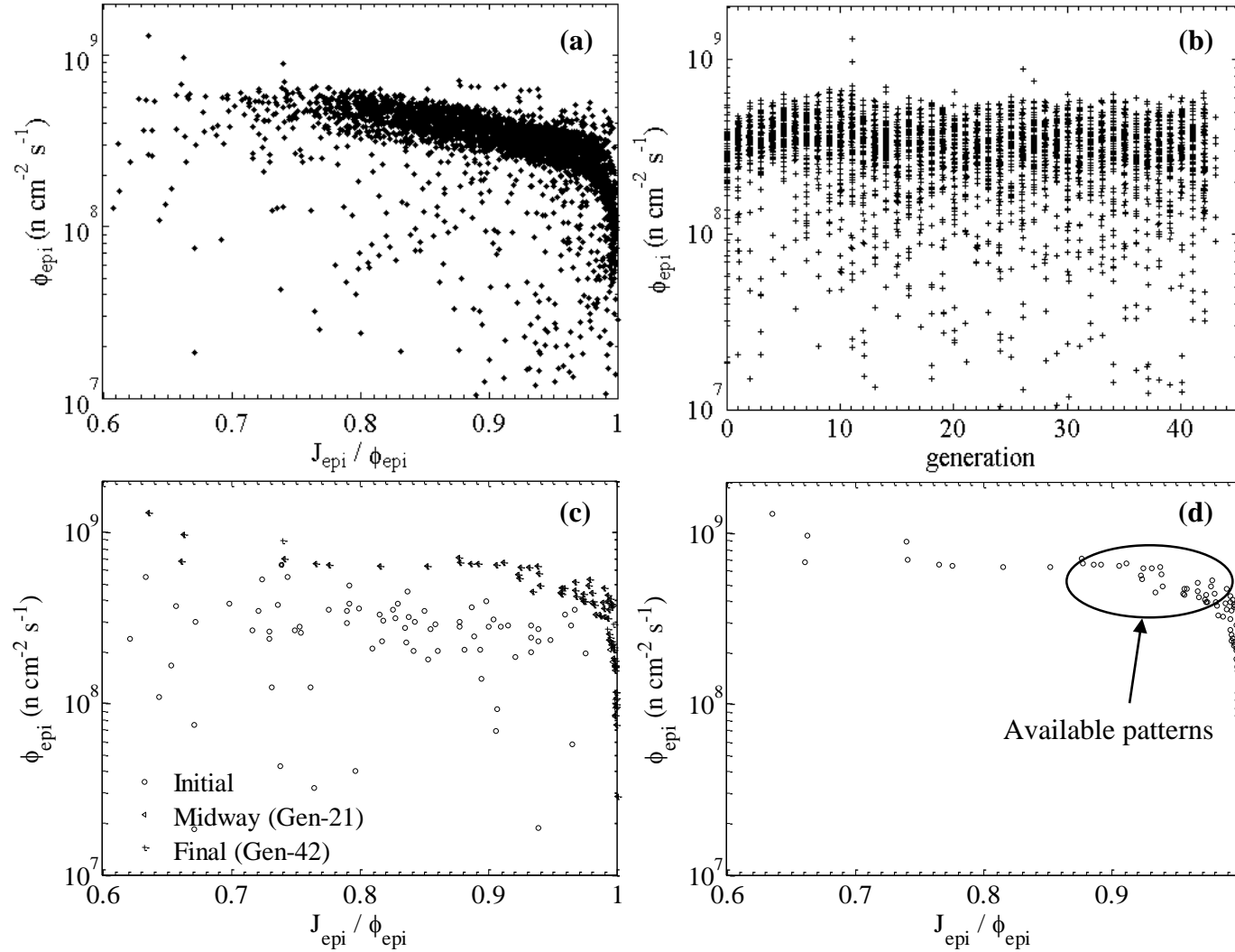


Fig. 6.12 Optimization results for Collimator sub-patterns: (a) Solution space, (b) Epithermal neutron flux solutions with respect to generation number, (c) Evolution of the solutions at initial, midway and final generations and (d) Pareto-front solutions.

The solution space, shown in Fig. 6.12 (a), indicates that all the solutions change from 0.1 to $10.0 \times 10^8 \text{ n cm}^{-2} \text{ s}^{-1}$ for the epithermal neutron flux and from 0.6 to 1.0 for the neutron current to flux ratio. Since all the solutions are (assigned as) in the first front, the iterations appear to be converged. In addition, epithermal neutron flux solutions, shown in (b), pack around $3.0 \times 10^8 \text{ n cm}^{-2} \text{ s}^{-1}$. Furthermore, the solutions for epithermal neutron flux seem to be not dispersed evenly between the lower and upper bounds; instead, they are positioned close to the upper bound. As the generation number increases, the solutions, shown in (c), approach to pareto-optimal solution line. The line, shown in (d), has a continuous concave slope, not linear or convex or discrete.

The best pattern (CP₁), which gives the highest epithermal neutron flux within the pareto-front solutions, has an epithermal flux of $1.3 \times 10^9 \text{ n cm}^{-2} \text{ s}^{-1}$ and an epithermal neutron current to flux ratio of 0.64. However, the obtained ratio is not sufficient to get the desired value mentioned in Section 4.2 although the epithermal neutron flux is increased by 4 times compared with the bare value. The other best pattern (CP₂), which gives the highest epithermal neutron current to flux ratio of about 1.0, has an epithermal flux of $2.8 \times 10^7 \text{ n cm}^{-2} \text{ s}^{-1}$ and has a convergent type of collimator. However, in this case, the obtained epithermal flux is impractical for the BNCT.

It can be concluded that the candidate patterns must be among the patterns which would make sure the required beam aperture ($>$ a ratio of 0.75) with an epithermal flux of $> 5.0 \times 10^8 \text{ n cm}^{-2} \text{ s}^{-1}$. The available patterns are pointed out on Fig. 6.12 (d) and tabulated in Table 6.6. It is understood from the results that a well-collimated beam typically has an outlet radius (or in terms of beam aperture area) higher than 0.5 cm but not greater than 0.7 cm, an inlet radius wider than 5 cm and a length longer than 20 cm. By far the best materials for the collimator are the PE and Cerrobend. On the other hand, Al_2O_3 seems a promising material among the collimator materials used in the GA. Other materials are, apparently, not proper although they are widely used in the experiments as collimator.

It is important to note that the beam aperture (outer) diameter can be adjusted according to the size of the tumor.

Table 6.6 Available sub-patterns for the collimator sub-pattern design

$J_{\text{epith}}/\Phi_{\text{epith}}$	Φ_{epith} $10^8 \text{ n cm}^{-2} \text{ s}^{-1}$	Material	L (cm)	r_i (cm)	r_o (cm)
0.877	7.069	PE	23.70	7.39	0.63
0.877	6.614	PE	28.38	6.28	0.69
0.911	6.603	Al ₂ O ₃	23.01	7.42	0.58
0.891	6.579	PE	27.06	6.29	0.68
0.886	6.551	PE	33.77	7.34	0.70
0.765	6.546	Cerro	24.44	7.71	0.52
0.775	6.486	PE	14.99	7.17	0.53
0.905	6.423	Cerro	23.01	7.42	0.58
0.815	6.369	PE	27.73	9.51	0.45
0.937	6.336	Al ₂ O ₃	21.00	7.42	0.58
0.852	6.295	PE	14.75	5.09	0.43
0.931	6.274	PE	25.47	6.44	0.60
0.925	6.226	PE	26.02	5.57	0.61
0.939	5.779	Cerro	25.47	6.44	0.60
0.922	5.640	Al ₂ O ₃	24.39	4.35	0.61
0.923	5.403	Cerro	33.08	7.37	0.65
0.978	5.319	PE	29.10	4.03	0.60
0.966	5.087	PE	26.91	4.20	0.58
0.977	4.849	Cerro	25.59	2.83	0.62
0.939	4.847	PE	27.73	3.70	0.45
0.957	4.729	Cerro	29.93	4.63	0.66
0.989	4.714	PE	27.39	2.49	0.64
0.958	4.692	Cerro	28.72	4.48	0.66
0.967	4.569	PE	27.06	2.79	0.68
0.934	4.504	Cerro	32.56	6.41	0.69
0.955	4.414	Cerro	33.77	6.20	0.70
0.980	4.410	Cerro	28.72	2.00	0.66
0.956	4.369	Cerro	31.31	7.19	0.69
0.973	4.357	Cerro	32.69	2.67	0.70
0.992	4.291	PE	30.25	2.35	0.66
0.967	4.222	Cerro	33.77	6.56	0.70
0.972	4.113	Cerro	33.77	5.19	0.70
0.994	4.065	PE	32.44	2.17	0.68

A selected suitable collimator for the BNCT is depicted in Fig. 6.13. The collimator has a length of 23.7 cm, an inlet diameter of 14.78 cm and an outlet diameter of 1.26 cm. The collimator material is PE and collimator type is convergent with a conical shape. Such design yields a current to flux ratio of 0.877. Effect of this collimator design on the neutron fluxes is shown in Table 6.7. Incoming particle fluxes are calculated at the entry surface of the collimator enclosed with the inlet radius while outgoing particle fluxes are calculated at the exit surface of the collimator enclosed with the outlet radius. The fluxes reported are the values averaged over the considered surfaces.

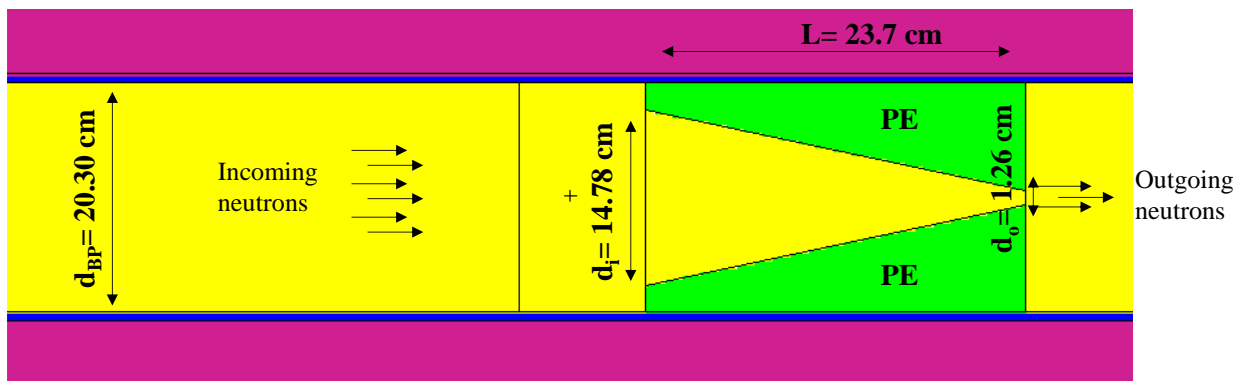


Fig. 6.13 A selected pattern for collimator

Table 6.7 Particle fluxes with and without the sub-pattern

	Incoming Particle Flux	Outgoing Particle Flux	
		Bare	Sub-pattern
Φ_{th} (n/cm ² .s)	$1.044 \pm 0.0060 \times 10^9$	$5.876 \pm 0.0077 \times 10^8$	$9.287 \pm 0.108 \times 10^8$
Φ_{epi} (n/cm ² .s)	$4.140 \pm 0.0116 \times 10^8$	$2.702 \pm 0.0144 \times 10^8$	$7.069 \pm 0.132 \times 10^8$
Φ_{fast} (n/cm ² .s)	$8.264 \pm 0.0090 \times 10^8$	$5.751 \pm 0.0108 \times 10^8$	$9.724 \pm 0.124 \times 10^8$
J_{epi}/Φ_{epi}	-	0.891 ± 0.013	0.877 ± 0.026
I_γ (γ/cm ² .s)	$2.715 \pm 0.0079 \times 10^9$	$1.873 \pm 0.0096 \times 10^9$	-

6.3.5 Final Pattern: Uniting the Sub-patterns

A final pattern, as shown in Fig. 6.14, is formed by joining the created sub-patterns, spectrum shifter, filtering and collimator. A comparison between the bare port and the designed port is given in Table 6.8.

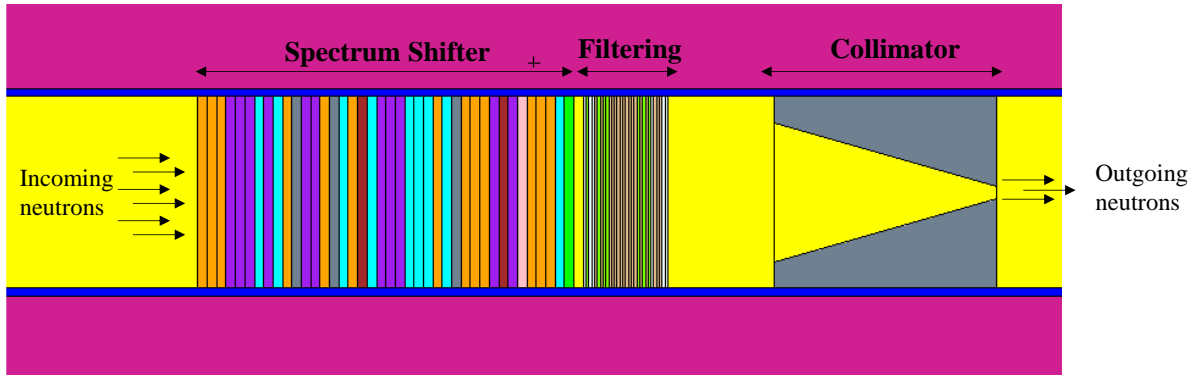


Fig. 6.14 View of the final pattern

Table 6.8 Particle fluxes with and without the final pattern

	Incoming Particle Flux	Outgoing Particle Flux	
		Bare	Pattern
Φ_{th} (n/cm ² .s)	$2.034 \pm 0.0041 \times 10^9$	$5.876 \pm 0.0077 \times 10^8$	$0.325 \pm 0.021 \times 10^8$
Φ_{epi} (n/cm ² .s)	$7.232 \pm 0.0087 \times 10^8$	$2.702 \pm 0.0144 \times 10^8$	$4.167 \pm 0.135 \times 10^8$
Φ_{fast} (n/cm ² .s)	$1.376 \pm 0.0069 \times 10^9$	$5.751 \pm 0.0108 \times 10^8$	$1.967 \pm 0.107 \times 10^8$
J_{epi}/Φ_{epi}	-	0.891 ± 0.013	0.877 ± 0.026
I_{γ} (γ/cm ² .s)	$4.622 \pm 0.0059 \times 10^9$	$1.873 \pm 0.0096 \times 10^9$	$9.394 \pm 0.112 \times 10^6$

As seen in table, when all the sub-patterns are joined to obtain the final pattern, at the end of BP, thermal, epithermal and fast fluxes are calculated to be about 0.33 , 4.2 and 2.0×10^8 n cm⁻² s⁻¹, respectively. A collimation ratio of 0.877 is achieved. Compared with the bare value, a higher epithermal flux and, lower thermal and fast fluxes are obtained.

Effect of use of sub-patterns in the BP on the neutron fluxes is clearly shown in Fig. 6.15. Thermal flux drastically decreases as the neutrons pass through the filtering. Fast flux decreases continuously inside the spectrum shifter but not inside the filtering. Intensity of the fluxes increases to some extent due to collimation process.

Furthermore, effect of beam shaping process on the neutron spectrum is demonstrated in Fig. 6.16 at the port exit. As seen in the figure, the neutrons with low energy ($< 10^8$) are completely removed from the spectrum. The figure also points out that the fast neutrons, by slowing down, make significant contribution to the epithermal flux in the energy range of 10^{-6} and 10^{-4} eV.

In the final step, photon fluence is reduced to an acceptable level as described in Section 4.2. Last row of Table 6.8 exhibits the photon fluence for the bare BP and the modified BP. Photon

fluence decreases from 1.873×10^9 to about 0.01×10^9 $\text{n cm}^{-2} \text{s}^{-1}$. As seen in the table, it is evident that the photon fluence at the port exit is quite low. Therefore, there is no need to shield the photons further. Yet, a sufficient thickness of Pb shielding block is calculated using the information given in Section 4.4.4 and the material is placed right at the exit of the collimator. The required Pb thickness is found to be about 5 cm (tenth-layer value -TLV) to reduce the photon fluence by 10 times.

As a result, it is possible to obtain a desired epithermal neutron beam if a proper pattern is used inside the BP.

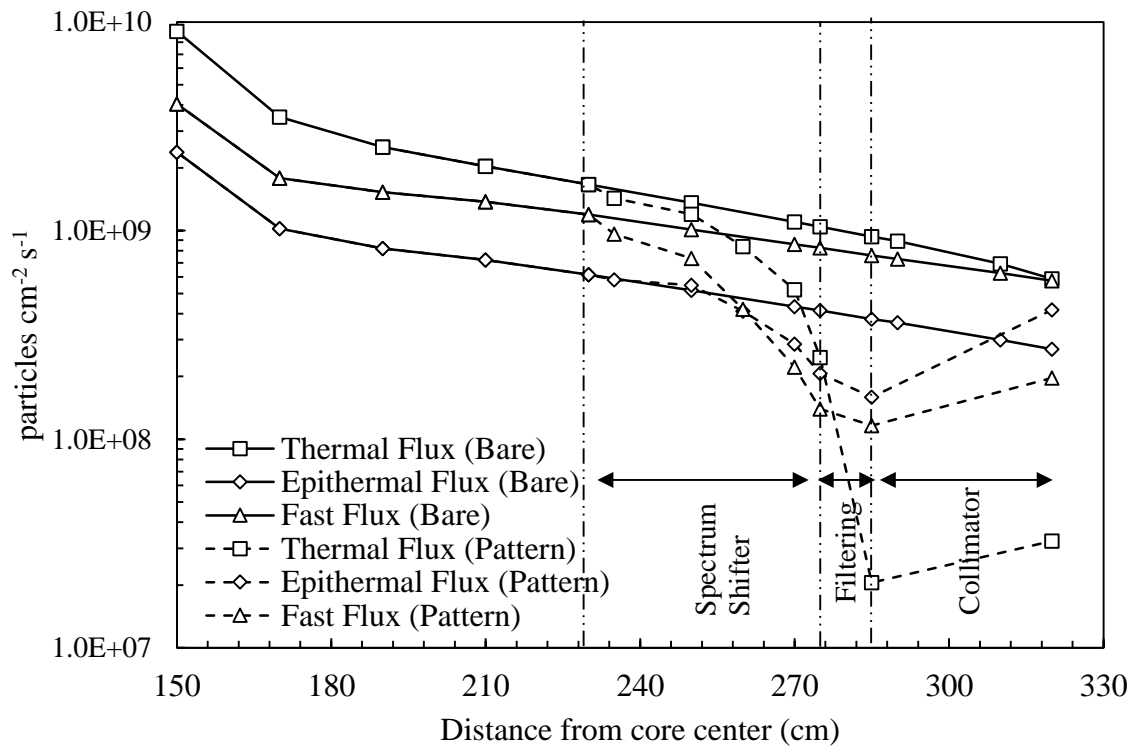


Fig. 6.15 Change of particle flux along with distance from the core center with and without the final pattern

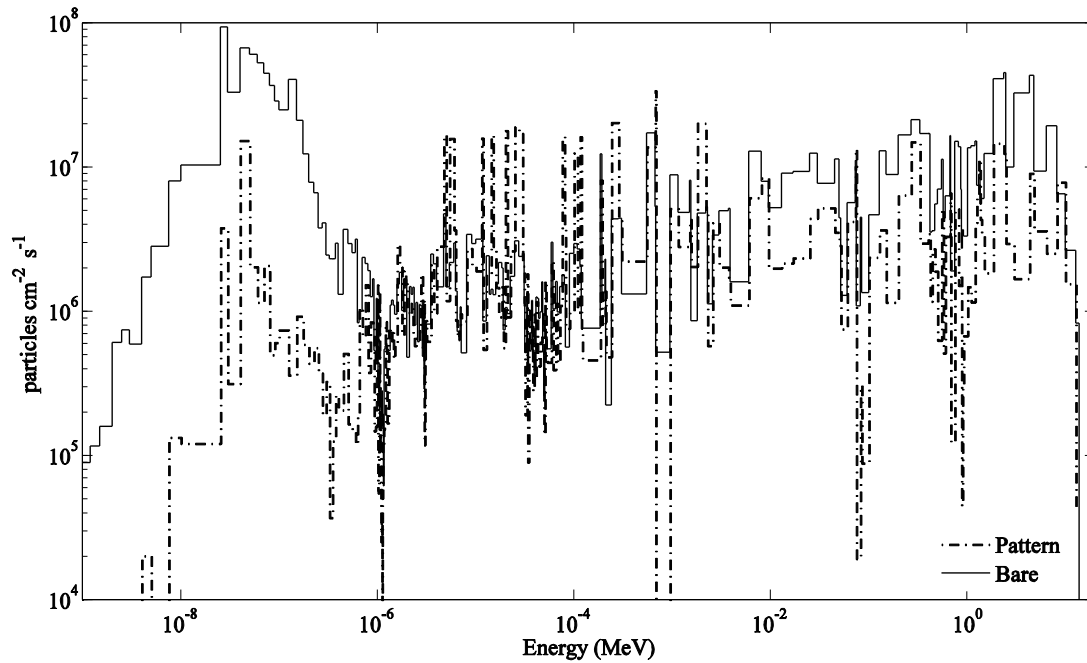


Fig. 6.16 Neutron spectrum at the port exit with and without the final pattern

6.4 Concluding Remarks

On the Reactor Modeling

- ✓ For ITU-TRR, a detailed modelling with MC method is carried out in a manner consistent with its design parameters determined by General Atomic. As well as inclusion of the in-core components, for the future studies, the model incorporates out-core components such as neutron beam tubes, thermal column, concrete biological shield and neutron radiography room.
- ✓ Outcomes of the MCNP model are in good agreement with the SAR (and experimental) data. It appears from the results that there is not much to be gained by modelling the reactor with further details. That is, the current model reported in this study is capable of producing acceptable results in computing.

On the Burnup Analysis

- ✓ From the results, it is understood that spectrum of the incoming particles to the PBP, specifically epithermal neutrons, is clearly affected from the burnup level of the reactor. At some energy levels, thermal flux changes up to $\pm 1\%$ and fast flux increases by 3% . Epithermal neutron flux fluctuates up to $\pm 10\%$. Thus, a burnup-corrected neutron spectrum should be used in the future BNCT studies.

On the Optimization Calculations

- ✓ The prepared GA code coupled with MCNP is capable of finding the proper patterns for the desired nuclear application. Depending on the application type, it would be sufficient to modify the code (only the cost function module).
- ✓ The most important issue in an optimization study is the time required to compute the cost value. Although the MC based-codes yield more reliable results (by simulating each particle) than the deterministic codes, these codes require naturally more time to get a cost value. In this study, one cost calculation takes more or less 3 minutes to get a standard deviation of 0.07 % when Intel Xenon E5 Processors (12x4) with a core frequency of 3.10 GHz are used. For over 7000 iterations, the necessary time for the full computation would be at least two weeks.
- ✓ It is understood from the results that discretization (use of constant material thickness) of the continuous optimization problem is a good way to speed up the calculations. An alternative way is to use a deterministic reactor physics code.
- ✓ Although the solutions provided in this study are indicated as the best solutions, it should be noted that those, in fact, may not be the best. The reason is that the stopping criteria are defined by a number of external parameters. When one of the specified criteria is met, the algorithm stops searching. Therefore, it is possible to find a better pattern should the algorithm keep searching. In this study, all of the best patterns are obtained while all of the elite solutions are in the first front.
- ✓ The parameters used in the GA are the population size, crossover/mutation fractions, and mutation rate and convergence criteria. Those parameters affect the convergence speed of the optimization. Therefore, the users must be aware of which values of parameters are better for their problems.
- ✓ The reason for the long MC calculations is that the deep penetration problems require excessive neutron history combined with different variance reduction techniques. The computational time has a complex relationship (inverse proportion) with standard deviation. As the deviation decreases, the required time increases.
- ✓ In a classic search, there is about 9×10^{10} (a combination of 40 mesh points using 17 different materials) possible patterns to be searched for the spectrum shifter materials. It becomes 3×10^7 (a combination of 30 mesh point using 10 different materials) for the filtering materials. In this study, the pareto-optimal solutions are obtained at the maximum iteration number of 9800 in the optimization of spectrum shifter materials.

On the GA Results

- ✓ Selection criterion for the material thickness is based on the mean free path values of the selected materials. Yet, the total thickness of a material inside the optimized pattern is open to change when the thickness is changed.
- ✓ The order of the materials in a sub-pattern does not have a significant impact on the flux values at the pattern exit; however, the order of sub-patterns inside the BP seriously affects the flux values at the port exit.

On the Capability of PBP for the BNCT

- ✓ In the bare port, the magnitude of the incident beam reduces from 10^{12} particle $\text{cm}^{-2} \text{s}^{-1}$ to 10^9 particle $\text{cm}^{-2} \text{s}^{-1}$ as the distance from the port inlet increases.
- ✓ The bare PBP has a thermal neutron flux of $5.88 \pm 0.01 \times 10^8$ n $\text{cm}^{-2} \text{s}^{-1}$, an epithermal neutron flux of $2.70 \pm 0.01 \times 10^8$ n $\text{cm}^{-2} \text{s}^{-1}$, a fast neutron flux of $5.75 \pm 0.01 \times 10^8$ n $\text{cm}^{-2} \text{s}^{-1}$, a photon fluence of $1.87 \pm 0.01 \times 10^9$ γ $\text{cm}^{-2} \text{s}^{-1}$ and a current-to-flux ratio of 0.89 at the port exit. This implies that theoretically, an epithermal neutron flux of 8.45 (fast plus epithermal) $\times 10^8$ n $\text{cm}^{-2} \text{s}^{-1}$ is possible if all the fast neutrons, without any losses, slow down to the epithermal.
- ✓ Using the spectrum shifter method, it is possible to reduce the fast neutron flux of the incident beam by 9 times with almost 3 times reduction in the epithermal flux. The main materials among the suggested materials to obtain a good pattern are Al (with compound forms), S, Kr and Ar. Si and K addition in small amounts seem suitable.
- ✓ Using the filtering method, it is possible to reduce the thermal neutron flux of the incident beam by 12 times with almost no cost in the epithermal flux. A good filtering pattern can be formed with a combination of Cd and Ti. The beam may be tuned by adding Gd, Ag, In and Th elements in small amounts.
- ✓ Using the collimation method, it is possible to increase intensity of the epithermal neutron flux of the incident beam by about 3 times and to obtain a highly collimated beam (<0.75). The qualified materials for the collimator are PE and Cerrobend. In addition to these, Al_2O_3 seems a promising material. The best collimator type is the convergent type with a conical shape.
- ✓ When the optimized pattern is used inside the port, epithermal neutron flux at the port exit is calculated to be $4.17 \times 10^8 \pm 0.14$ n $\text{cm}^{-2} \text{s}^{-1}$ with a current-to-flux ratio of 0.88 ± 0.03 . Furthermore, the thermal and fast neutron fluxes, and photon fluence are reduced by about 20, 3 and 200 times, respectively.

- ✓ Using the final pattern, patient irradiation period for receiving the sufficient neutron dose is calculated to be about 25 min. It is likely to extend the period a little bit. In this manner, the sub-patterns that have an epithermal flux lower than $1.0 \times 10^8 \text{ n cm}^{-2} \text{ s}^{-1}$ can be utilized for the BNCT. In this case, biological half-life of the boron concentration in the tumor cells limits the period.
- ✓ In this study, epithermal energy range is assumed to be higher than 0.625 eV (instead of 0.4 eV) lower than 10 keV, due to need of conservative calculations. If the contributions of 0.4-0.625 eV and 10-20 keV neutrons are taken into account, it is evident that epithermal flux would increase some more. Furthermore, somewhat contribution to the dose due to epithermal neutrons is expected from the fast neutrons as some of the fast neutrons will be epithermal inside the tumor.
- ✓ The results show that although there is no way to reach the desired epithermal neutron flux ($> 10^9 \text{ n cm}^{-2} \text{ s}^{-1}$) in the PBP, BNCT is applicable in the port, by supplying a minimum desired epithermal neutron flux at the port exit. Therefore, the method suggested in this study provides promising results.
- ✓ To sum up, the beam shaping method suggested in this study is independent from user experiences and can readily be implemented into any incident beam of a considered research reactor (even for other neutron sources) for a desired medical/industrial application.

On the Future Work

- ✓ Using the method proposed in this study, applicability of the BNCT in the tangential BP is to be investigated. Furthermore, the bare port results point out that the PBP may support a wide range of nuclear applications. As a future work, availability of neutron radiography (imaging) application in the PBP (later in other BPs) can be studied.
- ✓ To reduce the irradiation period of the patient, the reactor may be uprated to a higher power level.
- ✓ By and large, in this study, natural form of the materials is used due to fabrication considerations. However, as can be seen from the neutronic properties of the examined isotopes, use of the pure (in the form of single isotope) or enriched form of the selected materials in the patterns would yield a well-shaped beam. For this purpose, scope of this study is going to be broadened through the use of pure/enriched materials.
- ✓ The results calculated in this study are the theoretical values; thus, they need to be supported by the experimental measurements.

REFERENCES

- [1] Akan, Z., Türkmen, M., Çakır, T., Reyhancan, İ. A., Çolak, Ü., Okka, M., Kızıldaş, S., Modification of the radial beam port of ITU TRIGA Mark II research reactor for BNCT applications, *Applied Radiation and Isotopes*, 99, 110-116, **2015**.
- [2] Locher, G. L., Biological effects and therapeutic possibilities of neutrons, *American Journal Roentgenological and Radium Therapy*, 36(1), **1936**.
- [3] Kruger P.G., Some biological effects of nuclear disintegration products on neoplastic tissue, *Proceedings of the National Academy of Sciences of the United States of America*, 26(3), 181–192, **1940**.
- [4] Harling, O.K., Boron neutron capture therapy research at the MIT Research Reactor, *Neutron News*, 5 (4), 23–28, **1994**.
- [5] Harling, O.K., et al., The fission converter based epithermal neutron irradiation facility at the MIT Reactor, *Nuclear Science and Engineering*, 140, 223-240, **2002**.
- [6] Matsumoto, T., Liu, H., B., Brugger, R.M., Design Studies of an Epithermal Neutron Beam for Neutron Capture Therapy at the Musashi Reactor, *Journal of Nuclear Science and Technology*, 32(2), 87-94, **1995**.
- [7] Matsumoto, T., Design of Neutron Beams for Boron Neutron Capture Therapy for TRIGA Reactor, *Journal of Nuclear Science and Technology*, 33(2), 171-178, **1996**.
- [8] Gabel, D., Sauerwein W., *Clinical implementation of boron neutron capture therapy in Europe*. In: Amaldi U, Larsson B (eds) *Hadrontherapy in oncology*, Elsevier Science, Amsterdam, pp 509–517, **1994**.
- [9] Sauerwein, W., Hideghéty, K., Gabel, D., Moss, R.L., European clinical trials of boron neutron capture therapy for glioblastoma, *Nuclear News*, 41(2), 54–56, **1998**.
- [10] Oka, Y., et al., Study of epithermal neutron columns for boron neutron capture therapy, *Progress in Nuclear Energy*, 32 (1–2), 61–70, **1998**.
- [11] Kageji, T., et al., Radiation injury of boron neutron capture therapy using mixed epithermal- and thermal neutron beams in patients with malignant glioma, *Applied Radiation and Isotopes*, 61 (5), 1063–1067, **2004**.
- [12] Auterinen, I., et al., *Metamorphosis of a 35 year-old TRIGA reactor into a modern BNCT facility*. In: Hawthorne, M.F., Shelly, K., Wiersema, R.J., *Frontiers in Neutron Capture Therapy*. Vol. I, Kluwer Academic/Plenum Publishers, New York, 267–275, **2001**.

- [13] Schmitz, T., et al., Dose calculation in biological samples in a mixed neutron-gamma field at the TRIGA reactor of the University of Mainz, *Acta Oncologica*, 49 (7), 1165-1169, **2010**.
- [14] Auterinen, I., et al., A toolkit for epithermal neutron beam characterization in BNCT. *Radiation Protection Dosimetry*, 110 (1-4), 587-93, **2004**.
- [15] Hsu, F.Y., et al., Microdosimetry study of THOR BNCT beam using tissue equivalent proportional counter, *Applied Radiation Isotopes*, 67 (7-8), 175-178, **2009**.
- [16] Harker, Y.D., et al., Neutron sources for BNCT using low-power research reactors or compact charged particle accelerators, *International Conference Neutrons in Research and Industry*, Crete, Greece, 48, **1997**.
- [17] Gritzay, O.O., et al., Monte-Carlo calculations for the development of a BNCT neutron source at the Kyiv Research Reactor, *Applied Radiation and Isotopes*, 61, 869–873 **2004**.
- [18] Protti, N., et al., Calculations of dose distributions in the lungs of a rat model irradiated in the thermal column of the TRIGA reactor in Pavia, *Applied Radiation and Isotopes*, 67, 210–213, **2009**.
- [19] Ballarini, F., et al., Cell death following BNCT: A theoretical approach based on Monte Carlo simulations, *Applied Radiation and Isotopes*, 69, 1745–1747, **2011**.
- [20] Wortmann, B., Knorr, J., Basic requirements and parameter optimization for boron neutron capture therapy of extracorporeal irradiated and auto-transplanted organs, *Applied Radiation and Isotopes*, 70, 1709–1717, **2012**.
- [21] Liu, H.M., et al., Increase of the beam intensity for BNCT by changing the core configuration at THOR, *Applied Radiation and Isotopes*, 67, 247–250, **2009**.
- [22] Liu, Y.H. et al., Neutron spectra measurement and comparison of the HFR and THOR BNCT beams, *Applied Radiation and Isotopes*, 67, 137–140, **2009**.
- [23] Liu, Y.H., et al., The angular and spatial distributions of the thermal neutron source description of the THOR BNCT beam, *Radiation Measurements*, 45, 1432 -1435, **2010**.
- [24] Liu, Y.H., et al., Performance evaluation of the source description of the THOR BNCT epithermal neutron beam, *Applied Radiation and Isotopes*, 69, 1892–1896, **2011**.
- [25] Colautti, P., et al., Microdosimetric measurements in the thermal neutron irradiation facility of LENA reactor, *Applied Radiation and Isotopes*, 88, 147-152, **2014**.

- [26] Koivunoro, H., et al., The FiR 1 photon beam model adjustment according to in-air spectrum measurements with the Mg (Ar) ionization chamber, *Applied Radiation and Isotopes*, 88, 134–138, **2014**.
- [27] Nagels, S., et al., Determination of the irradiation field at the research reactor TRIGA Mainz for BNCT, *Applied Radiation and Isotopes*, 67, 242–246, **2009**.
- [28] Hampel, G., et al., Irradiation facility at the TRIGA Mainz for treatment of liver metastases, *Applied Radiation and Isotopes*, 67, 238–241, **2009**.
- [29] Blaickner, M., et al., Dosimetric feasibility study for an extracorporeal BNCT application on liver metastases at the TRIGA Mainz, *Applied Radiation and Isotopes*, 70, 139–143, **2012**.
- [30] Vega-Carrillo, H.R., et al., Neutron spectra at two beam ports of a TRIGA Mark III reactor loaded with HEU fuel, *Applied Radiation and Isotopes*, 83, 252–255, **2014**.
- [31] Belousov, S., Ilieva, K., Preliminary modeling of BNCT beam tube on IRT in Sofia. *Applied Radiation and Isotopes*, 67, 230–233, **2009**.
- [32] Schickler, R.A., et al., Comparison of HEU and LEU neutron spectra in irradiation facilities at the Oregon State TRIGA Reactor, *Nuclear Engineering and Design*, 262, 340– 349, **2013**.
- [33] Tiyapun K., *Epithermal Neutron Beam Design at the Oregon State University TRIGA Mark II Reactor (OSTR) Based on Monte Carlo Methods*, Master of Science, Oregon State University, Oregon, **1997**.
- [34] Sweezy E. J., *Development of a Boron Neutron Capture Enhanced Fast Neutron Therapy Beam*, Doctor of Philosophy, Georgia Institute of Technology, **2002**.
- [35] Bleuel, L. D., *Determination and Production of an Optimal Neutron Energy Spectrum for Boron Neutron Capture Therapy*, Doctor of Philosophy, University of California, **2003**.
- [36] Özçelik Ş., Gül, A., Boron-containing tetrapyrroles, *Turkish Journal of Chemistry*, 38, 950-979, **2014**.
- [37] General Atomics, *Safety Analysis Report for the TRIGA Mark II Reactor*, Institute for Nuclear Energy, Istanbul Technical University, **1978**.
- [38] Olander, D., Greenspan, E., Garkisch, H.D., Petrovic, B., Uranium-zirconium hydride fuel properties, *Nuclear Engineering and Design*, 239, 1406-1424, **2009**.
- [39] Simnad, M.T., The U-ZrHx alloy: its properties and use in TRIGA fuel, *Nuclear Engineering and Design*, 64, 403, **1981**.

- [40] GA Technologies, Inc., by Tomsio, N., *Characterization of TRIGA Fuel*, ORNL/Sub/86-22047/3, GA-C18542, **1986**.
- [41] GA Technologies, Inc., *Uranium-zirconium hydride TRIGA LEU fuel*. In: Research Reactor Core Conversion Guidebook, Vol. 4, Fuels. IAEA-TECDOC-643, Appendix I-7 (19), **1992**.
- [42] U.S. Department of Energy, *Office of Civilian Radiactive Waste Management, Characteristics of Potential Repository Wastes*, DOE/RW-0184-R1-Vol.2, TI92 019056, **1992**.
- [43] El Bakkari, B., El Bardouni, T., Nacir, B., El Younoussi, C., Boulaich, Y., Boukhal, H., Zoubair, M., Fuel burnup analysis for the Moroccan TRIGA research reactor, *Annals of Nuclear Energy*, 51, 112-119, **2013**.
- [44] Böck, H., Villa, M., Periodic fuel element inspections at the TRIGA Mark II Reactor Vienna, *International Conference: Nuclear Energy in Central Europe 2001*, Portoroz, Slovenia, September 10-13, Paper no: 514, **2001**.
- [45] Persic, A., Ravnik, M., Slavic, S., Zagar, T., *TRIGLAV: A program package for research reactor calculations*, Reactor Physics Division, Josef Stefan Institute, Slovenia, IJS-DP-7862, **1998**.
- [46] X-5 Monte Carlo Team, *MCNP – A General Monte Carlo N-Particle Transport Code*, Version 5, LA-UR-03-1987, April 24, **2003** (revised October 3rd, 2005).
- [47] Chadwick, M.B. et al., ENDF/B-VII.0: Next Generation Evaluated Nuclear Data Library for Nuclear Science and Technology, *Nuclear Data Sheets, Special Issue on Evaluated Nuclear Data File*, **2006**.
- [48] Rose, F.P., *ENDF-201, ENDF/B-VI Summary Documentation*, BNL-NCS-17541, 4th ed., 1991.
- [49] Koning, A., Forrest, R., Kellett, M., Mills, R., Henriksson, H., Rugama, T., *The JEFF-3.1 Nuclear Data Library*, JEFF Report 21, **2006**.
- [50] Santamarina, A. et al., *The JEFF-3.1.1 Nuclear Data Library*, ISBN 978-92-64-99074-6 (Data Bank), NEA No. 6807, **2009**.
- [51] MacFarlane, R. E., Kahler, A. C., Methods for Processing ENDF/B-VII with NJOY, *Nuclear Data Sheets*, 111, 2739-2890, **2010**.
- [52] MacFarlane, R. E., Muir, D. W., *The NJOY Nuclear Data Processing System*, Version 91, Los Alamos National Laboratory report, LA-12740-M, **1994**.

- [53] Chadwick, M.B., et al., ENDF/B-VII.1: Nuclear Data for Science and Technology: Cross Sections, Covariances, Fission Product Yields and Decay Data, *Nuclear Data Sheets*, 112(12), 2887-2996, **2011**.
- [54] JEFF team, *JEFF-3.2: Evaluated nuclear data library*, **2014**.
https://www.oecd-nea.org/dbforms/data/eva/evatapes/jeff_32.
- [55] Ge, Z. G., et al., The Updated Version of Chinese Evaluated Nuclear Data Library (CENDL-3.1). In: *Proc. International Conference on Nuclear Data for Science and Technology*, Jeju Island, Korea, April 26-30, **2010**.
- [56] Shibata, K., et al., JENDL-4.0: A new library for nuclear science and engineering. *Journal of Nuclear Science and Technology*, 48(1), 1-30, **2011**.
- [57] Koning, A.J., et al., *TENDL-2013: TALYS-based evaluated nuclear data library*. www.talys.eu/tendl-2013.html, **2013**.
- [58] Poston, D.L., Trellue, H.R., *User's Manual, Version 2.0 for MONTEBURNS*, LA-UR-99-4999, **1999**.
- [59] Driscoll, M. J., Downar, T. J., Pilat, E. E., *The Linear Reactivity Model for Nuclear Fuel Management*, American Nuclear Society, La Grange Park, Illinois, **1990**.
- [60] Pelowitz, D. B., Fallgren, A. J., McMath, G. E., *MCNP6 User's Manual*, Code Version 6.1.1beta, Manual Rev. 0, LA-CP-14-00745, Rev. 0, **2014**.
- [61] IAEA, *Current status of neutron capture therapy*, Technical Reports Series, No. 1223, Vienna, ISSN 1011-4289, **2001**.
- [62] Harling O. K., Riley, K. J., *Fission Reactor-Based Irradiation Facilities for Neutron Capture Therapy*, In: Sauerwein, W. A. G., et al., *Neutron Capture Therapy: Principles and Applications*, Springer, Heidelberg, **2012**.
- [63] Korea Atomic Energy Research Institute, Nuclear Data Center, <http://atom.kaeri.re.kr> (July, **2015**).
- [64] Domanus, J. C., *Practical Neutron Radiography*, Commission of the European Communities Neutron Radiography Working Group, Kluwer Academic Publishers, Dordrecht, Netherlands, **1992**.
- [65] Hubbel, J. H., Seltzer, S. M., Tables of X-Ray Mass Attenuation Coefficients and Mass Energy-Absorption Coefficients from 1 keV to 20 MeV for Elements Z = 1 to 92 and 48 Additional Substances of Dosimetric Interest, *NIST*, Standard Reference Database 126, NISTIR 5632, <http://www.nist.gov/pml/data/xraycoef/index.cfm> (July, **2015**).

- [66] Deb, K., et al., A Fast and Elitist Multiobjective Genetic Algorithm: NSGA-II, *IEEE Transactions on Evolutionary Computation*, 6 (2), 182-197, **2002**.
- [67] Schaffer, J. D., Multiple objective optimization with vector evaluated genetic algorithms, in *Proceedings of the First International Conference on Genetic Algorithms*, Grefenstette, J. J., Ed. Hillsdale, NJ: Lawrence Erlbaum, pp. 93–100, **1987**.
- [68] Fonseca, C. M., Fleming, P. J., Multiobjective optimization and multiple constraint handling with evolutionary algorithms II: Application example, *IEEE Transactions on Systems, Man and Cybernetics*, 28, 38–47, **1998**.
- [69] Kursawe, F., A variant of evolution strategies for vector optimization, In: *Parallel Problem Solving from Nature*, Schwefel, H.-P., Männer, R., Eds. Berlin, Germany: Springer-Verlag, pp. 193–197, **1990**.
- [70] Zitzler, E., Deb, K., Thiele, L., Comparison of multiobjective evolutionary algorithms: Empirical results, *Evolutionary Computation*, 8(2), pp. 173–195, **2000**.
- [71] Haupt, R.L., Haupt, S.E, *Practical Genetic Algorithms*, John Wiley & Sons, Inc., Hoboken, New Jersey, **2004**.
- [72] Mele, I., Ravnik, M., Trkov, A., TRIGA Mark II Benchmark Experiment, Part I: Steady-State Operation, *Nuclear Technology*, 105, 37-51, **1994**.
- [73] Mele, I., Ravnik, M., Trkov, A., TRIGA Mark II Benchmark Experiment, Part II: Pulse Operation, *Nuclear Technology*, 105, 52-58, **1994**.

CIRRICULUM VITAE

Credentials

Name, Surname : Mehmet TÜRKMEN
Place of Birth : Çorum
Marital Status : Single
E-mail : tm@hacettepe.edu.tr; mehmeturkmen@gmail.com
Address : Altay Mah. 33 Sok. Yalım Apt. No:14/9
Eryaman, Etimesgut, Ankara, Turkey

Education

High School : Fatsa High School
BSc. : Nuclear Engineering, Faculty of Eng., Hacettepe Uni.,
MSc. : Nuclear Engineering, Faculty of Eng., Hacettepe Uni.
PhD. : Nuclear Engineering, Faculty of Eng., Hacettepe Uni.

Foreign Languages: English (Advance)

Work Experiences: Research Assistant in Dept. of Nuclear Engineering (2007-2015)

Areas of Experiences: Monte Carlo Method, In-Core Fuel Management, Reactor Design Development, Radiation Physics, Genetic Algorithm

Projects and Budgets:

1. Sökmen, C.N., Turkmen, M., 2015. Effect of Thermal-Neutronic Coupling on the Cross-Sections of Nuclear Fuel. 1001-Project of the Scientific and Technological Research Council of Turkey (TUBITAK) (Project No: 114F375).
2. UAM Expert Group: K. Ivanov, M. Avramova, S. Kamerow, I. Kodeli, E. Sartori, E. Ivanov, O. Cabellos, Turkey Contributors of Benchmark Group: Sökmen, C. Niyazi, Türkmen, M., 2013. Benchmark for Uncertainty Analysis in Modeling (UAM) for Design, Operation And Safety Analysis of LWRs, Volume I: Specification and Support Data for the Neutronics Cases (Phase I), NEA/NSC/DOC(2012).
3. Zabunoğlu, H.O., Türkmen, M., 2013. Cost Analysis for Once-Through Uranium and Uranium-Thorium Fuel Cycle of ACR-700 and CANDU-6 Reactors. Comprehensive

Research Project Supported by Scientific Research and Development Office (Project No: 01001602003), Hacettepe Uni., Ankara, Turkey.

4. National Scholarship Award for Ph.D. Students from the Scientific and Technological Research Council of Turkey, 2013-to-Present, TUBITAK-BIDEB 2211-C.

Publications:

1. Türkmen, M., Çelikten, O. Ş., Sökmen, C. N., 2015. Uncertainty in modeling due to use of isothermal temperature inside the fuel. Nuclear Engineering and Technology, Submitted article. In review process.
2. Türkmen, M., Çolak, Ü., Ergün, Ş., 2015. Core map generation for the ITU TRIGA Mark II research reactor using Genetic Algorithm coupled with Monte Carlo method. Nuclear Engineering and Design, Accepted article.
3. Türkmen, M., Çolak, Ü., Ergün, Ş., 2015. Effect of burnup on the neutronic parameters of ITU TRIGA Mark II Research Reactor, Progress in Nuclear Energy, 83, 26-34.
4. Akan, Z., Türkmen, M., Çakır, T., Reyhancan, İ. A., Çolak, Ü., Okka, M., Kızıldaş, S., 2015. Modification of the radial beam port of ITU TRIGA Mark II research reactor for BNCT applications, Applied Radiation and Isotopes, 99, 110-116.
5. Türkmen, M., Çolak, Ü., 2014. Analysis of ITU TRIGA Mark II Research Reactor Using Monte Carlo Method. Prog. Nucl. Energy 77, 152-159
6. Türkmen, M., Zabunoğlu H. O., 2012. Use of Th and U in CANDU-6 and ACR-700 on the once-through cycle: Burnup analyses, natural U requirement/saving and nuclear resource utilization. Journal of Nuclear Materials 429, 263–269.
7. Türkmen, M., Çolak Ü., 2012. Effect of Packing on Neutron Spectrum and the Isotopic Composition of HTGR fuel. Annals of Nuclear Energy 46, 29–36.

Oral and Poster Presentations:

1. Türkmen, M., Çolak, Ü., 2014. Fuel Burnup Calculation in ITU TRIGA Mark II Research Reactor by Using Monte Carlo Method. In: NENE2014: 23rd International Conference Nuclear Energy for New Europe, Portorož, Slovenia, September 8-11.
2. Türkmen, M., Çolak, Ü., 2013. ITU TRIGA Mark II Research Reactor: A Benchmark Analysis with Various Codes. In: The European Research Reactor Conference: RRFM2013, Saint Petersburg, Russia, April 21 – 25, RRFM2013 Transaction, pp. 395-400.

3. Çolak, Ü., Türkmen M., 2011. The Effect of Neutron Energy Spectrum on Actinide Management in High Temperature Reactors. In: 20th International Conference Nuclear Energy for New Europe 2011 (NENE2011), Bovec, Slovenia.
4. Türkmen, M., Çolak, Ü., 2010. Neutron Energy Spectrum Shift and Its Effect on Fission Product Inventory in Spherical HTGR Fuel. In: IAEA Technical Meeting on High Temperature Gas Cooled Reactor Fuel & Fuel Cycle, Vienna, Austria.
5. Türkmen, M., Zabunoğlu, H. O., 2009. Thorium Utilization in CANDU-6 and ACR (Advanced CANDU). In: X. National Nuclear Science and Technology Congress, September 9-11, Muğla, Turkey.